InSb Semiconductors and (In,Mn)Sb Diluted Magnetic Semiconductors: Growth and Properties

D I S S E R T A T I O N

zur Erlangung des akademischen Grades

doctor rerum naturalium
im Fach Physik

eingereicht an der
Mathematisch-Naturwissenschaftlichen Fakultät I
der Humboldt-Universität zu Berlin

von
Master-Physikerin Lien Tran

Präsident der der Humboldt-Universität zu Berlin:
Prof. Dr. Jan-Hendrik Olbertz

Dekan der Mathematisch-Naturwissenschaftlichen Fakultät I:
Prof. Dr. rer. nat. Andreas Herrmann

Gutachter:
1. Prof. T. Masselink – HU Berlin
2. Prof. H. Riechert – Paul-Drude-Institut
3. Prof. G. Salamo – University of Arkansas, USA

eingereicht am: 24. Februar 2011
Tag der mündlichen Prüfung: 13. April 2011

Abstract

This dissertation describes investigations of the growth by molecular beam epitaxy and the characterization of the semiconductor InSb as well as the diluted magnetic semiconductor (DMS) $In_{1-x}Mn_xSb$.

The InSb films were grown on GaAs (001) substrate and Si (001) offcut by 4^o toward (110) substrate up to a thickness of about 2 μm, in spite of a large lattice mismatch between the epi-layer and substrate (14.6% between InSb and GaAs, and 19.3% between InSb and Si). After optimizing the growth conditions, the best InSb films grown directly on GaAs without any special technique results in a high crystal quality, low noise, and an electron mobility of 41100 cm^2/Vs Vs with associated electron concentration of 2.9e16 cm^{-3} at 300 K. Such structures could be used, for example, for infrared detector structures.

The growth of InSb on Si, however, is a challenge. In order to successfully grow InSb on Si, tilted substrates and the insertion of buffer layers were used, which helps to reduce the lattice mismatch as well as the formation of defects, and hence to improve the crystal quality. An electron mobility of 24000 cm^2/Vs measured at 300 K, with an associated carrier concentration of 2.6e16 cm^{-3} is found for the best sample that was grown at 340^oC with a 0.06 μm-thick GaSb/AlSb superlattice buffer layer. The smaller value of electron mobility (compared to the best GaAs-based sample) is related to a higher density of microtwins and stacking faults as well as threading dislocations in the near-interface region as shown by transmission electron microscopy. Deep level noise spectra indicate the existence of deep levels in both GaAs and Si-based samples. The samples grown on Si exhibit the lowest Hooge factor at 300 K, lower than the samples grown on GaAs.

Taking the optimized growth conditions of InSb/GaAs, the diluted magnetic semiconductor $In_{1-x}Mn_xSb$/GaAs (001) is prepared by adding a few percent of Mn into the host material InSb during growth. I have investigated the properties of the samples with a range of low Mn content ($x < 1\%$). Mn decreases the lattice constant as well as the degree of relaxation of (In,Mn)Sb films. Mn also distributes itself to result in two different and distinct magnetic materials: the diluted magnetic semiconductor (In,Mn)Sb and clusters of ferromagnetic MnSb. The MnSb clusters dominate only on the surface as indicated by the structural characterization. The measured values of Curie temperature T_c Tc for these two materials are found to be highly dependent on Mn concentration. For the DMS alloy (In,Mn)Sb, the Curie temperature appears to be smaller than 50 K, whereas it is greater than 300 K for the MnSb clusters. The occurrence of the high T_c and and MnSb clusters on the surface suggest the possibility to obtain higher T_c by adding more Mn into the host material and etching the samples down to several ten nanometers from the surface to eliminate the MnSb clusters as well as annealing at low temperature to remove the Mn interstitial sites.

Zusammenfassung

Im Rahmen dieser Arbeit wurden InSb- und verdünnt-magnetische $In_{1-x}Mn_xSb$-Filme mittels Gasquellen-Molekularstrahlepitaxie hergestellt und deren strukturelle und elektronische Eigenschaften untersucht.

Die InSb-Dünnschichten wurden sowohl auf GaAs(001)-Substrat als auch um 4^o in Richtung [110] fehlgeschnittenem Si(001)-Substrat hergestellt. Trotz einer starken Gitterfehlanpassung (14,6% zwischen InSb und GaAs und 19,3% zwischen InSb und Si) wurden epitaktische Schichten bis zu einer Dicke von 2 μm realisiert und die Wachstumsbedingungen optimiert. Optimierte InSb-Schichten direkt auf GaAs zeigen eine hohe kristalline Qualität, niedriges Rauschen und eine Elektronenbeweglichkeit von 41100 cm^2/Vs bei 300 K. Die Ladungsträgerkonzentration beträgt etwa 2,9e16 cm^{-3}. Solche InSb-Filme können als aktive Medien für Infrarot-Detektoren verwendet werden.

Um InSb-Dünnschichten guter Qualität auf Si-Substrat zu realisieren, wurden fehlgeschnittene Substrate benutzt, die die Bildung von Defekten reduzieren und damit die Qualität der Kristalle verbessern. Zur Reduzierung der Gitterfehlanpassung wurden Pufferschichten gewachsen. Eine Elektronenmobilität von 24000 cm^2/Vs und Ladungsträgerkonzentration von 2,6e16 cm^{-3} wurden bei 300 K nachgewiesen. Diese Probe enthält ein 0,06 μm GaAs/AlSb-Supergitter als Pufferschicht (Wachstumstemperatur war 340^oC). Die Verringerung der Elektronenmobilität (verglichen mit der besten GaAs-basierten Probe) ist der höheren Dichte der Microtwins und Stapelfehler als auch den Threading-Versetzungen in der schnittstellennahen Region geschuldet. Diese Defekte sind anhand von Transmissionselektronenmikroskopieaufnahmen nagewiesen. Die Deep-Level Rauschspektren zeigen die Existenz von Deep-Levels sowohl in GaAs- als auch in Si-basierten Proben. Die InSb-Filme auf Si-Substrat zeigen einen kleineren Hooge-Faktor im Vergleich zu Schichten auf GaAs (300 K).

Unter Anwendung der optimierten Wachstumsbedingungen für InSb/GaAs wurden verdünnt-magnetische $In_{1-x}Mn_xSb$-Schichten auf GaAs (001)-realisiert. Die untersuchten Proben enthalten bis zum 1% Mangan. Mn verringert die Gitterkonstante und damit den Grad der Relaxation von (In,Mn)Sb-Filmen. In den Proben befindet sich Mn in zwei magnetischen Formen, sowohl als verdünnt-magnetischer Halbleiter (In,Mn)Sb, als auch als MnSb-Cluster. Die Cluster dominieren auf der Oberfläche, wie durch die Transmissionselektronenmikroskopieaufnahmen gezeigt wird. Die Curie-Temperatur, T_c, unterscheidet sich für die beiden Formen und hängt stark von der Mn-Konzentration ab. Für (In,Mn)Sb ist T_c kleiner als 50 K . Die MnSb-Cluster zeigen dagegen ein T_c über 300 K. Das hohe T_c und der Existenz von MnSb-Clustern auf der Oberfläche legt nahe, dass Erreichen von höheren T_c-Werten durch Hinzufügen von mehr Mn in das Wirtsmaterial möglich sein könnte. Die MnSb-Cluster sollten durch das Abtragen einiger zehn Nanometer der Oberfläche vollständig beseitigt werden können. Um die Mn-Zwischengitterplätze zu entfernen, sollten die Proben bei niedrigen Temperaturen getempert werden.

Parts of this work have been published as

Lien Tran, Fariba Hatami, Vasyl Kunets, Gregory Salamo, and W. Ted Masselink, *Comparison of MBE growth of InSb on Si (001) and GaAs (001)*, J. Electron. Mater. **37**, 1799-1805 (2008)

Lien Tran, Julia Dobbert, Fariba Hatami, and W. Ted Masselink, *Growth and characterization of InSb films on Si (001)*, Mater. Res. Soc. Symp. Proc. **1068**, C02-05 (2008).

Lien Tran, Jens Herfort, Oliver Bierwagen, Fariba Hatami, and W. Ted Masselink, *Narrow-gap ferromagnetic semiconductors (In,Mn)Sb on GaAs (001): growth and properties*, Phys. Stat. Sol. (c) **1-5** (2009)

Julia Dobbert, **Lien Tran**, Fariba Hatami, and W. Ted Masselink, Vasyl. Kunets and Gregory Salamo, *Low frequency noise in InSb/GaAs and InSb/Si channels*, Appl. Phys. Lett. **97**, 102101 (2010).

Lien Tran, Fariba Hatami, Jens Herfort, Achim Trampert and W. Ted Masselink, *Distribution of Mn in ferromagnetic (In,Mn)Sb films grown on (001) GaAs using MBE*, J. Crys. Growth. doi:10.1016/j.jcrysgro.2010.10.127, (2010).

Julia Dobbert, **Lien Tran**, Fariba Hatami, and W. Ted Masselink, Vasyl. Kunets and Gregory Salamo, *A comparison of the low frequency noise in InSb grown on GaAs and Si by MBE*, J. Crys. Growth. doi:10.1016/j.jcrysgro.2010.12.039, (2010).

Parts of this work have either been submitted or prepared

Julia Dobbert, **Lien Tran**, Fariba Hatami, and W. Ted Masselink, Vasyl. Kunets and Gregory Salamo, *Generation-recombination noise in InSb/GaAs and InSb/Si channels* (submitted to Appl. Phys. Lett. (2010)).

Lien Tran, Fariba Hatami, Karin Braune, W. Ted Masselink, Jens Herfort, Vasyl Kunets, Gregory Salamo, *Curie temperature in two magnetic phases of (In,Mn)Sb crystals grown on GaAs (100)* (will be submitted to J. Appl. Phys. (2011)).

Conference contributions

Lien Tran, and W. Ted Masselink, *Growth and characterization of high quality InSb films on GaAs*, the 10th Deutsche Physikerinnentagung 2006 (DPG2006), 2-5 November 2006, Berlin, Germany.

Lien Tran, Fariba Hatami, Vasyl Kunets, Gregory Salamo, and W. Ted Masselink, *Comparison of MBE growth of InSb on Si (001) and GaAs (001)*, the 49th Electronic

Materials Conference 2007 (EMC2007), 20-22 June 2007, Notre Dame, Indiana, USA.

Lien Tran, Julia Dobbert, Fariba Hatami, and W. Ted Masselink, *Growth and characterization of InSb films on Si (001)*, the MRS Spring Meeting 2008, 24-28 March 2008, San Francisco, California, USA.

Lien Tran, Jens Herfort, Oliver Bierwagen, Fariba Hatami, and W. Ted Masselink, the 35th International Symposium on Compound Semiconductors 2008 (ISCS2008), 21-24 September 2008, Europa-Park, Rust, Germany.

Lien Tran, Oliver Bierwagen, Vasyl Kunets, Fariba Hatami, W. Ted Masselink, *Magnetoresistance in the ferromagnetic semiconductor (In,Mn)Sb grown on GaAs (001)*, the 12th Deutsche Physikerinnentagung 2008 (DPG2008), 6-9 November 2008, Münster, Germany.

Lien Tran, Fariba Hatami, Jens Herfort, Achim Trampert and W. Ted Masselink, *Distribution of Mn in ferromagnetic (In,Mn)Sb films grown on (001) GaAs using MBE*, the 16th International Conference on Molecular Beam Epitaxy (MBE2010), 22-27 August 2010, Berlin, Germany.

Julia Dobbert, **Lien Tran**, Fariba Hatami, and W. Ted Masselink, Vasyl. Kunets and Gregory Salamo, *Low frequency noise in InSb*, the 16th International Conference on Molecular Beam Epitaxy (MBE2010), 22-27 August 2010, Berlin, Germany.

Symbols/Abbreviations

H, B	Applied magnetic field, flux density of magnetic field
M	Magnetization
T	Absolute temperature
T_c	Curie temperature
e	Electron charge
j	Current density
μ	Carrier mobility
n, p	Electron concentration, hole concentration
R_H	Hall coefficient
σ, ρ, R	Conductivity, resistivity, sheet resistance
h, $\hbar$	Planck constant, $h/2\pi$ - reduced Planck constant
k	Boltzmann constant
λ	Wavelength
c	Speed of light in a vacuum
m^*, m_e	Effective mass, mass of the free electron
E_C, E_V, E_F	Conduction band energy, valence band energy, Fermi energy
E	Energy
r	Growth rate
d	Thickness
t	Time
a	Lattice constant
ν	Poisson's ratio
0D, 1D, 2D, 3D	Zero-, one-, two-, three-dimensional
ML	Monolayer, equals half the lattice constant
MR	Magnetoresistance
DMS	Diluted magnetic semiconductor
MBE	Molecular beam epitaxy
MOCVD	Metal-organic chemical vapor deposition
UHV	Ultra high vacuum
RHEED	Reflection high energy electron diffraction
DCXRD	Double crystal x-ray diffraction
FWHM	Full width at half maximun
AFM	Atomic force microscope
SIMS	Secondary ion mass spectrometry
SEM	Scanning electron microscopy
SQUID	Superconducting quantum interference device
TEM	Transmission electron microscopy
AHE	Anomalous Hall effect
BEP	Beam equivalent pressure
RKKY	Ruderman-Kittel-Kasuya-Yosida
BL	Buffer layer

Contents

1 Introduction

Narrow band gap III-V compound semiconductors have been renewed interest for optoelectronic devices, high frequency electronics, and magnetic field sensors. InSb has small direct band gap (0.17 eV), low effective mass ($0.014m_e$), and high room-temperature electron mobility ($\sim$ 70000 cm^2/Vs). Therefore, it has been particularly attractive as a potential material for infrared detectors and high-speed devices. Epitaxial techniques such as molecular beam epitaxy (MBE), metalorganic chemical vapor deposition, and liquid phase epitaxy can be used to grow InSb films. The films can be fabricated on InSb, GaSb, or InAs substrates. But this method is not preferred due to low resistance of the substrate. Instead, GaAs and Si substrates are more used even though there is a significant lattice mismatch between substrate and epitaxial layer (lattice mismatch 14.6% between InSb and GaAs, and 19.3% between InSb and Si). In my thesis, thick InSb films were grown on GaAs (001) and vicinal Si (001) offcut by 4^o toward (110) substrates using MBE. MBE growth is accomplished by heating material sources in effusion cells in an ultrahigh vacuum chamber. Therefore, thermally induced atomic or molecular beams of the constituent elements are created and impinged on a substrate. Different growth parameters, conditions, and techniques have been examined to obtain high quality films, in particular with respect to high mobility. The best InSb sample grown directly on GaAs substrate at 310^oC[1] provides 300 K mobility of 41100 cm^2/Vs with a carrier concentration of 2.9e16 cm^{-3}. Fewer studies have been concerned with the heteroepitaxy of InSb on Si than on GaAs [1; 2; 3]. The difficulties involved in growth of high quality InSb films on Si include the large lattice mismatch, the different thermal expansion coefficients ($\alpha_{InSb} \approx 2\alpha_{Si}$ at 300 K) and antiphase domain formation due to the growth of anpolar semiconductor on a nonpolar semiconductor. Some problems have been eliminated by the use of tilted substrates [3], indium pre-deposition and the insertion of various buffer layers [4; 5; 6]. In my work, I used Si (001) offcut by 4^o toward (110) substrate and the insertion of buffer layers. The 300 K mobility of 24000 cm^2/Vs corresponding to a carrier concentration of 2.6e16 cm^{-3} was found for the best sample, which is grown at 340^oC[2] with $\sim$ 2 nm GaSb/AlSb superlattice buffer layer. The conductivity was n type and a degradation 60.4% of the electron mobility at 77 K was observed.

Diluted magnetic semiconductors (DMS) are characterized by the random substitution of a fraction of the original atoms by magnetic atoms, as schematically shown in Fig. 1.1. Therefore, they combine magnetic with semiconducting properties. The III-V ferromagnetic semiconductors have been extensively studied, especial those alloys with

[1] The thermocouple temperature was 350^oC. According to my estimation using high temperature calibration, this temperature is about 310^oC.

[2] The thermocouple temperature was 380^oC

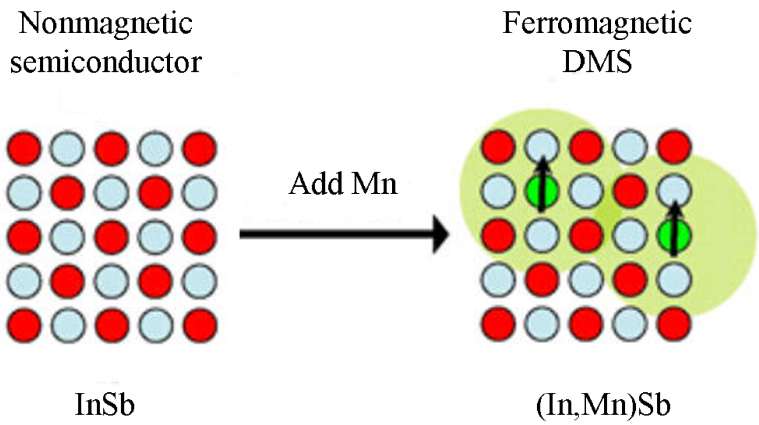

Figure 1.1: (Reproduced from www.als.lbl.gov) Schematic of nonmagnetic semiconductor InSb and DMS with ferromagnetic order mediated by holes.

the small lattice constants and large energy gaps such as (Ga,Mn)As, (Ga,Mn)N and (In,Mn)N, which are expected to provide the high Curie temperatures T_c. It is also very important to explore the opposite extreme of the family, (In,Mn)Sb, because it brings with itself new opportunities for applications in the far infrared spin-photonics and, due to its high carrier mobility, in devices based on spin-dependent transport [7; 8; 9]. Recently, Ganesan et al. [10] reported studies on bulk Mn doped InSb grown using the horizontal Bridgman technique. It has been found that a ferromagnetic state below 10 K is the consequence of (In,Mn)Sb alloy and other ferromagnetic component is related to MnSb clusters in the crystal. I prepared (In,Mn)Sb/GaAs by epitaxial technique MBE that allows to grow high quality crystal films and dope few percent of Mn. The optimized growth conditions for InSb/GaAs structures were used for the epitaxy of (In,Mn)Sb samples. All the samples were grown at the same conditions but with different Mn contents. For a comparison, a nonmagnetic InSb has been presented. Many experimental techniques, such as reflection high energy electron diffraction (RHEED), x-ray diffraction (XRD), atomic force microscope (AFM), scanning electron microscopy (SEM), transmission electron microscopy (TEM), Hall measurements, superconducting quantum interference device (SQUID) have been employed to investigate and characterize the films as well as the behavior of Mn atoms in the system. The Mn concentrations were estimated to be smaller than 1%. The presence of Mn in the InSb films decreases the average lattice constant as well as the degree of relaxation of (In,Mn)Sb films. Two magnetic states due to alloy (In,Mn)Sb and clusters MnSb on the surface have been observed. Both the (In,Mn)Sb alloy as well as MnSb inclusions are ferromagnetic and two distinct Curie temperatures are measured. The Curie temperature of dilute magnetic semiconductor depends on Mn concentration and is below 50 K, while the MnSb clusters exhibits distinct hysteresis loops above 300 K. The existence of such ferromagnetic clusters in these hybrid system may be important for semiconductor-based spinphotonics applications and devices with a higher Curie temperature.

This thesis is organized as follows:

- The second chapter shows some aspects of narrow band gap semiconductor InSb, and III-V diluted magnetic semiconductors, particularly (In,Mn)Sb.
- The preparation of InSb/GaAs, InSb/Si, and (In,Mn)Sb/GaAs structures, involving the substrates preparation, growth conditions as well as experimental growth techniques are given in chapter 3.
- In chapter 4, properties of InSb/GaAs and InSb/Si systems, in particular with respect to the structural and electrical analysis are discussed.
- Chapter 5 provides the detailed studies related to (In,Mn)Sb/GaAs system, such as the lattice parameter, the investigation of negative magnetoresistance and anomalous Hall effect, the Mn distribution and Curie temperature.
- Conclusions and outlook are given in chapter 6.

2 Some features of III-V narrow band gap semiconductors and diluted magnetic semiconductors

InSb with a narrow energy band gap has provided an exciting field of research and exposed a number of extreme physical and material characteristics. A new class, as known as diluted magnetic semiconductor: in which a fraction of its constituent ions are replaced by magnetic ions, is also providing renewed interest in the underlying physics. In this chapter, some fundamental properties and a brief overview of the epitaxial growth of InSb narrow band gap semiconductor and diluted magnetic semiconductors are described in detail. Section 2.1 deals with properties and a review of the epitaxy of InSb, while section 2.2 is followed with a report of III-V diluted magnetic semiconductors, especially (In,Mn)Sb.

2.1 III-V narrow band gap semiconductors InSb

2.1.1 Introduction

InSb is a zinc blende crystal structure made from the elements indium (In) and antimony (Sb) (Fig. 2.1). There are three most important parameters of a semiconductor for device applications: the band gap, the lattice constant, and the mobility. InSb has the smallest band gap from the binary III-V semiconductor group. The band structure of InSb at 300 K is shown in Fig. 2.2. The conduction band minimum and the valence band maximum occur at the Γ points (a direct energy band gap). The band gap referred to the energy difference between them is 0.17 *eV*. The *V1* valence band, with a large density of states (large effective mass) is normally called the heavy hole band. A similar manner the *V2* valence band is called the light hole band. The *V1* and *V2* valence bands happen to have the same energy at their upper extremum. The *V3* valence band is known as the split-off band. The energy separation marked as 0.8 *eV* is the spin-orbit splitting. The *V3* valence band is low enough to remain unpopulated by free holes distributed between the uppermost states of the *V1* and *V2* bands. The conduction bands of InSb are less complex than the valence bands. The lowest conduction band minimum is

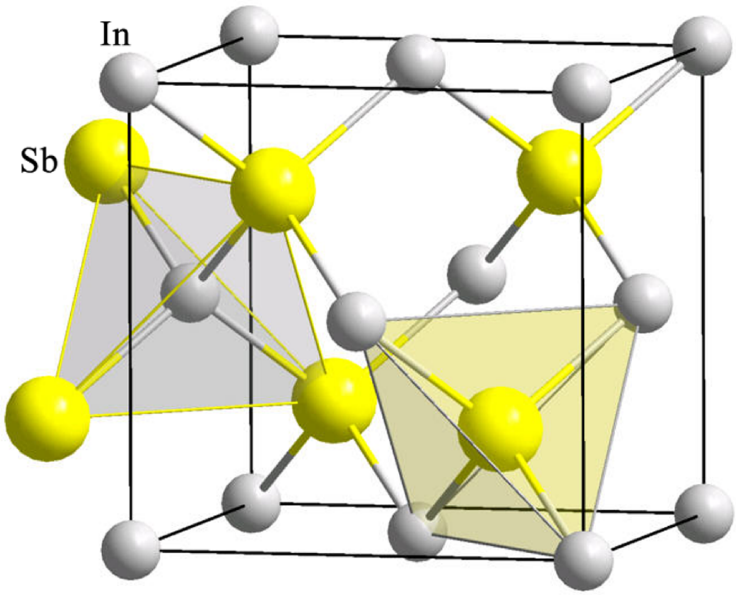

Figure 2.1: (From www.wikipedia.org) InSb crystal structure.

marked as Γ_6. At thermal equilibrium the upper conduction band valleys marked L_6 do not contain any free electrons, but electron can be exited from Γ_6 in to L_6 in a large electric field. Of course, InSb has other conduction bands. But figure 2.2 shows only the lowest two of these. The higher ones are not involved in quasi-equilibrium studies of the semiconductor, but they still influence the optical and photoemissive properties in the visible and ultraviolet parts of the spectrum [11].

For semiconductor with a zinc-blende structure, the lattice constant a is defined by the spatial extent of the face-centered cubic sub-lattices. Figure 2.3 shows the band gap and corresponding wavelength versus lattice constant of several elementary and binary III-V semiconductors at room temperature. By controlling the concentration of the constituent semiconductor, one can tailor the band gap and the lattice constant of semiconductor alloys. InSb with the narrowest band gap (0.17 eV) and the largest lattice constant (6.48 Å) in the binary III-V group delimits the wavelength range for optical devices based on InSb structure in the infrared region. As InSb grown on a substrate, the layer adopts the in-plane lattice spacing. The difference in lattice constant between InSb (a_L) and substrates (a_S) leads to a compressive strain in InSb layers grown on these substrates. For the growth of InSb on GaAs substrate (lattice constant a_S of 5.65 Å) and Si substrate (lattice constant a_S of 5.43 Å), the epi-layer has a smaller lattice constant than the substrate. Thus, it results in a lattice mismatch ε of 14.6% between InSb and GaAs and 19.3% between InSb and Si ($\varepsilon = \frac{a_L - a_S}{a_S}$). In the InSb/GaAs system, both materials have a zinc-blende crystal structure. Therefore, InSb adopts the in-plane lattice constant of GaAs. The deposited layer is either fully strained, partly relaxed, or fully relaxed. Figure 2.4 illustrates the two limiting cases of a fully strained (a) and a fully relaxed (b) semiconductor epi-layer that has a bigger lattice constant than the substrate. If the deposited layer is much thinner than the substrate, the substrate

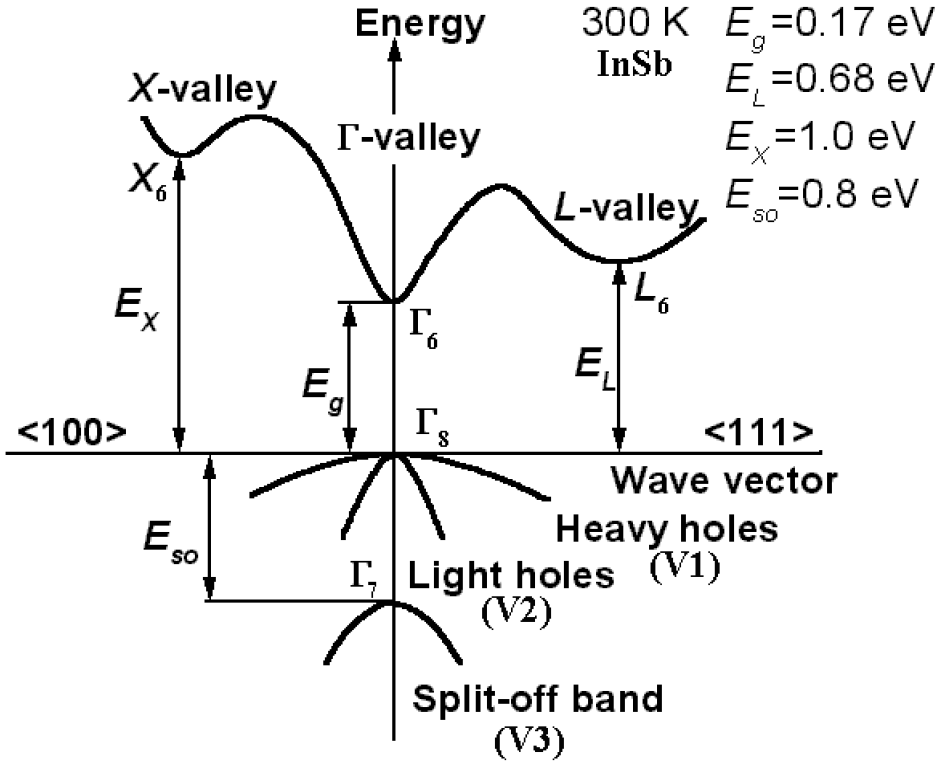

Figure 2.2: (Reproduced from http://www.ioffe.ru) Band structure of InSb at 300 K.

maintains its relaxed lateral lattice constant, and the mismatch is accommodated in the layer. As seen in Fig. 2.4(a), the thin layer grown on top of substrate is fully strained by assuming the smaller lattice constant of the substrate ($a_L^{\parallel} = a_S^{\parallel}$). The epi-layer is biaxially compressed in-plane with the in-plane strain component $\varepsilon_{\parallel}$ and expanded vertically resulting out of plane strain component $\varepsilon_{\perp}$

$$\varepsilon_{\parallel} = \frac{a_L^{\parallel} - a_L}{a_L} \tag{2.1}$$

$$\varepsilon_{\perp} = -\frac{\varepsilon_{\parallel}}{\nu} \tag{2.2}$$

where ν is Poisson ratio of the layer and has a value of 0.35 for InSb [12]. The vertical lattice constant of the strained layer is

$$a_L^{\perp} = a_L(1 + \varepsilon_{\perp}) \tag{2.3}$$

If the thickness d of the deposited layer increases, the total strain energy in the deposited layer also increases. Until d exceeds a critical thickness, the strain can be relaxed by the formation of dislocations in the interface between epi-layer and substrate (Fig. 2.4(b)). Dislocations can be the lines of defects that form when a part of the

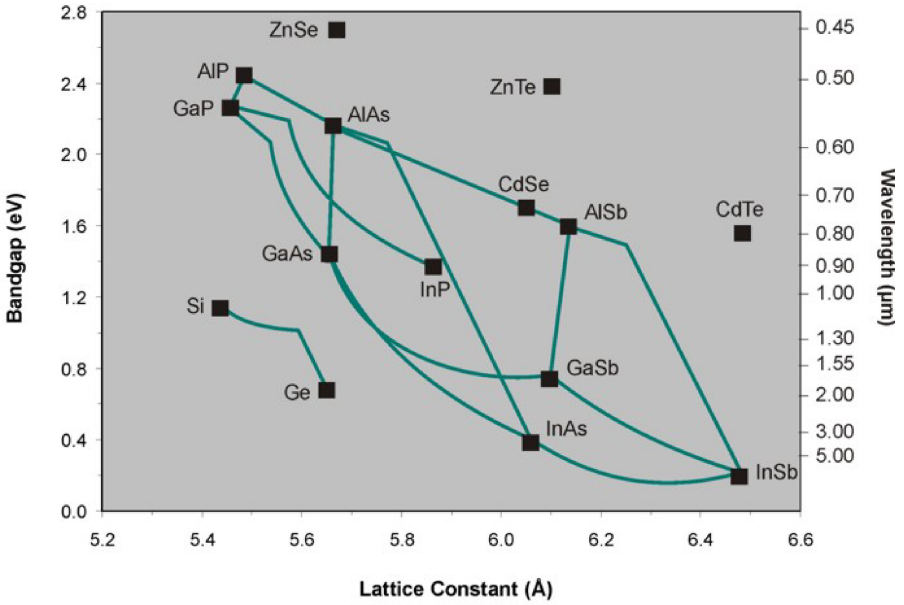

Figure 2.3: (From http://www.veeco.com) Energy gap and corresponding wavelength versus lattice constant at 300K of several elementary and binary semiconductors with a zinc-blende structure. Labeled dots denote the elementary and binaries, whereas the connection lines mark the band gaps and lattice constants of the pertinent semiconductor alloys.

crystal overlaps relative to another part [13].

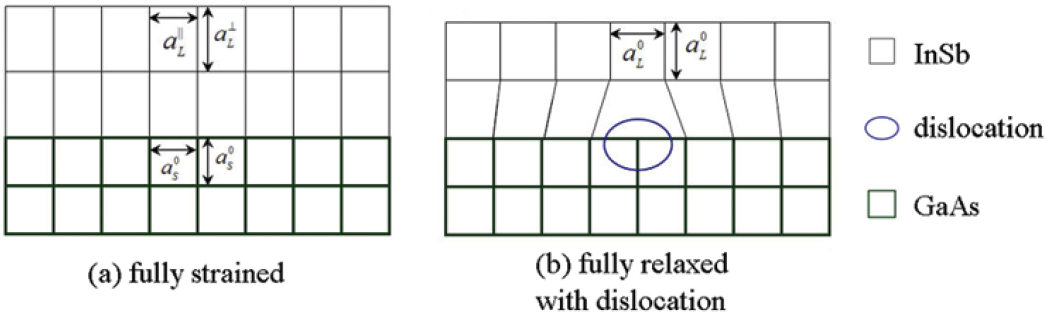

Figure 2.4: Fully strained (a) and fully relaxed (b) semiconductor layer with a larger lattice constant than the substrate.

In addition to narrow band gap and large lattice constant, InSb has a high room-temperature electron mobility of 70000 cm^2/Vs. Due to these unique properties, InSb provides many applications such as infrared detectors, Hall devices, as well as fast transistors in terms of dynamic switching [14; 15; 16; 17; 18; 19; 20; 21]. The InSb detectors are sensitive between 1-5 μm wavelengths. The InSb photodetectors fabricated by MBE have been reported over the years. Kimukin *et al.* [14] introduced the high-speed operation of the InSb-based p-i-n photodetectors grown on GaAs substrate in the mid-IR. Electrical and optical properties of photodetectors with active areas ranging from 7.06e-6

cm^2 to 2.25e-4 cm^2 measured at 77 K and 300 K, respectively. Detectors had high zero-bias differential resistances, and the differential resistance area product was 4.5 Ωcm^2. At 77 K, spectral measurements yielded high responsivity between 3 and 5 μm with the cutoff wavelength of 5.33 μm. The maximum responsivity for 80-μm diameter detectors was 1.00e5 V/W at 4.35 μm while the detectivity was 3.41e9 $cm\sqrt{Hz}/W$. High-speed measurements were done at room temperature. An optical parametric oscillator was used to generate picosecond full-width at half-maximum (FWHM) pulses at 2.5 μm with the pump at 780 nm. 30-μm diameter photodetectors yielded 3-dB bandwidth of 8.5 GHz at 2.5 V bias. The InSb infrared photodetectors grown heteroepitaxially on Si substrates by MBE are reported by Michel *et al.* [15]. Excellent InSb material quality is obtained on 3-inch Si substrates (with a GaAs predeposition) as confirmed by structural, optical, and electrical analysis. InSb infrared photodetectors on Si substrates that can operate from 77 K to room temperature have been demonstrated. The peak voltage-responsitivity at 4 μm is about 1.0e3 V/W and the corresponding Johnson-noise-limited detectivity is calculated to be 2.8e10 $cm\sqrt{Hz}/W$. This was the first important stage in developing InSb detector arrays or monolithic focal plane arrays (FPAs) on silicon. The development of this technology could provide a challenge to traditional hybrid FPA in the future. Singh *et al.* [16] reported the growth of high quality InSb p-i-n structures which have been optimized using reflection high energy electron diffraction. Optimized InSb p-i-n structures of 5.8 μm thickness demonstrated x-ray full width at maximum (FWHM) of 101 and 147 arcsec for GaAs and Si substrates, respectively, and exhibited excellent uniformity and morphology. Prototype InSb p-i-n detectors on Si have been fabricated and have demonstrated photovoltaic response at 6.5 μm up to 200 K. A 4.8-μm-thick InSb layer grown on GaAs at a growth temperature of 395^{o}C and a III/V incorporation ratio of 1/1.2 had an x-ray rocking curve FWHM of 158 arcsec and a Hall mobility of 92300 cm^2/Vs at 77 K.

Micro-Hall sensor arrays were developed by using InSb thin films. Togawa *et al.* [17] introduced an InSb thin-film linear micro-Hall sensor array of eight sensors, each with a sensitivity of 10 $nT/Hz^{1/2}$ developed for biomedical applications. The individual Hall sensors had an active area of 5 μm $\times$ 5 μm and were separated by a distance of 5 μm. A combination of these Hall devices and a magnetization system incorporating both dc and ac bias magnetic fields, enabled the simultaneous detection of multiple 2.8 μm diameter superparamagnetic beads. Nano scale Hall probes (currently mostly based on GaAs) have to be employed to measure highly inhomogeneous magnetic fields. Recently, some Hall probes have been manufactured with an active area of only 100 nm $\times$ 100 nm [18] (while conventional Hall probes have an active area of 100 μm $\times$ 100 μm) [19]. These can be used to make magnetic field detections in the nano-Tesla range possible [20; 21].

InSb is renewed studied to construct very fast transistors that use one-tenth of the energy of existing components. In the late 1990s, bipolar transistors constructed from InSb operated at frequencies up to 85 GHz. Researchers at US Intel and UK QinetiQ also used InSb and developed transistors. Recently, they have been reported field-effect transistors operating at over 200 GHz. Transistors act as switches or amplifiers in electronic circuits to process information. Due to highly active and greater number of carriers, InSb allows electrons to speed through faster than conventional silicon-based

transistors. While the transport characteristics of these carriers are exhilarating, there is a downside: they also make these transistors more difficult to control than silicon-based ones, except at low temperatures, around 77 K. The researchers have then sandwiched pure InSb between layers of AlInSb to improve the transistors. The isolated pure InSb layer acts as a quantum well. Therefore, electrons are confined: not only travel with high speed but also are controlled at very low voltage. It is also capable to operate InSb devices with voltages under 0.5 V, reducing their power requirements. "Indium antimonide is one example of several new materials that Intel will continue to investigate in order to ensure that Moore's Law extends well beyond the next decade" says Ken David - director of components research for Intel's Technology and Manufacturing Group. (From www.compoundsemi.com).

2.1.2 Epitaxial growth of narrow band gap semiconductor InSb

Recent improvements in epitaxial techniques have led to the availability to grow compound semiconductor films with high quality. InSb can be enabled on several substrates by a varity of epitaxial methods such as metalorganic chemical vapor deposition (MOCVD), liquid phase epitaxy (LPE) and molecular beam epitaxy (MBE).

InSb on GaAs

The growth of InSb on GaAs substrates ($\sim 14.6\%$ lattice mismatch) has been studied by many groups. In an earlier work, Bosch [22] reported the growth of InSb on the nonpolar GaAs (110) surface. The epitaxial films with a thickness from 1-7.7 μm showed n-type conductance and mobilities at 77 K, μ_{77}, of 12000-75000 cm^2/Vs. It was concluded that the higher values of mobilities can be achieved by optimizing the growth conditions.

Ohno *et al.* [23] also reported the growth of high-quality InSb films on GaAs (001) using MBE. The films provided room temperature mobility of 55000 cm^2/Vs with a carrier concentration of 5e15 cm^{-3}. The conductivity was n type even down to 13 K and no degradation of the electron mobility due to the high density of dislocations was observed.

Parker *et al.* [24] investigated later the MBE growth and Si doping of InSb on GaAs (100). At low growth temperatures, $\sim 340^oC$, Si acted only as a donor and could produce electron concentrations from 1e17 to 3e18 cm^{-3} and mobilities at 77 K identical to those of bulk material. Although higher concentrations could be achieved, autocompensation occurred above 3e18 cm^{-3} since the measured value of the carrier concentration at 77 K was lower than expected. At $n = 1.2e17$ cm^{-3}, the value of μ_{77} was above 40000 cm^2/Vs in 1-μm-thick films. Electrical properties were effected by defects at the interface between the GaAs substrate and the InSb layer. By introducing a 1300-Å-thick doped slab at various distances d between the interface (d=*0* μm) and the surface of the epilayer ($d \simeq 1.5$ μm), it was shown that the mobility degraded more than a factor of 2 when the doped slab is located at the interface.

The growth of InSb on GaAs using MBE with an employment of a thin InSb layer at the GaAs interface grown by an atomic layer epitaxy (ALE) process was studied by Thompson [25]. A 300 Å buffer layer of InSb was grown by ALE at a substrate temperature of 300^{o}C at the GaAs/InSb interface before the growth of bulk-like properties InSb films. The primary InSb layer was grown at 420^{o}C with an atomic flux ratio of Sb to In of 1.4 and a growth rate of 1 μm/h after optimizing the growth conditions. It has been observed the reduction of the defects in the top InSb film. The best 5-μm-thick InSb layers had x-ray rocking curve widths of 100 arcsec, n-type carrier concentrations at 77 K in the range of e15 cm^{-3}, and carrier mobilities greater than 100000 cm^2/Vs. Mesa isolated photodiodes were also fabricated and had carrier lifetimes of 20 ns, in comparison to 200 ns observed in bulk InSb with a similar carrier concentration.

Songpongs *et al.* [26] investigated the conductance at the free surface or at an interface to a cap layer in Si-doped InSb on GaAs (001). A 0.5-μm-thick GaAs buffer layer was grown first on substrate before deposited 1.9-μm-thick layer of undoped bulk InSb. The structure was then followed by 1000-Å-thick Si-doped InSb with or without a cap layer of 500 Å GaAs or GaSb. The 1000-Å-thick doping layer play a role of providing electrons to the undoped bulk layer. The type of cap layer effects on both carrier concentrations and mobilities, especially in the temperature range 100-250 K. The structure has a dominant p-type conduction which is responsible for singularities in carrier concentration at $\approx$ 50 K and $\approx$ 90 K in the GaAs-cap sample and an enhanced conduction with a GaSb cap, respectively.

High mobility InSb films grown on GaAs (001) substrate with thick AlSb and InAlSb step-graded buffer (SGB) layers were investigated by Sato [27]. The structure consists some buffer layers (first 200 nm GaAs grown at 600^{o}C, next 20 nm AlAs grown at 640^{o}C, then 1μm AlSb grown at 400^{o}C, after that 1μm AlSb grown at 500^{o}C, finally $In_xAl_{1-x}Sb$ grown at 420^{o}C: from $x = 0.1$ to 0.9; thickness of about 0, 100, 500, 1000 nm), followed 2-μm-thick InSb layer grown at 460^{o}C. It was observed that the electron mobility increases as the SGB thickness increases. In contrast, sheet carrier concentration exhibits almost the same value. A sample with the 1000 nm SGB showed very high room temperature mobility of about 56000 cm^2/Vs. Surface roughness and mosaicity do not influence directly on the mobility.

Using a similar method of two-step growth process, Debnath *et al.* [28] grew InSb thin films on GaAs (001) substrate. The best 2-μm-thick InSb film had an X-ray rocking curve width of 277 arcsec and room-temperature Hall mobilities of 55000 cm^2/Vs, corresponding to the carrier concentrations of 1.5e16 cm^{-3}. A low defect density due to confinement of the dislocation in the InSb/GaAs interface has been seen.

Recently, Chyi *et al.* [29] has reported the MBE growth of InSb on GaAs (100) substrates. Remarkably good morphologies were obtained despite the large lattice mismatch (14.6%) between InSb and GaAs. Room-temperature electron mobilities as high as 57000 cm^2/Vs with $n_D - n_A \sim 1.6e16$ cm^{-3} were measured in 5-μm-thick InSb layers. The substrate temperature and Sb/In flux ratio were found to critically effect on the quality of InSb films.

InSb on Si

The difficulties to grow high quality InSb films on Si include the large lattice mismatch (>19%), the different thermal expansion coefficients ($\alpha_{InSb} \approx 2\alpha_{Si}$ at room temperature), and antiphase domain formation due to the growth of a polar semiconductor on a nonpolar semiconductor. Therefore, fewer works have been done on the heteroepitaxy of InSb on Si than on GaAs.

In an earlier work, Chyi *et al.* [1] introduced the growth of InSb on Si substrates tilted 4^o off (100) towards (110). InSb layers were grown either directly on substrate or after GaAs buffer layer. For 3.2-μm-thick layers, high room temperature electron mobilities were shown: 48000 cm^2/Vs and 39000 cm^2/Vs with and without a 0.2 μm GaAs buffer, respectively. One sample with a thickness of 8 μm showed narrower width of x-ray rocking curves, sharper band-edge transmission curves, and higher electron mobilities of 55000 cm^2/Vs.

Lu *et al.* [3] reported the growth of thin (< 1000 Å) InSb films on Si wafers with a sandwich-type fluoride buffer, BaF_2/InSb/BaF_2. The interface properties were examined by Auger electron spectroscopy and the InSb films were characterized by X-ray and Hall mobility measurements. It was found that thin InSb films with high electron mobility can be obtained by using this sandwich-type buffer layer.

As same as the method of Lu to insert fluoride buffer layers in order to reduce the lattice mismatch between epi-layer and substrate, Liu *et al.* [4] accomplished InSb on Si using CaF_2 buffer layers. Si(111) and Si(001) substrates were used. In the case of the growth on CaF_2/Si(111) substrate, In-terminated InSb(111) was produced by opening the In and Sb shutters simultaneously at substrate temperatures between 300^{o}C and 400^{o}C. The thickness of grown InSb films was about 0.32-8 μm. Experimental measurements indicated that a good crystalline quality of InSb layers. A high electron mobility at room temperature of 65000 cm^2/Vs was found for 8-μm-thick layer. On CaF2/Si(001) substrates, the InSb layers grew in the (111) orientation with two domains 90^o apart. The 4-μm-thick layer had room temperature electron concentration of 2.7e16 cm^{-3} corresponding to mobility of 9973 cm^2/Vs. The crystalline quality and electrical properties of these films, as the author expected, were worse than those grown on (111) oriented substrates. A reason was added that these structures were probably not grown under optimum conditions.

The growth of high-quality InSb films on Si(111) substrates without buffer layers was published by Rao [30]. A temperature range, 170-400^{o}C, was examined. Up to growth temperature of 300^{o}C surface morphology and epitaxial quality of the film improve with increasing temperature. But after 300^{o}C, a deterioration in the quality of the film was seen with an increase in growth temperature. The electron mobility of the film increases with growth temperature and the highest electron mobility at room temperature of about 2200 cm^2/Vs for the film grown at 300^{o}C was obtained. This is significantly less than the one of 70000 cm^2/Vs observed in bulk InSb. However, an improvement in the electrical properties could be achieved using a two-step growth procedure. The first consisted 300-Å-thick interface layer growth at 300^{o}C. The second followed by growth at 400^{o}C. The electron mobility at room temperature of a 1.8-μm-thick film grown by this method was 23000 cm^2/Vs.

Later, Mori *et al.* [6] added AlSb (lattice constant of 6.1355 Å) buffer layers for the

heteroepitaxial growth of InSb films on a Si(001) substrate. It can help to reduce the large lattice mismatch of about 19.3% between Si and InSb to about 5.6%. The thickness of the InSb layers was between 0.8 and 1.0 μm. The substrates temperatures ranged from 180 to 430^{o}C. The Sb/In flux ratio was about 4.7. The samples grown at 280^{o}C and 330^{o}C gave good crystal quality and surface morphology. At room temperature, sample grown at 280^{o}C showed electron mobility about 8000 cm^2/Vs and the carrier concentration about 4.7e17 cm^{-3}, whereas the sample grown at 330^{o}C had electron mobility about 11000 cm^2/Vs and carrier concentration about 5.9e17 cm^{-3}. It is found that the growth temperature about 300^{o}C is optimized to obtain the InSb films with smooth surface and good crystal quality.

In other work of Mori *et al.* [31], InSb films were deposited on Si (111) substrate with a InSb bi-layer at high growth temperature. The InSb bi-layer is prepared by the adsorption of 1 monolayer Sb atoms onto In-induced surface reconstruction on a Si(111) substrate. The influence of substrate temperature of first layer deposition on the two-step growth procedure was firstly studied. The RT electron mobility of the InSb film which was demonstrated on a Si(111) substrate at 420^{o}C with a InSb bi-layer was about 20000 cm^2/Vs.

During my thesis, I worked and we have also published the growth and properties of InSb films grown on GaAs and Si substrates using MBE [32; 9; 33; 34; 35]. The details will be discussed in the next chapters.

2.2 III-V diluted magnetic semiconductors

2.2.1 Introduction

The charge, mass, and spin of electrons are the most important features in the technology developments. Integrated circuits and high-frequency devices, which are used for information processing and communications, have had many success using the charge of electrons in semiconductors. Mass storage of information is carried out by magnetic recording (like hard disks, magnetic tapes, and magneto-optical disks) using spin of electrons in ferromagnetic materials. To date both the charge and spin of electrons can be used to further enhance the performance of devices.

A new electronics, called as spintronics (spin-transport based electronics) (Fig. 2.5), brings an ability to utilize the spin degree of the charge carriers in addition to its electronic charge. It is then possible to use the capability of mass storage and processing of information at the same time. It is also able to inject spin-polarized current into semiconductors to control the spin state of carriers. This approach can be followed by introducing magnetic elements into nonmagnetic semiconductors to make them magnetic. This category is termed diluted magnetic semiconductors (DMS), in which magnetic atoms introduced as impurities have moments on only a small fraction of all original atomic sites (Fig. 2.6) and combined therefore magnetic with semiconducting prop-

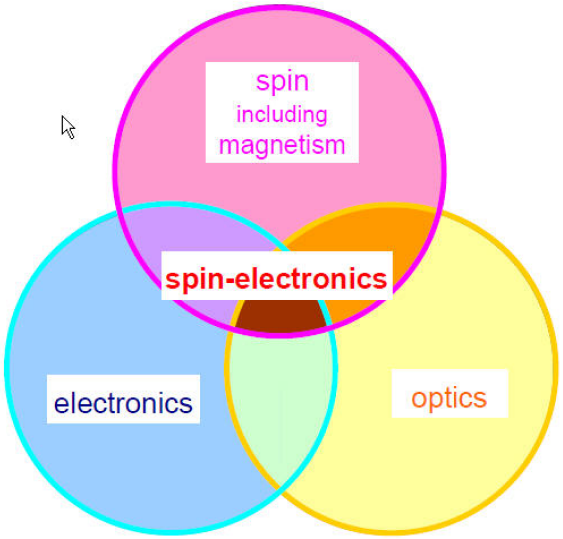

Figure 2.5: A schematic of spintronics. Spin, electronic and optical properties are utilized at the same time [36].

erties. Studies of DMS have concentrated most extensively on II-VI semiconductors, such as CdTe and ZnSe, in which the valence of the cations matches that of the common magnetic ions. This phenomenon makes these DMS relatively easy to prepare in both bulk form and thin epitaxial layers. But it is difficult to create p- and n-type in doped II-VI DMS, which made the material less attractive for applications. In addition, the magnetic interaction in II-VI DMS is dominated by the antiferromagnetic exchange between the Mn spins. This results in the paramagnetic, antiferromagnetic, or spin- glass behavior of the material. It was impossible to obtain ferromagnetic properties at low temperature in modulation doped quantum well structures based II-VI DMS [37]. In approach, (III,Mn)V DMS are more compatible with the semiconductors used in present-day electronics. The semiconducting properties are essentially the same as the host III-V compound, with a change in the band gap. When Mn atom substitutes the group III sites, it gives a local moment as well as a free hole for conduction. As the five electrons in the unfilled 3d shell of the Mn-ion give rise to localized magnetic moments, strongly interaction with the band electrons occurs via an exchange mechanism. This terminology recognizes that Fermi statistics is the ultimate origin [38]. Some of mechanisms, which couple localized spins in a semiconductor, have been identified. Heisenberg's direct-exchange [39] occurs between two local spins. It results the difference between the Coulomb energy of an antisymmetric singlet spin wave function state and a symmetric triplet spin wave function state. Kramer's super-exchange interaction [40] applies to local moments that are separated by a nonmagnetic atom. While moving from the nonmagnetic atom to an empty shell of the magnetic atom, an electron can interact (through the direct-exchange) with electrons forming its local moment. The nonmagnetic atom is polarized and coupled with all its magnetic neighbors (through the direct-exchange). In (III,Mn)V materials, super-exchange provides an anti-ferromagnetic

contribution to the interaction between Mn local moments on neighboring cation sites. Within the Zener [41; 42] approach, a double exchange mechanism, assuming an intermediate nonmagnetic atom, is given. In the context of III-V magnetic semiconductors, this interaction occurs when Mn acceptor states form an impurity band with mixed spd character. Thus, electrical conduction and Mn-Mn exchange coupling are both realized within an impurity band. This double-exchange plays a potentially importance role at lower Mn doping and in wide band gap (III,Mn)V materials. Other version of Zener's exchange is kinetic-exchange (indirect-exchange interaction). In this model, the coupling of local moments (usually on d-shell or f-shell) is mediated by s- or p-band itinerant carriers. Both ferromagnetic direct-exchange interaction (with band electrons on the same site) and anti-ferromagnetic interaction (due to hybridization between the local moment and band electrons on neighboring sites) can be happened [43; 44]. Due to the interaction, band electrons are polarized at one site and neighboring sites. If the band carrier polarization is weak, the celebrated Ruderman-Kittel-Kasuya-Yosida (RKKY) mechanism, originally applied to carrier-mediated indirect coupling between nuclear moments and between local d-shell moments in metals, is expected to dominate [45; 46]. The potential importance of this type of mechanism is greater in (III,Mn)V ferromagnetism, such as (Ga,Mn)As, (In,Mn)As, and Mn-doped antimonides. It is not very clear to distinguish impurity-band double-exchange and kinetic-exchange interactions. In a strong-coupling, narrow-band limit system, the former is more employed than the latter [38].

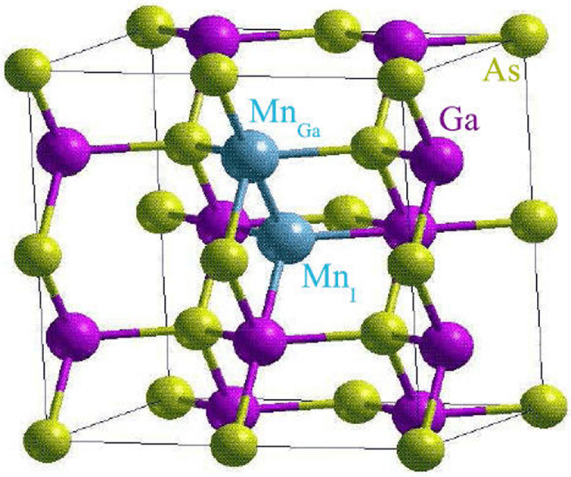

Figure 2.6: Illustration of (Ga,Mn)As DMS. Positions of substitutional Mn_{Ga}, and the less common interstitial Mn_I are indicated [38].

In order to observe magnetic cooperation in III-V DMS systems, we need to introduce a few percents or more of magnetic elements in III-V semiconductors. It was demonstrated that the incorporation of magnetic Mn ions into III-V semiconductors is limited to approximately 0.1% under equilibrium growth conditions. Even with this small doping level, surface segregation and phase separation occur. However, the advances of the non-equilibrium low temperature MBE (LT-MBE) techniques can lead to the successful

growth until more than 1% Mn in GaAs-based DMS [47; 36; 48; 49; 50; 51; 46; 52; 53; 54; 55; 56; 57; 58; 59; 60; 61; 47; 62; 63; 64; 65; 66; 67; 68; 69] and InAs-based DMS [70; 71; 72; 73; 74; 75; 76; 77; 78; 79]. More recently, several extended studies cover the the MBE growth of related heterostructures such as (Ga,Mn)N [80; 81; 82; 83; 84; 85; 86; 87; 88], (Ga,Mn)Sb [89; 90], and (In,Mn)Sb [91; 9; 92; 93; 7; 94].

2.2.2 Review of the growth of diluted magnetic semiconductor (In,Mn)Sb

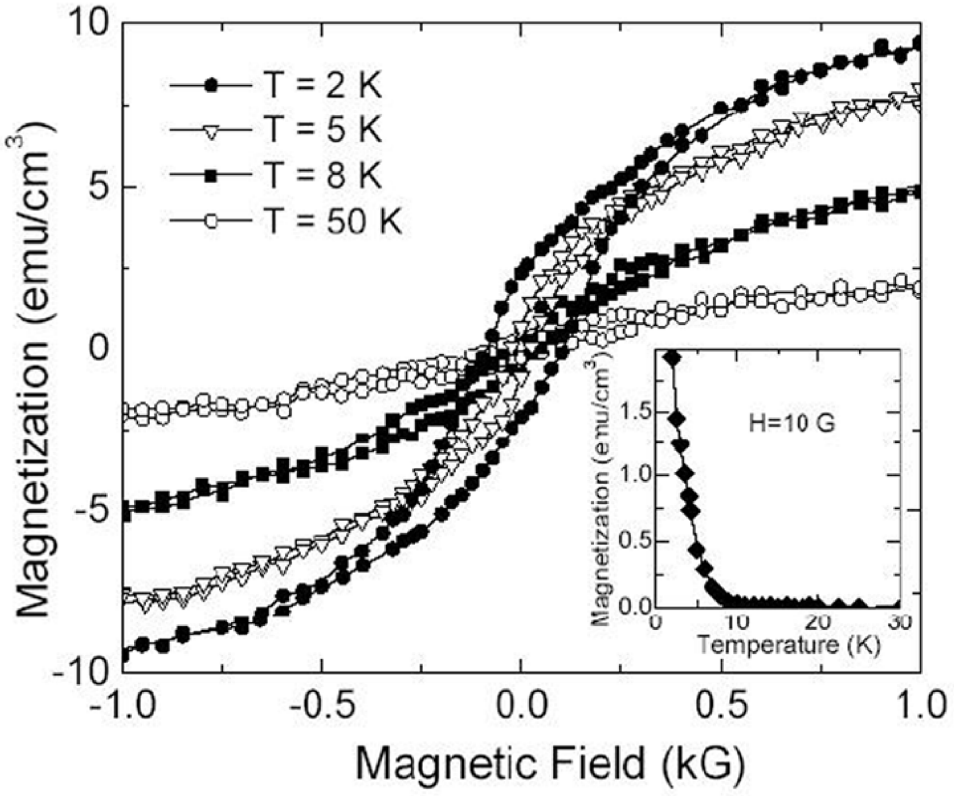

Figure 2.7: Present of hysteresis loops in magnetization measurements in $In_{1-x}Mn_xSb$ film with x = 0.028. The field was applied perpendicular to the layer plane. The inset indicates the Curie temperature of $\sim$ 9 K [95].

More recently, the research activity has focused extremely on the opposite extreme (in term of the largest lattice constant and the smallest hole effective mass) in the III-V based DMS: (In,Mn)Sb.

In the 1990s, the properties of (In,Mn)Sb single crystals grown using the Czochralski method have been reported [92; 93]. The Mn concentration is below 3.5e17 cm^{-3}. In this crystal, Mn behaves as a shallow acceptor (activation energy E_a = 7 meV). At low

temperature, the field-induced insulator-to-metal transition in the crystal occurs due to a strong spin-dependent coupling between the Mn spins and holes. The Mn spins interact each other predominately anti-ferromagnetic. A large magneto-resistance effect and an anomalous Hall effect have been observed.

Recently, Wojtowicz *et al.* [7; 96; 94; 95; 97] have largely presented results obtained on (In,Mn)Sb in both experiment as well as theory. $In_{1-x}Mn_xSb$ alloys were grown on CdTe/GaAs hybrid substrates using LT-MBE [7; 94]. The growth temperature was 170^{o}C for the growth of 230-nm-thick $In_{1-x}Mn_xSb$ film with the growth rate of 0.26 ml/s. Mn compositions x were obtained from Rutherford backscattering and particle-induced x-ray emission (RBS/PIXE) to be 0.02 and 0.028. Ferromagnetic order, by the present of clear hysteresis loops in both magnetization measurements and anomalous Hall effect directions, was observed. No other crystallographic states (e.g., MnSb) was seen. The Curie temperature T_C ranges up to 8.5 K (Fig. 2.7). It was considered a theoretically model, as the simplest mean-field theory, to estimate the T_C due to exchange and correlation in the itinerant-hole system [98; 99; 100]. A detailed study of magnetic scattering processes in the sample with $x = 0.02$ has also investigated [97]. It was found that Mn^{2+} ions locate outside the ferromagnetic ordered regions, leading to a reflection of the positional disorder of the magnetic moments in the saturating nature of both magnetization and magneto-resistance. The p-d exchange between spin-polarized charge carriers and localized Mn^{2+} is proposed to explain the observed phenomena both above and below the ferromagnetic phase transition.

More recently, Ganesan *et al.* [101; 10; 102] has also published the growth and properties of $In_{1-x}Mn_xSb$ films grown on GaAs. The films were grown with small Mn concentrations ($x = 0.0085$, 0.018, 0.029, and 0.04) by nearly equilibrium technique liquid phase epitaxy. With very high growth temperature of 525^{o}C (just below the melting point of InSb of 525.7^{o}C), the films were deposited for the thickness between 50 and 150 μm [101]. For the sample with highest Mn composition of 0.04, SEM revealed the presence of clusters. There was a magnetic phase change below 10 K which may originate from the ferromagnetic matrix. Meanwhile, the saturation in magnetization at 300 K was consequent of the ferromagnetic clusters MnSb, which has T_C above room temperature 300 K ($T_C = 587$ K). Electrical properties of the films at 1.3 K and 300 K has been given in Fig. 2.8.

Nominal film composition (x)	Thickness (μm)	Resistivity ρ ($\times 10^{-3}$ Ω cm)		Carrier conc. ($\times 10^{19}$ cm^{-3})		Mobility μ (cm^2/V s)	
		1.3 K	300 K	1.3 K	300 K	1.3 K	300 K
0.0085	45	2.46	2.87	1.37	1.70	153.8	103.4
0.018	35	1.90	2.29	2.20	2.09	146.2	130.3
0.029	50	0.89	1.20	7.31	6.94	97.1	73.2
0.04	50	1.01	1.17	6.86	7.05	90.3	74.4

Figure 2.8: Electrical properties of the $In_{1-x}Mn_xSb$ samples at 1.3 K and 300 K [101].

$In_{1-x}Mn_xSb$ films have also been grown by the horizontal Bridgman method with Mn concentration between 0.006 and 0.04 [10]. An increase in the anomalous Hall resistivity with Mn concentration below 30 K suggested a strong localization of carriers. The carrier concentration also increased with dopant concentration, implying Mn atoms substitute the In sites and create conduction holes. Similar to the case of $In_{1-x}Mn_xSb$ growth by

liquid phase epitaxy, a magnetic ordering below 10 K due to InMnSb alloy formation and other due to MnSb clusters have been observed. The presence of ferromagnetic clusters with higher T_C may make them important for device applications.

2.2.3 Study for achieving higher Curie temperature T_C

For these DMS to be useful in device applications, the Curie temperature T_C needs to exceed 300 K. Thus, the low T_C of the investigated DMS shows a serious problem in spintronics.

The first report of T_C in p-type (In,Mn)As was 7.5 K [71]. A relation between the ferromagnetic transition and carrier localization and a Zener double-exchange process were pointed out. As (Ga,Mn)As promises to give the highest T_C in the III-V based DMS, experiments in some of the ferromagnetic (Ga,Mn)As samples suggested ferromagnetic rise from the Zener double-exchange associated with electrons in the unfilled 3d shell. These samples have T_C close to 50 K [103]. Later, Ohno *et al.* [104] presented a jump of T_C as high as 110 K in a (Ga,Mn)As sample with Mn concentration x of 0.053. It was also found that the kinetic-exchange mechanism for ferromagnetic coupling influences on T_C value. The RKKY mechanism, which originally applied to indirect coupling between Mn d-shell moments mediated by induced spin polarization in a free-hole itinerant-carrier system, is proposed to dominate [105]. Recently, due to the development of post growth annealing techniques, T_C is pushed up to 173 K for 8% Mn doped GaAs [106]. Although the discovery made it possible to do proof-of-principle experiments for fabricating various spintronic devices, this T_C is still too low for real world application. In (III,Mn)Sb DMS system, due to weaker p-d exchange and smaller effective mass of holes in the larger unit cell antimonide, (III,Mn)Sb is predicted to have smaller T_C than that of (Ga,Mn)As [107; 108]. The kinetic-exchange mechanism also has influence on T_C values [109]. However, (III,Mn)N and (III,Mn)P bring higher T_C, even far above 300 K, particularly in (Ga,Mn)N [108]. Sasaki *et al.* [110] reported a very high T_C of 1000 K in (Ga,Mn)N samples. However, it was not completely understood that this high T_C is attributed to a (Ga,Mn)N ternary alloy only or to other ferromagnetic metal contributed in the host GaN lattice. The unclear nature of magnetic interactions in these wide-gap DMS attracts various interests [111; 112; 113; 114; 115; 116; 117].

Efforts to obtain ferromagnetic DMS with T_C higher than 300 K is not only a challenging task for experiments but also for theory, where the underlying mechanism of their ferromagnetic properties has not been completely understood. However, it is widely demonstrated that the dominating exchange mechanism (i.e. Zeners's p-d-exchange and Zener's double exchange) leads to ferromagnetic order [119; 120]. Bergqvist *et al.* [118] calculated T_C of $Ga_{1-x}Mn_xAs$ as a function of Mn concentration x using the mean field approximation (MFA-VCA) and Monte Carlo simulations (MC) (Fig. 2.9). The percolation and disorder effects are considered to play a critical role for ferromagnetism in this system. The calculated T_C values from MC simulations (by accounting for percolation problems) are lower than these from MFA-VCA. One can be understood that percolation seems to show an obstacle for high T_C in DMS. Jungwirth *et al.* [107] also

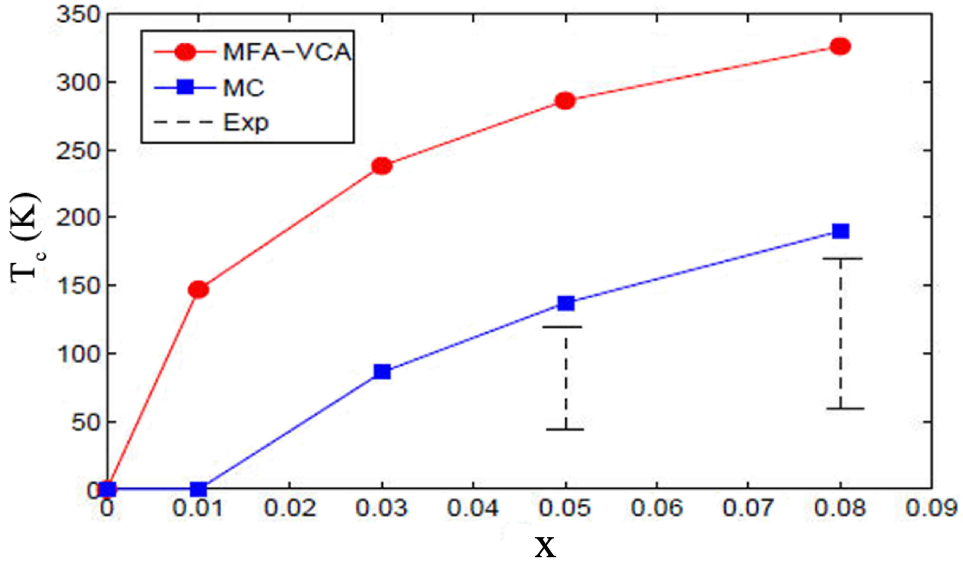

Figure 2.9: Calculated Curie temperatures of $Ga_{1-x}Mn_xAs$ as a function of Mn concentration x using the mean field approximation (MFA-VCA) and Monte Carlo simulations (MC) in comparison with experimental data [118].

presented mean-field theory for the estimation of T_C in (III,Mn)V DMS, but accounted for Coulomb interactions among holes in the valence band, (which enhances T_C), and for correlations in Mn ion orientations (which reduce T_C) [121; 122; 123]. Transition temperatures for several III-V hosts doped with 5% of Mn and with itinerant hole densities $p = 0.1$ and $p = 0.5$ nm^{-3} are listed in Fig. 2.10. Recently, G. Bouzerar *et al.* [124] used a semi-analytic theory, in which T_C could be calculated as follows

$$k_B T_C = \frac{2}{3N_0} \sum 1/F_i \tag{2.4}$$

where N_0 is a total of classical spins, F_i is dependent of the Green's functions for spins on impurity sites i and j.

Predicted T_C for (Ga,Mn)N and (Ga,Mn)As are shown in Fig. 2.11. A surprise that T_C of the doped GaN is always lower and falls of more rapidly than for the same concentration of doped GaAs, in contrast to the results indicated above [110; 108]. Thus, the author concluded that even if strongly p-type samples of (Ga,Mn)N are prepared, 300 K ferromagnetism is highly unlikely. These results call for explicit experimental verification and also show the oversimplification of previous theories. From above reviews, it should be suggested that a room-temperature T_C in (III,Mn)V DMS requires a explicit experimental verification as well as improving theories.

Host	p (nm^{-3})	T_c^{MF}	T_c^{ex}	T_c^{coll}	T_c^{est} (K)
AlAs	0.1	45	53	41	47
	0.5	134	158	105	119
GaAs	0.1	40	43	38	41
	0.5	124	138	106	115
InAs	0.1	14	15	14	15
	0.5	41	44	40	41
AlSb	0.1	19	22	18	20
	0.5	58	64	49	53
GaSb	0.1	18	19	18	19
	0.5	85	88	82	85
InSb	0.1	11	12	11	11
	0.5	37	38	35	36
AlP	0.1	94	127	73	94
	0.5	173	218	105	121
GaP	0.1	57	70	50	60
	0.5	101	115	43	45
InP	0.1	66	80	60	70
	0.5	136	163	103	118
GaN	0.1	379	629	81	250
	0.5	656	907	270	387
InN	0.1	308	549	89	240
	0.5	531	777	303	423

Figure 2.10: Mean-field (T_C^{MF}), exchange-enhanced (T_C^{ex}), collective (T_C^{coll}), and estimated (T_C^{est}) ferromagnetic transition temperatures in III-V host semiconductors doped with 5% of Mn and with itinerant hole densities p=0.1 and p=0.5 nm^{-3} [107].

2.3 Summary

This chapter is a review of fundamental characteristics and growth of narrow band gap semiconductor InSb and (III,Mn)V DMS, with the main emphasis on (In,Mn)Sb. InSb with a very narrow band gap of 0.17 eV, and a high room-temperature electron mobility

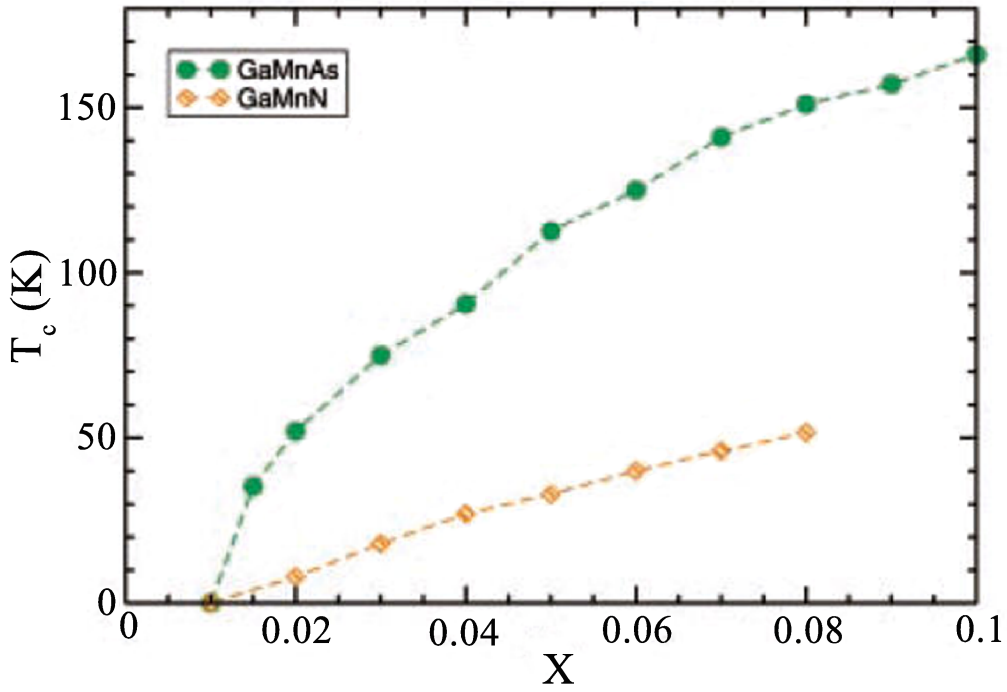

Figure 2.11: Predicted T_C for (Ga,Mn)N compared to (Ga,Mn)As with different Mn concentration x [124].

of 70000 cm^2/Vs provides many applications such as infrared detectors, Hall devices, as well as fast transistors. In such semiconductor devices, the spin-dependent phenomena is not available (or show only negligible effects) because the structures are made of nonmagnetic semiconductors alone. On the other hand, DMS based on non-magnetic semiconductors can be incorporated into semiconductor compounds based epitaxial structures and enhance spin-dependent phenomena due to the coexistence of the magnetism and semiconductor properties. DMS are obtained by alloying non-magnetic semiconductors with a sizable amount (a few percents, or more) of magnetic elements, such as Mn. We have focused on (III,Mn)V DMS. These materials have randomly located Mn local moments. They interact with itinerant carriers through exchange interactions in the valence band. The DMS and their heterostructures have offered a wide variety of materials and structures, which are possible to apply to spin-utilizing devices. For these applications, Curie temperature T_C should be above 300 K. The investigations for improving T_C are still in progress.

3 Preparation of InSb/GaAs, InSb/Si, and (In,Mn)Sb/GaAs heterostructures by molecular beam epitaxy

In recent years, the III-V compound semiconductors InSb and diluted magnetic semiconductors (In,Mn)Sb can be enabled by epitaxial methods such as metal-organic chemical vapor deposition (MOCVD), liquid phase epitaxy (LPE), metal-organic vapor phase epitaxy (MOVPE), and molecular beam epitaxy (MBE). It is shown that the growth mechanism is quite complicated. The substrate orientation, mismatch, surface preparation, growth temperature, growth rate, group V flux, thickness and more other factors of growth interruptions (such as time, temperature, doping) strongly effect on the finally film quality.

In this chapter, I present the preparation and growth of InSb and (In,Mn)Sb structures. The relevant processes are also discussed in detail. In section 3.1, a description of our growth system, a Riber Compact 21T MBE, is presented. Section 3.2 is followed with the methods to prepare GaAs and Si substrates. Section 3.3 focuses on the substrate temperature measurement and control. The information about growth rate calibrations is provided in section 3.4. In addition, the growth conditions are discussed in particular in section 3.5.

3.1 Riber Compact 21T molecular beam epitaxy system

MBE refers to the fluxes of constituent matrix and doping species (molecular beams) and their reaction on the substrate in order to form an ordered overlayer (epitaxy). Variations of MBE involve metal-organic MBE, solid-source MBE, hydride-source MBE, and gas-source MBE. Compared to other techniques of epitaxial film growth such as LPE, MOCVD, MOVPE, and related techniques, this epitaxy provides key advantages including the ability to control the growth to atomic monolayer dimensions and to monitor the growth process in real time. Due to the ultra-high vacuum growth environment of MBE, it occurs far from thermodynamic equilibrium and is mainly governed by the kinetics of the surface process. By using some in-situ surface analysis techniques such as reflection high energy electron diffraction and X-ray photoelectron diffraction, it is possible to study the dynamics of the growth process itself and the formation of inter-

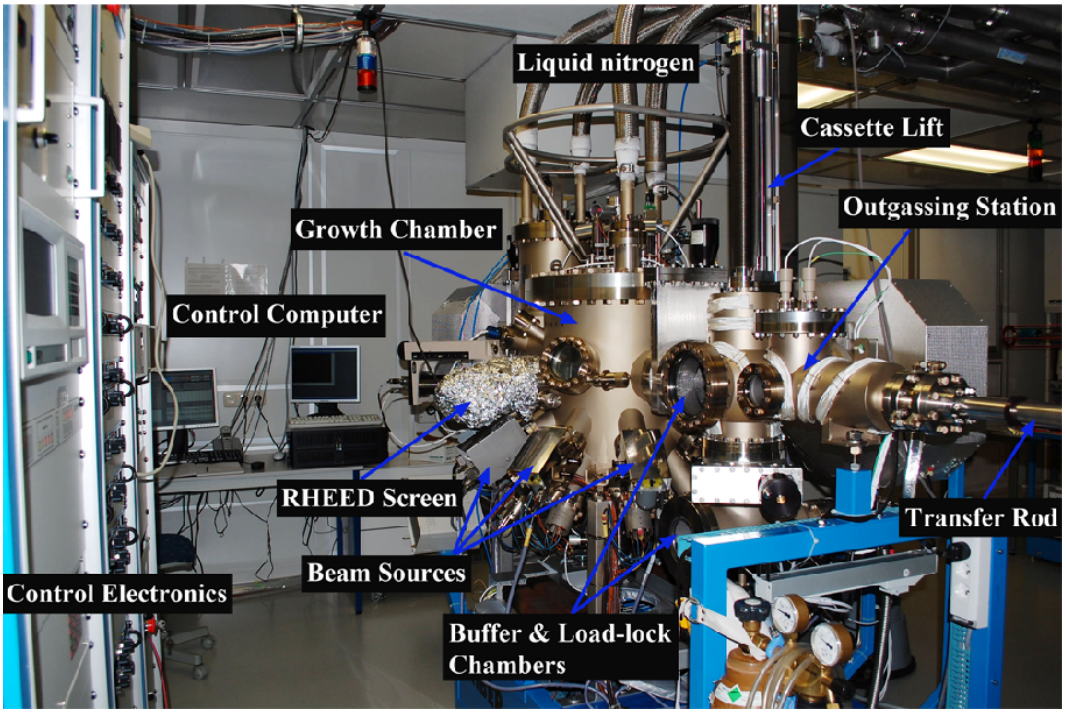

Figure 3.1: The Riber Compact 21T MBE system.

faces and surfaces of epilayers. The samples examined in my thesis were grown by MBE Riber Compact 21T as shown in Fig. 3.1. The MBE system consists three ultra-high vacuum (UHV) chambers: Load/unload chamber, buffer chamber, and growth chamber. Load/unload chamber is maintained under a vacuum condition in the 10^{-8} Torr range by the small turbo pump and membrane pump. After the cleaning, the substrates are placed on the substrate holders and installed on the loading cassette. In order to transfer substrates from the loading chamber to the buffer chamber, a cassette lift is employed, which is operated by a remote control. One substrate is then brought to the outgassing station by a manual transfer rod and heated for at least two hours at 200^{o}C. The vacuum in the buffer chamber in the range of 10^{-10} Torr is obtained by a ion pump. After the heating, the substrate is transferred by the manual transfer rod to the growth chamber. The substrate is then mounted on the substrate holder in the middle of the chamber and heated at high temperature to remove the oxide layer from the surface. The growth chamber is maintained under UHV conditions in the range of 10^{-9} Torr. A big turbo pump and an ion pump are employed to accomplish such pressure. In addition, a liquid nitrogen cooled circulation surrounds the entire inner surface of the growth chamber and the sources. This cryopanel causes a freezing out of remaining impurity particles in the growth chamber. Therefore, a further improvement of the vacuum conditions is accomplished. Growth chamber is equipped with beam sources including solid sources and gas sources. Solid sources contain effusion cells and cracking cells. Indium (In), Gallium

(Ga), Aluminum (Al) as group III-elements, Silicon (Si) as n dopant, and manganese (Mn) as p dopant and used for magnetic semiconductor materials are filled in the effusion cells. Antimony (Sb) as group V-element is filled in the cracking cell. Each cell have a thermocouple. By increasing the temperature, thermally induced atomic or molecular beams of the constituent elements are created. The incorporation of a specific element is controlled by simple mechanical shutter placed in front of the cells. Temperature and shutter of the cells are controlled by a computer. Apart from the solid sources, group V-elements: arsenic (As) and phosphor (P) are supplied from gases sources. A high temperature cell is used to crack both gases arsine (AsH_3) and phosphine (PH_3). The cracking temperatures for AsH_3 and PH_3 are usually 850^{o}C and 920^{o}C, respectively, resulting in the cracking efficiency higher than 90%. The group V flux is controlled by mass flow controller for the hydrides. Typical mass flow is around 1 sccm (which stands for standard cubic centimeters per minute), i.e. a mass flow equivalent to 1 cm^3/s at atmospheric pressure. The hydride mass flow can be abruptly turn on and off by valves. In addition, a shutter is placed in front of cracking cell to abruptly turn on and off the group V beam. The group V flux has to be larger than the group III flux in order to ensure that all group III atoms are used to form the III-V compound. An insufficient group V flux leads to a formation of group III metal droplets which degrades the sample surface. In addition, a motor rotates the substrate holder during the growth to obtain an homogenous surface.

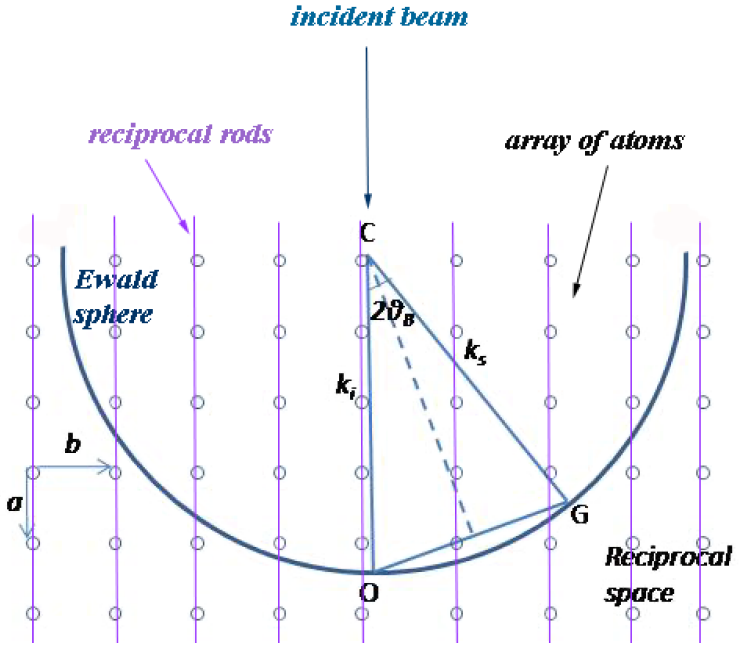

Figure 3.2: Reciprocal lattice and Ewald sphere construction illustrating refraction effects.

To in-situ monitor the growth, the reflection high energy electron diffraction (RHEED) is employed. RHEED is based on the reflection of electrons with high kinetic energy of

10 to 20 keV (12 keV in our setup) and low impact angle (typically less than 5^o) from the surface of a solid. The high-energy electron beams come from the RHEED gun and the diffracted beams are observed on a fluorescent screen forming the characteristic diffraction patterns. Due to the glancing incidence, the incoming electrons penetrate only the top layer of atoms of the sample. The de Broglie wavelength λ of these electrons with high kinetic energy E of 12keV is about 0.1 Å ($\lambda = hc/E$) corresponding to a Ewald sphere with radius k of 60 $Å^{-1}$ ($k = 2\pi/\lambda$). This radius is much bigger than the typical reciprocal lattice constant of III-V semiconductors. In Fig. 3.2, the surface of the sample is shown in reciprocal space. This reciprocal lattice builds a surface with a quadratic array of atoms. The incident plane wave falling on the crystal has a wave vector k_i whose length is $2\pi/\lambda$. The diffracted plane wave has a wave vector k_s which lies on the surface of the Ewald sphere. In reciprocal space, the two-dimensional array of the surface atoms turns into vertical lines, the reciprocal rods. Wherever these rods cross the Ewald sphere, the condition for constructive interference of the elastically scattered electron beams from the surface is fulfilled and Bragg's Law is obeyed. Therefore, a diffracted beam will occur. These scattered electron beams hit a fluorescent RHEED screen in certain RHEED spots, lying on a semi-circle. However, due to the energy spread of the incident beam and the deviation of real crystal from the translation symmetry in the surface, both the reciprocal lattice rods and Ewald circle seem to be thicker. Hence, the diffracted pattern of a flat surface are usually streaky (Fig. 3.3a). If the sample surface is rough or consists some three dimensional morphologies, the incident beam loses its energy because of the electron transmission diffraction. Therefore the streaky diffraction pattern is replaced by spots as seen in Fig. 3.3b.

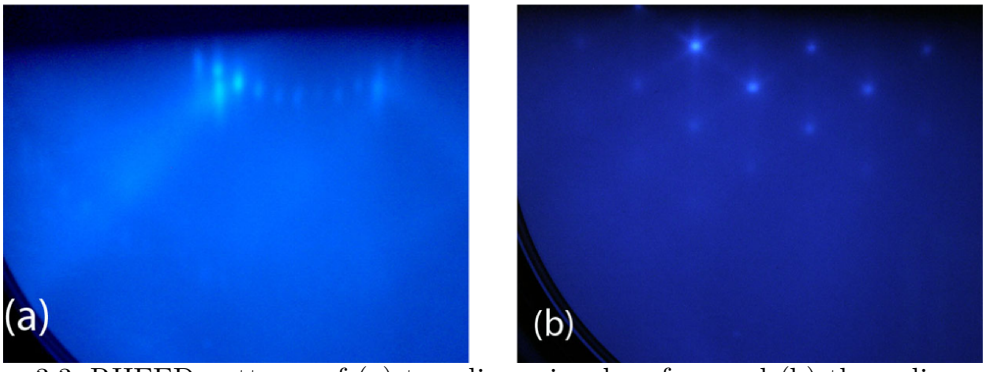

Figure 3.3: RHEED patterns of (a) two dimensional surface and (b) three dimensional surface, respectively.

Because of the phenomenon of surface reconstruction, (a re-ordering of the outermost atomic layers of a crystal to reduce the energy of the free surface), RHEED is one of the most helpful in-situ surface analysis techniques during MBE growth [125]. Each of the reconstructions, that a given surface can support during deposition, can only be maintained over a limited range of flux ratios and substrate temperatures at a given growth rate. Thus, surface reconstruction is extremely useful as a system-independent monitor of the MBE growth conditions. I used some applications of the RHEED such

as:

* Monitoring the temperature of oxide desorption from the substrate prior to growth. The RHEED pattern changes from bulk streaks or a diffuse glow to a sharply reconstructed surface when the surface oxides are desorbed from the substrate. For GaAs substrate, for instance, the oxide desorption temperature is well defined at 580^{o}C [126]. This issue will be presented in section 3.2.

* Setting up specific growth conditions, in particular with respect to clearly defined transitions in the surface reconstruction. For example, with a given beam equivalent pressure (BEP) ratio, the transition of surface reconstruction of GaAs is also defined [127]. In releasing the problems of substrate temperature measurement, this application of the RHEED is also useful. More detailed information will be provided in section 3.3

* Calibrating the growth rates and flux monitors by measuring the RHEED intensity oscillations. The maxima of intensity always corresponds to a smooth surface when a single monolayer is completely deposited. A high diffuse scatting with a reduction of the RHEED intensity means the deposition of the monolayer is not complete. For GaAs (001) substrate, the period of the RHEED intensity oscillation reveals exactly the growth of a single monolayer (equals half the lattice constant). This issue is presented in section 3.4.

* The quality of the deposited layer is also observed by the RHEED. While the streaky RHEED pattern refers to a flat surface, the spotty RHEED pattern corresponds to a rough surface or a surface with three dimensional islands. The involved results will be discussed in chapter 4 and 5.

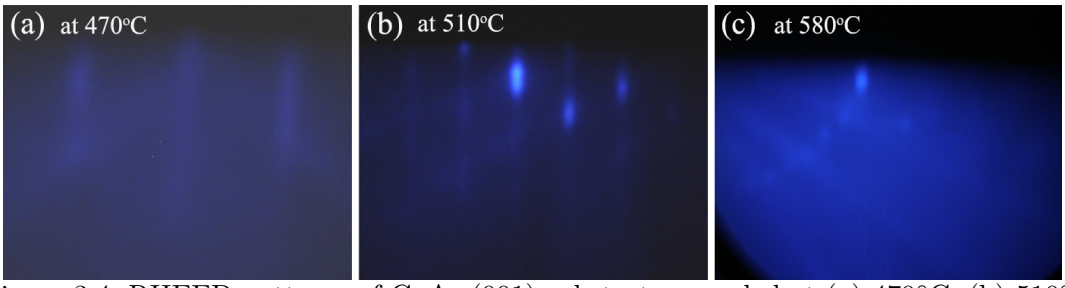

Figure 3.4: RHEED patterns of GaAs (001) substrate recorded at (a) 470°C, (b) 510°C and (c) 580°C, during the oxide desorption.

3.2 Substrates preparation

InSb has potential applications in high speed devices, infrared detectors and magnetic sensors. For these applications, InSb thin films should be grown on semi-insulating infrared transparent substrates. Although, there is a large lattice mismatch (14.6%) with InSb, GaAs is still an attractive substrate material due to its chemical stability and high resistivity. Besides, the replacement of native oxides with deposited oxides

Table 3.1: Wet cleaning conditions for Si wafer. HC, MC, NOL, and TVCO stand for hydrocarboneous contaminations, metallic contaminations, native oxide layer, and thin volatile chemical oxide, respectively.

Process condition	Temperature	Time	Results
C_2HCl_3 (trichlorethylene)	90^oC	5 min	Removal of HC
C_3H_6O (acetone)	20^oC	5 min	Removal of HC
CH_3OH (methanol)	20^oC	5 min	Removal of HC
NH_4OH, H_2O_2, H_2O	80^oC	10 min	Removal of Particles
HCl, H_2O_2, H_2O	80^oC	10 min	Removal of MC
HF (hydrofluoric acid 49%)	20^oC	2 min	Removal of NOL
HCl, H_2O_2, H_2O	80^oC	10 min	Growth of TVCO

in complementary metal-oxide semiconductor (CMOS) technology opens the door to replacing the Si with semiconductors without high-quality native oxides. It has been shown that the structure quality, orientation and morphology of epitaxial films depend strongly on the stoichiometry and reconstructions of the used substrates. Therefore, to achieve high quality reproducible epitaxial films, substrate surface preparation should be done with utmost care. In my work, I used GaAs (001) and vicinal Si (001) offcut by 4^o toward (110) substrates for the study. In the case of GaAs substrates, the substrates with 10^7 Ωcm resistivity at 22^oC protected by a grown oxide layer on the surface, are first etched using standard wafer cleaning procedures before being loaded in to the MBE system. The last step of cleaning procedures is baking substrates at 200^oC in outgassing station for at least two hours to desorb the water. Just before growth, the thin, protective oxide layer on the substrate surface was desorbed at 580°C under ultrahigh vacuum in growth chamber with antimony flux. The oxide desorption from the GaAs surface is monitored by the RHEED while heating substrate at a rate of 10^o/min. The RHEED evolution of the GaAs substrate is shown in Fig. 3.4. At 470°C, the RHEED pattern shows an unsharp elongated streaks due to the amorphous oxide layer as seen in Fig. 3.4a. A (2×1) reconstruction is obtained at 510°C (Fig. 3.4b) and a high intensity (2×4) reconstruction corresponding to the bulk GaAs reflections, appears immediately after the oxide layer is completely desorbed at 580°C (Fig. 3.4c).

In the case of Si substrates, hydrocarboneous molecules and native oxide layer in Si substrates are the major contaminants that need to be eliminated in order to get a clean surface [128; 129]. They affect subsequent epitaxial growth in two distinct ways: interference with the initial nucleation process and possible contamination of the epitaxial layers. The hydrocarboneous contaminations are often eliminated by degreasing of the surface with boiling trichlorethylene (C_2HCl_3) then rinse acetone, methanol, and deionized H_2O. The process to remove particle and metallic contaminations has been known as RCA process (first in solution of NH_4OH,H_2O_2, H_2O, then HCl, H_2O_2, H_2O).

The native oxide layer in Si substrates has a typical thickness of 1.5 nm. It is now well established that etching of the silicon surface in concentrated or dilute hydrofluoric

acid solutions can remove any oxide layer. The chemical reaction follows:

$$SiO_2 + 4HF = SiF_4 + 2H_2O \tag{3.1}$$

Finally, to protect the clean surface from any contamination and formation of non volatile SiO_2 due to expose to air while being transferred from wet chemical process to the MBE, a thin volatile oxide layer is grown. The different cleaning processes characterized are described in detail in Tab. 3.1.

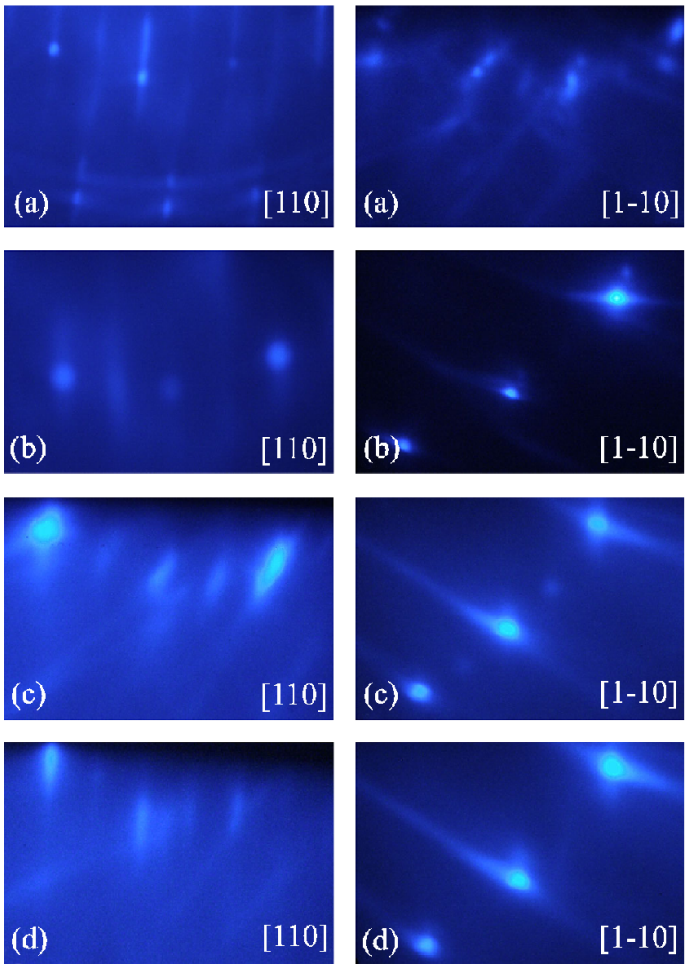

Figure 3.5: [110] and [1-10] RHEED patterns of Si (001) offcut by 4^o toward (110) substrate reconstruction recorded at (a) 380°C, (b) 430°C, (c) 850°C, and (d) 950°C.

After the chemical preparation of the substrate, the substrates are loaded immediately into the MBE system. Prior to the oxide removal, the substrate is heated to 200^oC for at least two hours, to desorb the water in outgassing station. This step is done to ensure the cleanliness of the growth chamber and to keep the contamination low. The substrate is then transferred to the growth chamber for next thermal treatments. SiO_2

thermal desorption takes place by heating Si substrate at $760^oC < T_S < 950^oC$ during tenths of minutes. A high temperature treatment ($\sim 950^oC$) of the Si substrates seems to be required to produce a certain terrace distribution in the Si surfaces in order to suppress antiphase domains during III-V epitaxial growth [130]. A detailed description of the thermal treatments and substrate reconstructions observed by RHEED are shown in Fig. 3.5. After the substrate temperature had been increased to about 850^oC, the surface showed a clear (2×4) reconstruction and appeared to be free of oxide as seen in Fig. 3.5c. When the substrate temperature reached 950^oC, a (2×1) reconstruction appears, indicating a dominance of double-height steps [128] (Fig. 3.5d).

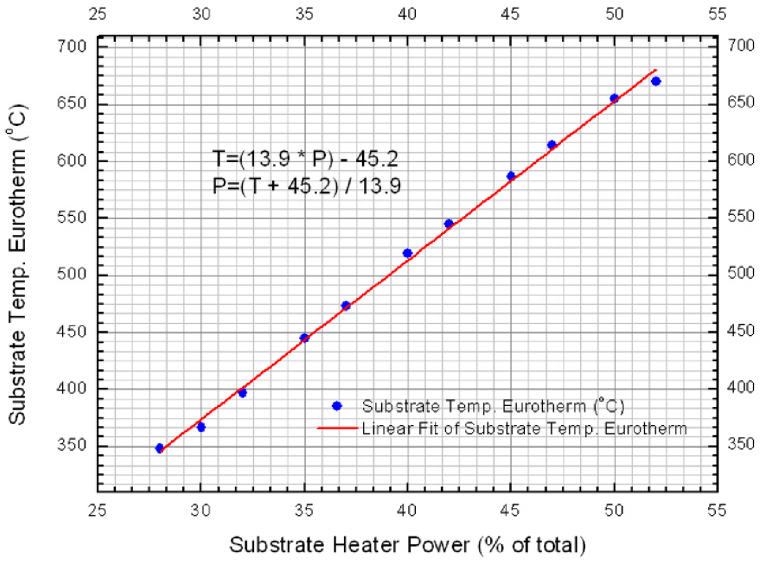

Figure 3.6: Correlation of eurotherm display and substrate heater power.

3.3 Substrate temperature measurement and control

One of the important features of the MBE growth technique is substrate temperature. It impacts on the incorporation of alloy semiconductors background impurities and lattice defects as well as interface roughness of heterojunction and surface morphology. In practice, the substrate temperature is strongly affected by various factors, including the backside finish of the substrate, the substrate holder, and the doping of the substrate. In the Riber Compact 21T MBE system, a backing plate with a thermocouple is mounted above the substrate holder in the vertical direction. By application of heating power, the temperature of the backing plate will be seen on the eurotherm control display. The temperature, therefore, is measured not directly at the the substrate but at the backing

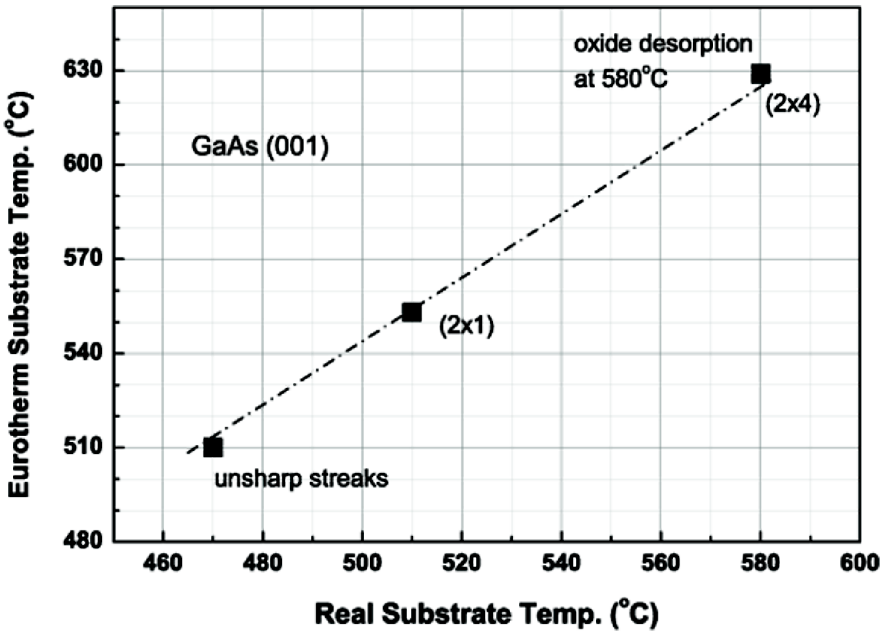

Figure 3.7: Correlation of eurotherm display and real substrate temperature via transition of GaAs surface reconstructions.

plate. It is usual, therefore, to move the backing plate as close as possible to the substrate before heating. It is common for the thermocouple temperature to differ by several tens of degrees from the actual substrate temperature when using such arrangements. Therefore, one has to distinguish between real substrate temperature and the temperature displayed in the MBE control panel. This would not be a problem if a correlation of eurotherm control display and the substrate heater power is used. By siting the same substrate heater power, the same substrate temperature condition is kept for everytime of the growth (Fig. 3.6). A substrate thermocouple can be calibrated against the melting points of certain eutectic affixed to, or deposited onto, the substrate. However, it is more common to reference temperatures to oxide desorption temperatures. For instance, the oxide desorption of GaAs substrate can be a well defined at 580^{o}C [126]. It is also possible to check substrate temperatures against changes in surface reconstruction. The RHEED can be employed to determine the real substrate temperature by observing the transition of surface reconstructions. Figure 3.7 shows the transitions of GaAs surface corresponding to eurotherm display and real substrate temperatures. I observed a transition between an unsharp elongated streaks (may be c(4×4) reconstruction [125]) to a (2×1) reconstruction 510°C. The (2×1) reconstruction was then replaced by a (2×4) reconstruction at 580°C, immediately after the oxide layer is completely desorbed (see Fig. 3.4 in section 3.2 for the obtained RHEED patterns). Repeated measurements of this phenomena generally show several fixed temperatures to find the desired real substrate temperature [131; 128; 132]. Other method to measure the substrate temperature is using infrared pyrometry [125]. It allows to measure the substrate temperature di-

rectly. It is also possible to calibrate source temperatures against a pyrometer. There are some cautions for using a pyrometer to measure substrate temperatures. A short wavelength pyrometer should be employed when using direct radiant heating. Because it avoids the transparency window of most commercially important semiconductors. For instance, a pyrometer operating at wavelengths below 0.95 μm is required for use with GaAs at growth temperature range of 450 - 750^{o}C. However, a long wavelength pyrometer may be used with In mounting systems, e.g., by measuring temperature of the In solder through the substrate. When using a short wavelength pyrometer, it is necessary to eliminate the reflections of hot filaments, evaporation sources and stray lighting from the substrate. It may be also necessary to compensate for fogging of the pyrometer port caused by deposition from background pressures of, for example, arsenic in III-V MBE, or from materials sublimating from the substrate. In our MBE system, the measured temperature from a short wavelength pyrometer is normal about 40^o lower than that from the eurotherm display.

3.4 Growth rate calibrations

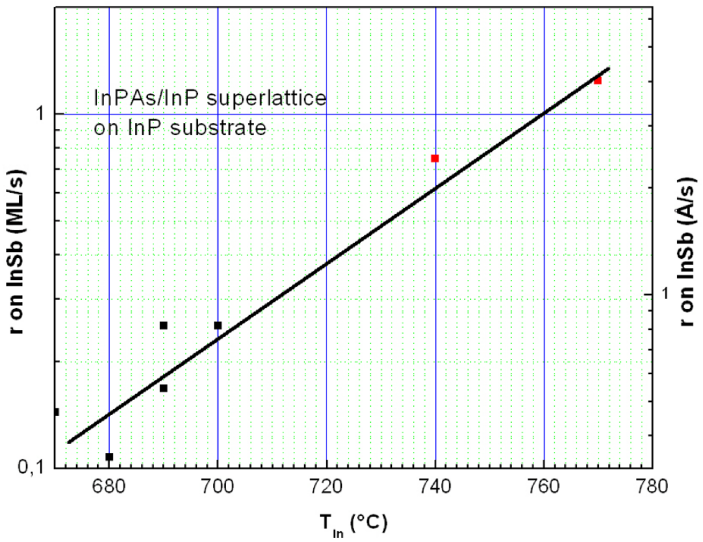

Figure 3.8: Growth rate of In archived from X-Ray measurements.

Other important feature of the MBE growth technique is the growth rate. The growth rate stands for amount of deposited material in term of layer thickness per unit time. Changes in the growth rate have a significant impact on the incorporation of alloy semiconductors, background impurities and lattice defects as well as interface roughness of heterojunctions and surface morphology. There are several methods to determine the growth rate such as using the RHEED intensity oscillation, X-ray or the measurements of

carrier concentration and thickness. The physical origin of the RHEED intensity oscillation lies in the fact that the maximal of intensity always occurs for smooth surface when a monolayer is completely deposited. Thus, the period of such oscillation corresponds exactly to the growth of single monolayer. In case the deposition is not totally finished, the surface is atomically rough, resulting a higher diffuse scattering and reduction of the RHEED intensity. In my work, to obtain the growth rate of In, InPAs/InP superlattices were grown on InP substrate at different temperature of In cell and analyzed by X-ray measurements. The obtained thickness of a period over the growth time show exactly the growth rate of In. The same method is used to calibrate the Ga and Al growth rate by growth GaAsP/GaAs superlattices and AlAsP/AlAs superlattices on GaAs substrate, respectively. In order to get the growth rate of Si dopant, doped bulk InSb is grown and the carrier concentration is measured by Hall measurement. For Mn, it is not possible to apply the similar method to Si, because the obtained hole concentration from Hall measurement is just approximately to the substitutional Mn density, but Mn can be at interstitial sites. Secondary ion mass spectrometry measurements or energy dispersive X-ray spectroscopy are much better to give the Mn concentration. Another ability I used to determine the Mn concentration corresponds to the Mn/In flux ratio, and confirmed by using a dynamical simulation of rocking curve analysis [133]. The experimental growth rate of each solid element In, Ga, Al and Si archived from X-Ray and Hall measurements for the studied samples is then plotted in Fig. 3.8, 3.9, 3.10, and 3.11, respectively. It is seen that the growth rate is followed a function of its effusion cell temperature, and is given by:

$$R(ML/s) = \exp(T - To)/s \tag{3.2}$$

where T_o and s are constants depending on the element and its physical state as well as the geometry of the cell.

3.5 Growth conditions of InSb/GaAs, InSb/Si and (In,Mn)Sb/GaAs

I carried out the growth of InSb/GaAs in a Riber Compact 21T MBE system equipped with RHEED. The semi-insulating (001) GaAs substrates with 10^7 Ωcm resistivity at 22^oC were first etched using standard wafer cleaning recipes before being loaded in to the MBE system. In the MBE system the indium beam is provided by conventional effusion cell and the Veeco valved antimony cell is cracked with temperature between 800^oC - 900^oC. Immediately prior to growth, the thin oxide layer on the substrate surface was desorbed at 580^oC under ultrahigh vacuum in growth chamber with antimony flux. Then the substrate temperature was decreased to the desired temperature for the growth of about 2 μm-thick InSb films. The samples were grown under the Sb/In flux ratio of about 5.6 and the growth rate of 2 Å/s but at various growth temperatures from 280^oC to 350^oC. A (2×4) reconstruction of RHEED pattern was observed during the growth

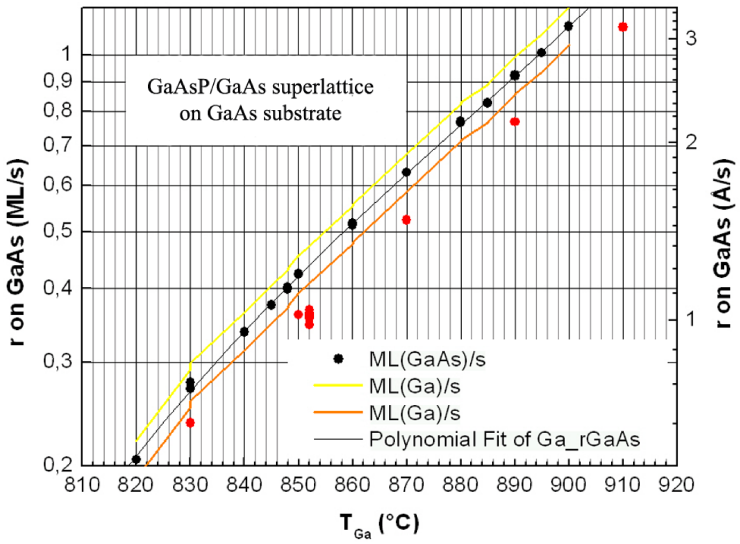

Figure 3.9: Growth rate of Ga archived from X-Ray measurements.

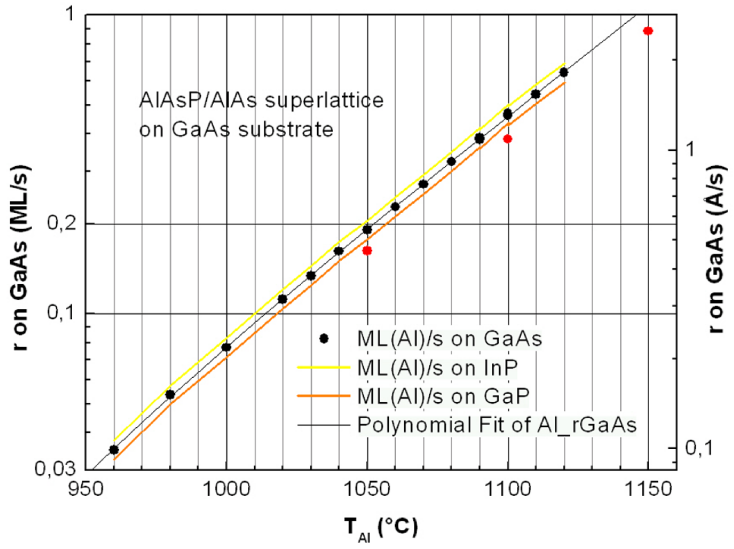

Figure 3.10: Growth rate of Al archived from X-Ray measurements.

of InSb films. After the growth the InSb films, the temperature was decreased to about 200^{o}C under the antimony flux.

I also investigated the growth of InSb on Si substrate. The Si substrate (p-type, with 50-80 Ωcm resistivity) 4° offcut (001) toward (110) were prepared using the Si wafer cleaning procedures (as given in section 3.2) before being loaded into the MBE system. The substrate temperature had been increased to $T_s = 950^o$C to obtain a surface characterized by double-height steps, which displayed by (2×1) of RHEED

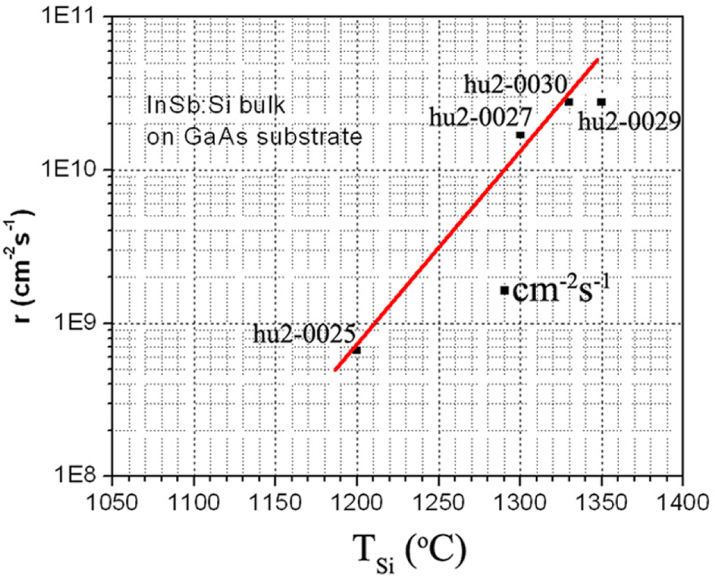

Figure 3.11: Growth rate of Si archived from Hall measurements.

pattern. After cooling the substrate to the intended growth temperature for InSb, the substrate exposed to Sb, resulting in a change in Si surface reconstruction from (2×1) to (1×1). The (1×1) reconstruction remains throughout the subsequent InSb deposition. InSb was deposited with Sb/In flux ratio of about 5.6 and growth rate of 2 Å/s. I have investigated growth temperatures between 280 and 400^{o}C. To prevent the formation of the defects we also used the insertion of various buffer layers between substrate and active InSb layer such as AlSb, GaAs and GaSb/AlSb superlattice to reduce the lattice mismatch. Structures grown on GaSb/AlSb superlattice show the best crystal quality. In these samples, after cooling the substrate temperature to the InSb growth temperature, a buffer layer consisting of 0.06 μm GaSb/AlSb superlattice was incorporated between substrate and 2 μm InSb layer. After the growth the InSb films, the temperature was decreased to about 200^{o}C under the antimony flux.

In order to observe magnetic cooperative phenomena in DMS system, one needs to introduce a sizable amount of magnetic elements. MBE could offer doping in excess of the thermodynamic solubility limit, segregation of impurities during growth. Typical MBE growth of (In,Mn)Sb films were carried out by using solid sources In, Sb, and Mn, without intentional doping. Mn provides both localized spins and holes because of its acceptor nature. Epitaxial (In, Mn)Sb films were grown on semi-insulating epiready (001) GaAs substrates using the optimum growth conditions as those for the best InSb/GaAs sample. Before initiating the Mn flux, 0.5 μm strain-relaxed thick InSb buffer layer was grown at temperature of 310^{o}C. A (2×4) reconstruction of RHEED pattern was observed during the growth of InSb film. The growth of 0.5 μm (In,Mn)Sb layer could be initiated by simply commencing the Mn flow during the InSb growth and keeping the substrate temperature T_s constant at 310^{o}C. No special precautions are necessary at the start

of (In, Mn)Sb growth. The RHEED of (In,Mn)Sb layers also shows the well-known (2×4) pattern. Samples were used in this study with the various Mn concentrations corresponding to the different temperatures of the Mn effusion cell from 420^{o}C to 670^{o}C. After the growth, the temperature was decreased to about 200^{o}C under the antimony flux. The Mn concentrations were estimated from the Mn/In flux ratio, and corrected by using a dynamical simulation of rocking curve analysis after the growth to be smaller than 1%. Both $\theta - 2\theta$ symmetric (004) and asymmetric (115) reflection rocking curves were used together with simulated curves to estimate the average Mn content in the samples. The experimental evidence of the process is given in chapter 5.

3.6 Summary

InSb/GaAs, InSb/Si and (In,Mn)Sb/GaAs systems were prepared by Riber Compact 21T MBE. For optimizing the growth, several parameters should be considered as follows: substrate cleaning, substrate temperature, beam equivalent pressure ratio, growth rate, V/III flux ratio, buffer layers. For my own samples, the Sb/In flux ratio of about 5.6 and the growth rate of 2 Å/s were chosen. In the case of growth on Si substrate, GaSb/AlSb superlattice as buffer layer should be introduced to prevent the formation of the defects. The growth of (In,Mn)Sb with different temperatures of the Mn effusion cell to get different Mn compositions.

4 InSb/GaAs and InSb/Si systems: measurements and properties

In this chapter, the properties of the investigated samples will be discussed. Results for both material system InSb/GaAs as well as InSb/Si will be presented in details. To analyze the samples, diverse techniques have been applied such as reflection high energy electron diffraction (RHEED), atomic force microscopy (AFM), scanning electron microscopy (SEM), and x-ray diffraction (XRD), Hall measurements, transmission spectroscopy, and noise spectroscopy. These methods used for characterization are also described in details. Section 4.1 will deal with the analysis of InSb/GaAs system, while section 4.2 is giving the results of InSb/Si heterostructures. Both systems will be compared.

4.1 InSb/GaAs system

The examined InSb/GaAs samples were grown under the growth conditions as presented in chapter 3, section 3.5 [1]. In addition, a schematic depiction of the structure is shown in Fig. 4.1.

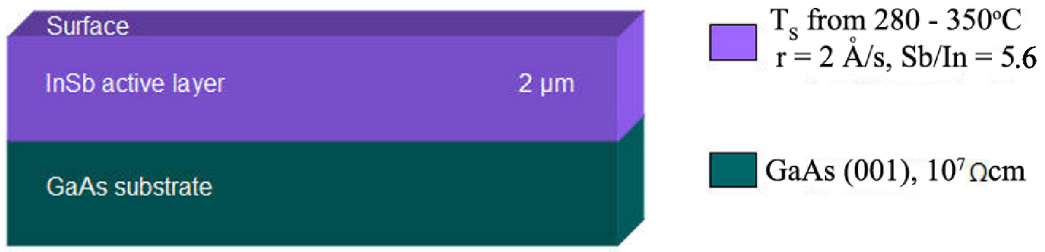

Figure 4.1: Schematic depiction of the structure InSb/GaAs.

[1] The temperatures are mentioned in this chapter as real substrate temperatures.

4.1.1 Surface structures

From RHEED

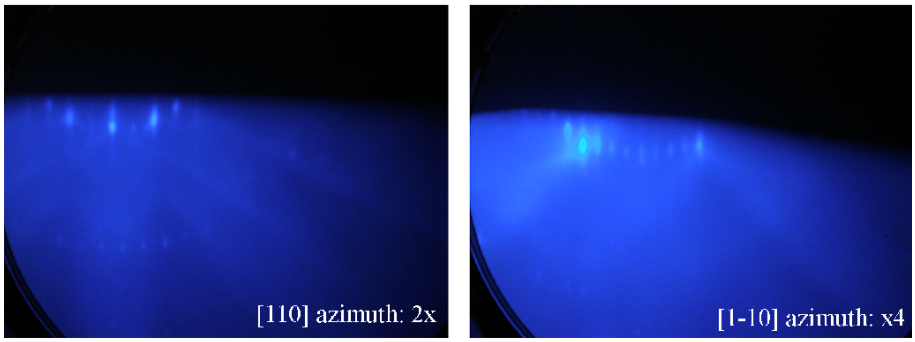

Figure 4.2: RHEED (2×4) reconstruction of InSb surface grown at 310^{o}C on GaAs (001).

As discussed in section 3.1, RHEED is one of the most important in-situ surface analysis method during MBE growth. When the first InSb monolayers have been deposited, the RHEED pattern had become spotty, indicating the three-dimensional growth because of the 14.6% lattice mismatch between InSb and GaAs substrate. After typically 100 Å, the spotty RHEED pattern was changed to streaky pattern for a smooth surface, indicating two-dimensional growth. The surface reconstruction was then (2×4) for the rest of the growth. Figure 4.2 displays the RHEED pattern with a streaky well-defined (2×4) reconstruction of InSb surface which observed throughout growth of InSb layer at 310^{o}C. The image on the left is obtained with the incident electron beam along the (110) direction, while the image on the right along (1-10). The sharp streaky RHEED pattern suggested a superior quality heteroepitaxial growth of InSb crystal. The RHEED patterns obtained from other InSb films, which were grown at temperature range from 280^{o}C to 350^{o}C, also showed similar (2×4) reconstruction and hence are not presented here. The surface of all samples was always mirror-like.

From atomic force microscopy (AFM)

Setups

Beside RHEED, atomic force microscopy (AFM) is extensively employed to study the surface morphology of the samples in atomic levels. The sample is mounted on a piezoelectric tube. This tube can move the sample in the z, x and y directions. The AFM works by scanning a fine semiconductor tip over a sample surface. The tip is positioned at the end of a cantilever. When the tip is nearly come to a sample surface, forces between the tip and the sample lead to a deflection of the cantilever. The magnitude of the deflection is captured by a laser that reflects at an oblique angle from the very end of the cantilever. A plot of the laser deflection versus tip position on the sample surface provides the resolution of the hills and valleys that constitute the topography of the surface. In most cases, it is necessary to adjust the distance between the tip and the

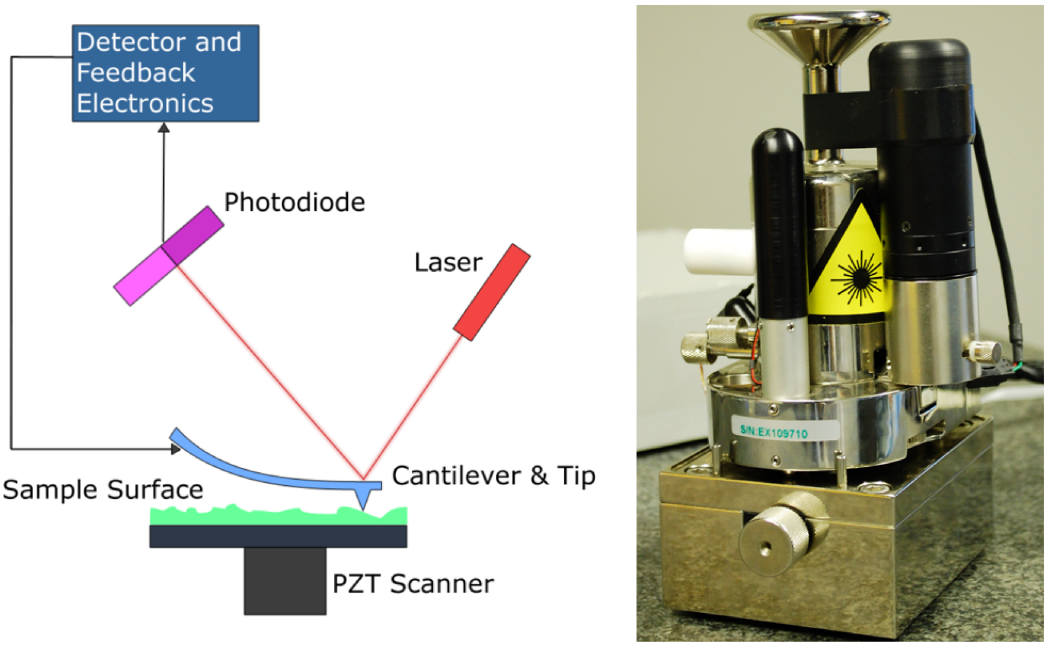

Figure 4.3: **left:** Schematic (reproduced from www.wikipedia.org) and **right:** Overview of our AFM.

scanned sample in the z direction. Because if the tip were scanned at a constant height, it would collide with the surface and may break. The sample surface is first scanned in the x direction. After a completely scanned line in the x direction, the scanner moves with a small step into the y direction to scan the next line. Figure 4.3 (left) illustrates the functional principle of an AFM, while figure 4.3 (right) is our AFM system

Results

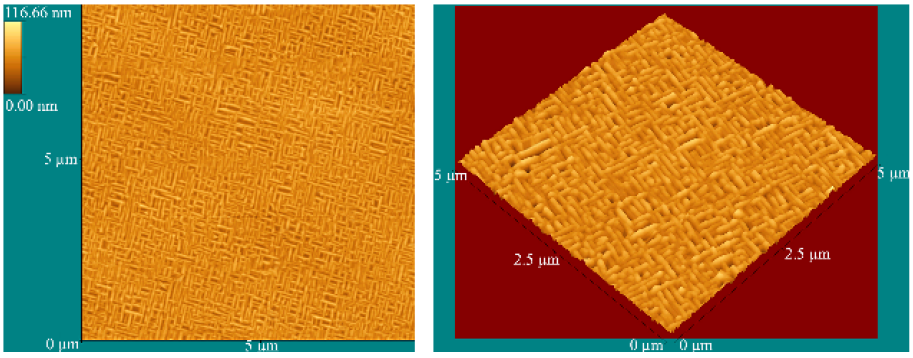

Figure 4.4: The AFM scans of the InSb film grown at 310°C on GaAs. **left:** 10 μm $\times$ 10 μm scan in 2D. **right:** 5 μm $\times$ 5 μm scan in 3D.

Figure 4.4 shows AFM topographs of the InSb film grown at 310^{o}C on GaAs. The surface of the grown InSb film has well-interconnected surface features. The average atomic height difference of the film deduced from the 3D image is about 100 nm, which is low enough for a flatness of the film. In an earlier work, Davis *et al.* [134] reported the growth of 2-5 μm-thick InSb on GaAs (100) substrate, also using the two step growth conditions (for more detail see chapter 3). The films revealed a set of rectangular features 5-10 μm on a side. However, we found no rectangular defect pattern on the grown surface. It was believed that with optimization of growth conditions, the defect density reduces in regions away from the InSb/GaAs heterointerface [135].

From scanning electron microscopy (SEM)

Setups

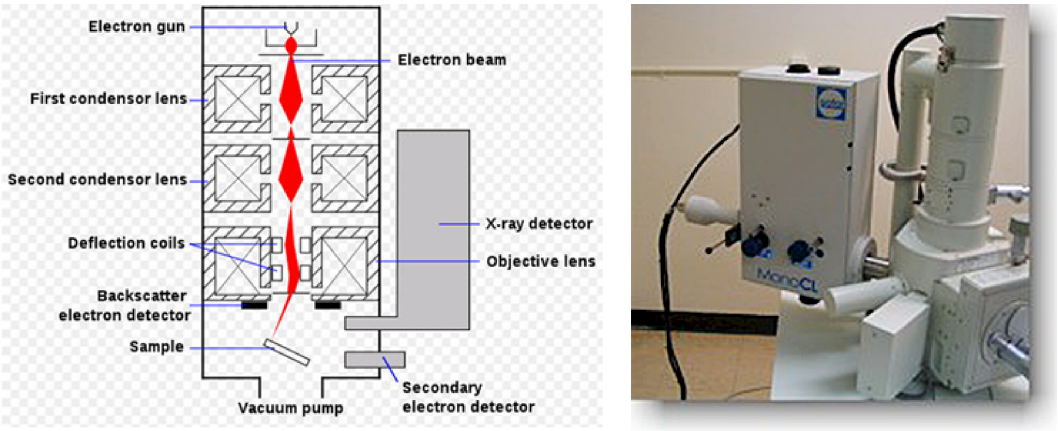

Figure 4.5: **left:** Schematic diagram of SEM (from www.wikipedia.org) and **right:** Our SEM Jeol JSM 6360 system.

The structural characterization is also studied using scanning electron microscope (SEM). A high-energy beam (about 2-50 keV) of electrons is used to scan the sample surface. The electrons will interact with the atoms. Due to the variation in the intensity of emitted electrons from the surface, the sample produces signals that contain information about the surface topography of the sample, composition and other properties such as electrical conductivity.

Figure 4.5 (left) shows a schematic diagram of SEM. In a typical SEM, an electron beam is emitted from an electron gun fitted with a filament cathode. It is focused by one or two condenser lenses to a spot about 0.4 nm to 5 nm in diameter. The beam then passes through deflector coils and interacts with the sample. Due to the energy exchange between the electron beam and the sample, three things can happen: reflection of high-energy electrons by elastic scattering, emission of secondary electrons by inelastic scattering, and the emission of electromagnetic radiation. Each of which can be detected by specialized detectors. Signals are displayed as variations in brightness on a cathode ray tube. The image can be digitally captured and displayed on a computer monitor

and saved to a hard disk. In my work, I used the SEM Jeol JSM 6360 (pictured in Fig. 4.5 (right)). It uses electron beam line Raith ELPHY PLUS (0.5 to 30 kV) to image a sample in vacuum with resolutions down to 3.0 nm at 25 kV. It can view specimens by secondary electron imaging (SEI), backscatter electron imaging (BSEI).

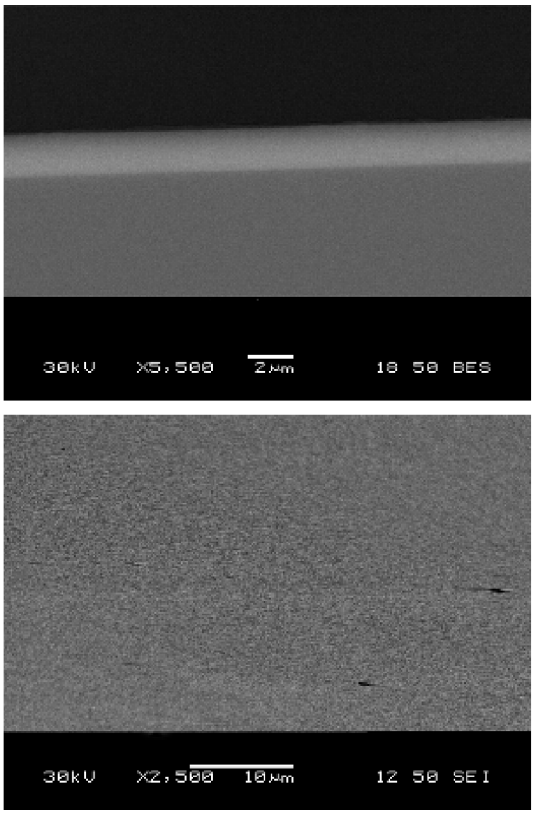

Figure 4.6: SEM micrographs of the sample grown at 310^{o}C. **top:** cross-sectional view and **bottom:** plan view.

Results

The cross section SEM micrograph of the film (cleaved sample) grown at 310^{o}C as seen in Fig. 4.6 (top) reveals the smooth surface and the sharpness of the interface between the InSb layer and the GaAs substrate. The film thickness is also detected to be $\sim$ 2 μm. However, the detailed scan on the surface (Fig. 4.6 bottom) shows the formation of small defects, of about 5 μm in length. It may be related to excess antimony [136] during cooling the growth temperature after the growth under the antimony flux.

4.1.2 Crystal diffraction

Setups

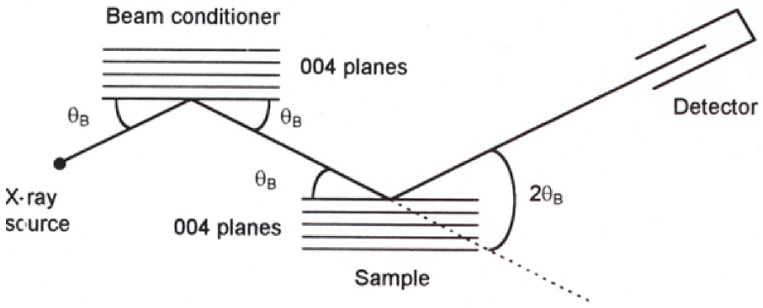

Figure 4.7: QC1a symmetric (004) reflection geometry. θ_B is the Bragg angle of the beam conditioner block and sample [137].

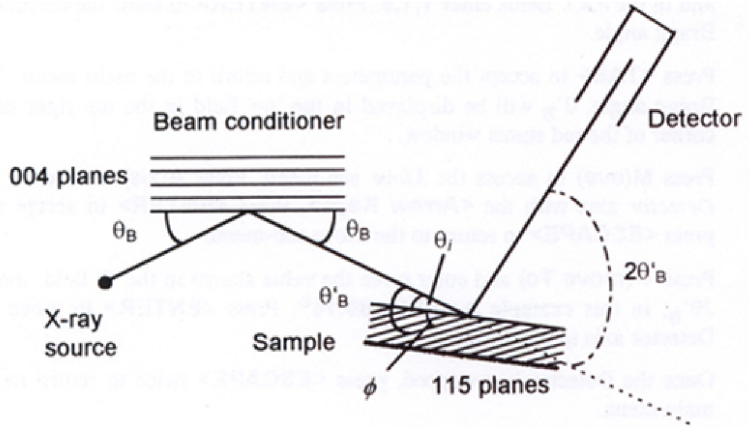

Figure 4.8: Asymmetric (115) reflection geometry. θ_B is the Bragg angle of the beam conditioner block, $\theta_B^{'}$ is the Bragg angle for the (115) reflection, ϕ is the angle between the (115) planes and the (004) planes and θ_i is the angle of incidence [137].

The crystal quality of the InSb films can be obtained from the x-ray diffraction (XRD) measurements. In my work, I used a Bede scientific QC1a diffractometer [137] to perform the measurements. This device uses double crystal XRD to remove the divergence characteristics of the x-ray beam from a compact 60 W air cooled x-ray source. Reference crystal GaAs is mounted in interchangeable, pre-aligned beam conditioner block. The close coupling of the reference crystal to the x-ray source and the short beam path within the instrument lead to surprisingly high peak count rates of more than 40000 cps for a quarter of the full power setting of the tube. Samples to be analyzed are mounted horizontally, with no adhesives, on detachable sample cassettes. A full 150 mm of X and Y travel for area mapping, as well as 32^o of tilt, 10 mm of hight adjustment and 360^o of rotation are built in to the QC1a. Data is collected by scanning both the sample and detector in the 1:2 ratio (θ-2θ)). Figure 4.7 and 4.8 show the experimental geometry on the QC1a required for both a symmetric (004) and an asymmetric (115) reflection,

respectively.

Results

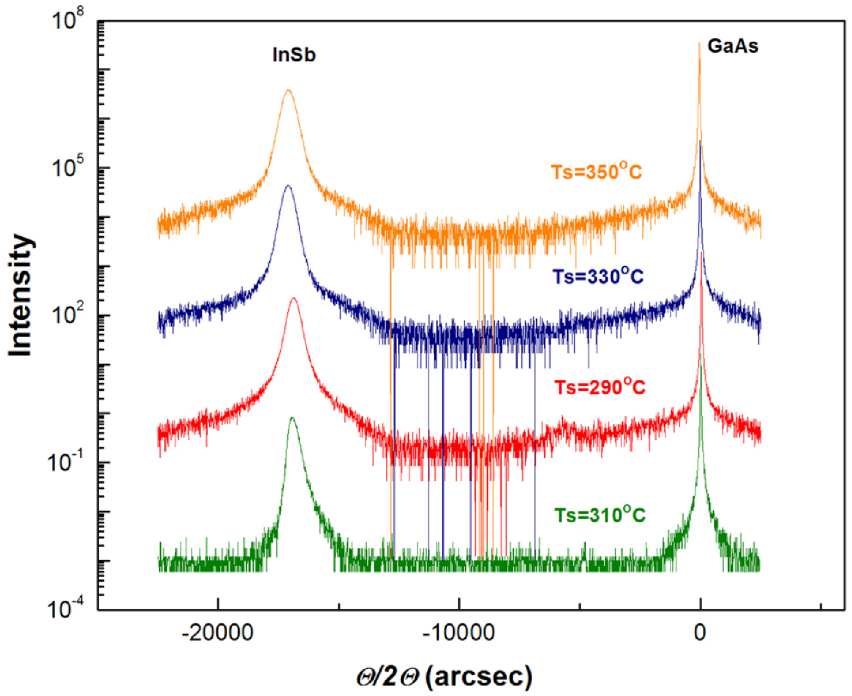

Figure 4.9: θ-2θ scans of InSb/GaAs films at 350^{o}C, 330^{o}C, 290^{o}C, and 310^{o}C.

The (004) double-crystal x-ray (DCXR) patterns of InSb/GaAs films grown at various growth temperatures are shown in Fig. 4.9. In all patterns, only peaks due to InSb and GaAs were observed. But the InSb peak is much wider than the GaAs peak, considering that the InSb layer is less consistent than the substrate. The InSb films were strongly oriented in (001) direction on the substrate and the InSb (004) peaks appeared with strong intensity. The intensity increased as the growth temperature decreased until 310^{o}C. But it decreased with the decrease in the growth temperature below 310^{o}C. For the sample grown at 310^{o}C, the InSb (004) peak exhibits the highest intensity and the full width at half maximum (FWHM) reduced to about 380 arcsecs compared to 439, 494, and 549 arcsecs at 290^{o}C, 330^{o}C, 350^{o}C, respectively. These DCXR results imply that the substrate temperature around 310^{o}C is suitable to grow InSb/GaAs with good crystal quality.

In addition, the strain were deduced to be smaller than 0,05%, indicating the films all were near 100% relaxed. As discussed in section 2.1, this can be understood that when the film is thick enough, the strain energy builds up to a point where it becomes energetically favorable to form misfit dislocations. At this point, the initially strained film would ideally decompose to a relaxed structure where the generated dislocations

relieve a portion of the misfit.

4.1.3 Electrical properties

In order to assess the transport properties, it is necessary to determine the resistivity ρ and carrier density n. The combination of ρ and n then allows to determine the mobility μ. In my thesis, I used van de Pauw (vdP) method to investigate direct current transport properties, in which only four sufficiently small contacts placed at the corner of square shaped sample are required [138].

Setups

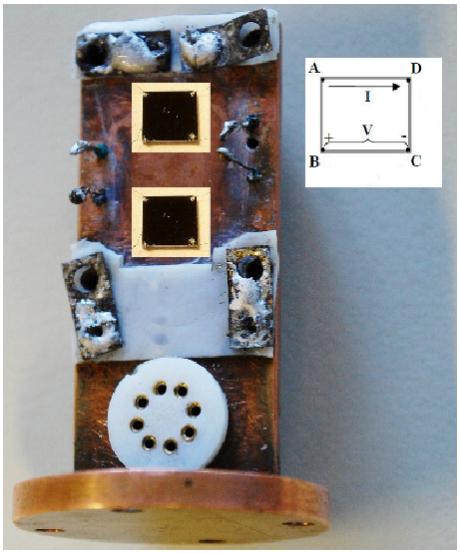

Figure 4.10: Two square shaped vdP samples mounted on the sample holder, corresponding to a schematic of simple square geometry with contacts A, B, C, D in the corners.

Indium contacts with small dimensions in comparison with the length of sample edge (4 mm) were made at corners of the sample by annealing at 200^{o}C for 2 minutes. The contact resistances were measured and found to be approximately the same. The contact size can influence on measured resistivity by correction factors, which originally calculated by van der Pauw [138]. 30-μm-Au wires were pressed in the contacts in order to connect the sample with a sample holder. The sample was then glued on the sample holder(there is a small isolated plastic tape between sample and sample holder) and wired. It is possible to mount two samples on the sample holder. The sample holder was contacted with soldering tin and wired (Fig. 4.10). Subsequently, it was placed on the sample holder mount, which is equipped with a heater and a thermocouple. A closed-cycle helium cryostat, which is placed in a water-cooled Helmholtz coil, is for cooling

down temperature. The voltage limit was set to 5 V, while 0.5 T for the magnetic field B and 9 - 300 K for the temperature range. The current was individually adjusted to the resistance for all samples. Before the measurement, the sample chamber was evacuated. Six cycles of measurements were taken for averaged results. The measurements are controlled using a LabView programme.

Definitions

The resistivity ρ is given by the ratio of electric field E and current density j and is the inverse of the conductivity σ

$$\rho = \frac{E}{j} = \frac{1}{\sigma} \tag{4.1}$$

and it corresponds to the relationship between carrier density and mobilities μ

$$\rho = \frac{1}{e(n\mu_n + p\mu_p)} \tag{4.2}$$

where n and p are electron and hole concentrations, respectively, while μ_n and μ_p are their respective mobilities. If the system has only electrons here, then the formula should be

$$\rho = \frac{1}{en\mu_n} \tag{4.3}$$

The Hall coefficient R_H is obtained from a combination of four-terminal resistances $R_{AC,BD}$ (the contact points A, B, C and D are marked in Fig. 4.10) measured once with and without magnetic field B

$$R_H = \frac{R_{AC,BD}(B) - R_{AC,BD}(B=0)}{B} \tag{4.4}$$

The carrier density n relates to the Hall coefficient R_H by

$$n = \frac{-1}{qR_H} \tag{4.5}$$

For two-layer system it should take the form

$$R_H = \frac{d(R_{Hb}\sigma_b^2 d_b + R_{Hs}\sigma_s^2 d_s)}{(\sigma_b d_b + \sigma_s d_s)^2} \tag{4.6}$$

where the subscripts b and s refer to the bulk and surface, respectively, σ is conductivity and $d = d_s + d_b$ is total thickness [139]. For a bulk semiconductor with simultaneous electron and hole conduction the Hall constant R_{Hb} and conductivity σ_b are given by

$$R_{Hb} = \frac{p\mu_h^2 - n\mu_e^2}{q(p\mu_h + n\mu_e)^2} \tag{4.7}$$

$$\sigma_b = \sigma_e + \sigma_h = q(n\mu_e + p\mu_h) \tag{4.8}$$

where *n(p)* is electron (hole) concentration, μ_e (μ_h) is electron (hole) mobility [11]. The temperature dependence of n and p are given by the equation

$$n = p = 4.28 \times 10^{15} T^{1.5} (m_e m_h / m^2)^{3/4} \exp(-E_g/2kT) \tag{4.9}$$

where m is the mass of the electron in free space, m_e (m_h) is the effective mass of the electron (hole) [140]. For InSb, m_e=0.014m and m_h=0.43m. The band gap, E_g, is taken to vary with the temperature according to

$$E_g = 0.24 - \frac{6 \times 10^{-4} T^2}{T + 500} \tag{4.10}$$

First, we assume that the surface layer consists of electrons and the surface layer is much thinner than the bulk layer. Therefore, the following identities are exposed

$$d = d_b, R_{Hs} = \frac{-1}{qn_s}, \sigma_s = qn_s\mu_s \tag{4.11}$$

$$d_s n_s = N_s \tag{4.12}$$

where μ_s (n_s) is electron mobility (concentration) of the surface layer, N_s is the sheet electron concentration. Second, N_s is assumed to be temperature independent and to have a value of 3.6e12 cm^{-2}. Third, we assume that

$$\frac{\mu_e}{\mu_h} = \frac{\mu_s}{\mu_h} = \frac{m_h}{m_e} = \frac{0.43}{0.014} = 30 \tag{4.13}$$

We can then write the Hall constant in the form

$$R_H = \frac{d}{q} \frac{d[p - n(\frac{\mu_e}{\mu_h})^2] - N_s(\frac{\mu_s}{\mu_h})^2}{\{d[p + n(\frac{\mu_e}{\mu_h})] + N_s(\frac{\mu_s}{\mu_h})\}^2} \tag{4.14}$$

$$R_H = -1.25 \times 10^{15} \frac{1798 \times 10^{-4} n + 32.4 \times 10^{14}}{(62 \times 10^{-4} n + 10.8 \times 10^{13})^2} \tag{4.15}$$

If we insert the form of n, we have the temperature dependence of the Hall constant, which will be discussed in the next section.

Results

Figure 4.11 shows the experimental carrier concentration as a function of measured temperature for InSb/GaAs samples grown at 290^{o}C, 310^{o}C, 330^{o}C and 350^{o}C. All samples are n type in the entire temperature range. The experimental results were then compared with the the calculation of the carrier concentration for the 2 μm-thick InSb films (the black curve), where m is the mass of the electron in free space, m_e (m_h) is the effective mass of the electron (hole) [140]. For InSb, m_e=0.014m and m_h=0.43m. The

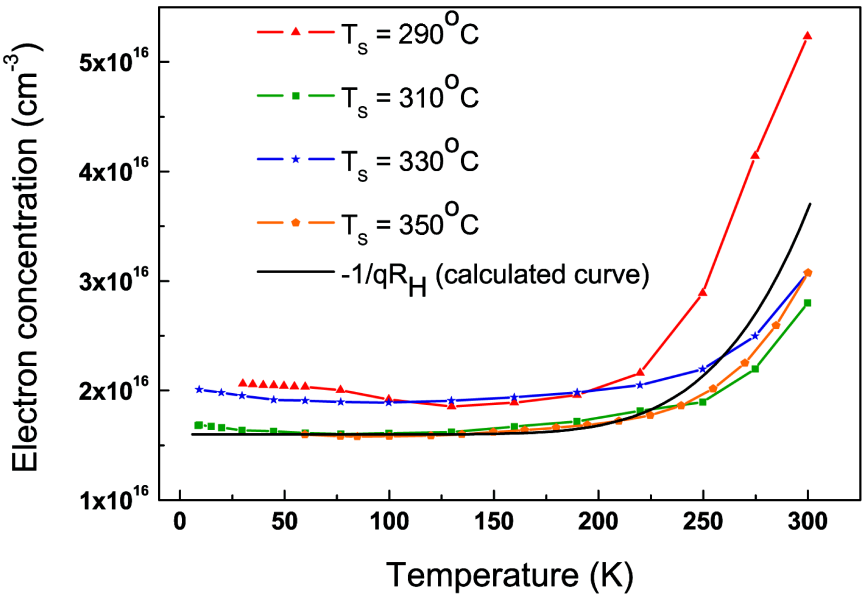

Figure 4.11: Temperature dependence of experimental carrier concentration in InSb/GaAs films grown at different temperatures. The theoretically black curve is inserted for comparison.

band gap, E_g, is taken to dependence of the temperature according to

$$E_g = 0.24 - \frac{6 \times 10^{-4} T^2}{T + 500} \tag{4.16}$$

It can be seen that the experimental curves fit quite well to the expression of the inverse Hall constant. Below 200^{o}C, the carriers concentration is quite constant indicating that there are no more intrinsic carriers. Hence these carriers are due to the ionized impurities (scatterers). Above 200^{o}C, the carrier concentration increases gradually. Because the electrons are much lighter than holes, there is a finite possibility that electrons can reach the conduction band and contribute to electrical conduction (n-type) in the Hall measurements and will give the sign of the Hall constant at ordinary temperatures. For the InSb layer grown at 310^{o}C, the electron concentration is lowest.

The temperature dependence of measured Hall mobility as shown in Fig. 4.12 is almost identical. The highest measured 300 K Hall mobility as 41100 cm^2/Vs is observed in the sample grown on GaAs at 310^{o}C. It is evident that the electron mobility decreased with measurement temperature in the samples. According to Matthiessen's rule, the electron mobility of InSb layer, μ, can be related to μ_b and μ_d, as follows

$$\frac{1}{\mu} = \frac{1}{\mu_b} + \frac{1}{\mu_d} \tag{4.17}$$

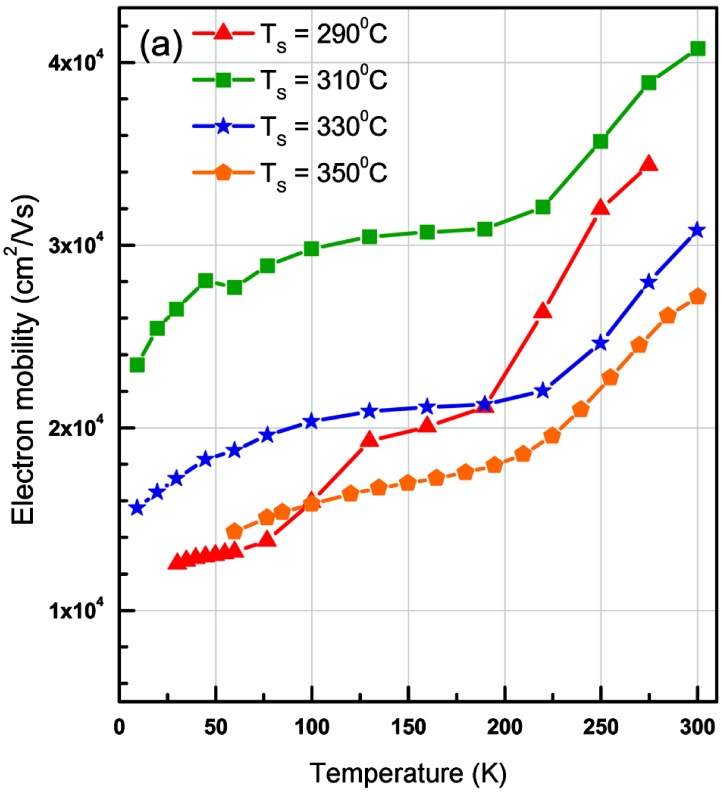

Figure 4.12: Temperature dependence of Hall mobility in InSb/GaAs films grown at different temperatures.

where μ_b is the intrinsic electron mobility of the bulk material and μ_d is the mobility limited by dislocation scattering. Electrons can be scattered by the depletion potential around the dislocations and the lattice dilatation associated with the dislocations. Using the Pödör and Dexter-Seitz models [141; 142], Weng *et al.* [143] found that the dominant factor limiting the electron mobility was the lattice dilatation scattering, which is apparently consistent with the predictions of the Dexter-Seitz model. According to this model, the mobility limited by deformation potential scattering μ_d is inversely proportional to the edge dislocation density D. These results, therefore, show a quantitative correlation between increasing dislocation density and decreasing electron mobility. The dislocation scattering increases as the temperature decreases since the screen effect of free carriers decreases. Therefore, the degradation of electron mobility is observed at low temperature. The electron mobility for the sample grown at 330^{o}C is 30800 cm^2/Vs and 19500 cm^2/Vs at 300 K and 77 K, respectively. However, for sample grown at 290^{o}C, the 300 K mobility was found higher but changed significantly when measurement temperature decreased. We obtained mobilities of 33000 and 13800 cm^2/Vs at 300 K and at 77 K (reduced 57% compared to 36 % for sample grown at 330^{o}C), indicating more defects formed due to unsuitable growth temperature. For the sample grown at 310^{o}C,

the 300 K electron mobility improved to 41100 cm^2/Vs, corresponding to 2.9e16 cm^{-3} of carrier concentration. The 29.6% reduction of electron mobility as the temperature decreased was smallest, suggesting the good quality of the film. This highest mobility in my sample is higher than the mobilities reported for 2 μm MBE InSb grown directly on GaAs samples done by other groups [26; 143].

The samples grown at 310^{o}C and 350^{o}C show the same carrier concentration at low temperatures (Fig. 4.11, the green and orange curve) - thus the same number of ionized impurities - but markedly different mobilities. Apparently this mobility difference can not be an effect of carrier concentration or ionized impurity concentration. Thus it is due to dislocation scattering with different dislocation density and not due to ionized impurity scattering. Generally, the mobility due to ionized impurity scattering scales with the concentration of ionized impurities. The low temperature ($<$ 150 K) carrier concentrations in my samples are ~1.6e16 cm^{-3} (310^{o}C, and 350^{o}C sample) and ~2e16 cm^{-3} (290^{o}C and 330^{o}C sample) which would correspond to a change of mobility due to ionized impurity scattering by maximum 25%. Clearly, the low temperature mobility (low temperature chosen to excludes the influence of intrinsic carriers on mobility) of the 310^{o}C-sample is larger by far above 25% compared to the mobilities of the 290^{o}C- and 330^{o}C- sample (the samples with the higher carrier concentration at low temperature). The higher mobility of the 310^{o}C-sample can thus not be explained by ionized impurity scattering only - there has to be clearly an increase of mobility due to reduced dislocation scattering.

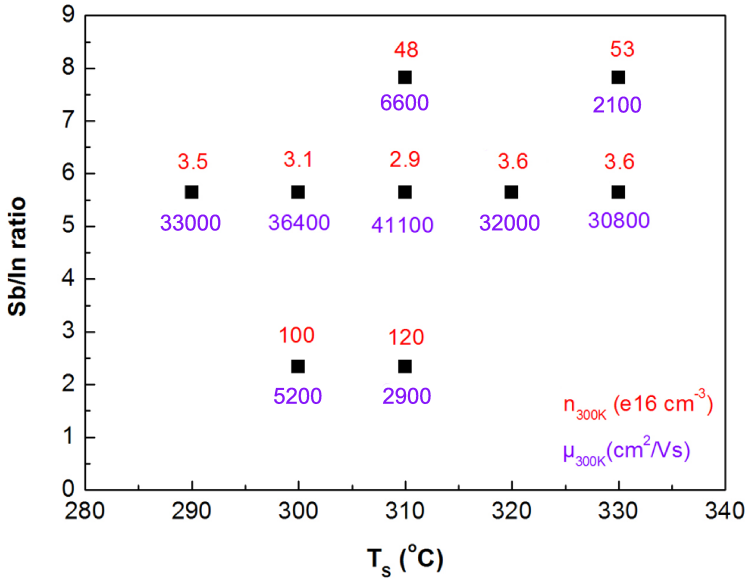

Figure 4.13: Measured 300 K electron concentrations and mobilities corresponding to the growth temperatures and Sb/In flux ratios.

4.1.4 Effects of growth temperature and Sb/In flux ratio on the electrical properties

It is well-known that substrate temperature and V/III ratio are two vital parameters in obtaining both good surface morphology and electronic mobility. I grew many samples at different temperatures and different Sb/In flux ratios for this study. Figure 4.13 presents the electron concentration and mobility at 300 K of nine samples with different growth temperature and different Sb/In flux ratio. The growth temperature and Sb/In flux ratio range vary from 280^{o}C to 350^{o}C and from 2 to 8, respectively. It can be seen that, small changes in growth temperature, 10^{o}C, produce large changes in electron mobility as well as electron concentration. The mobility is improved significantly when growth temperature increases up to 310^{o}C. The highest mobility is measured for the sample grown at 310^{o}C and a corresponding beam flux ratio Sb/In of 5.6. This sample also shows the lowest electron concentration of ~2.9e16 cm^{-3}. Over 310^{o}C, the mobility decreases from the maximum to 30800 (cm^2/Vs) in the sample grown at 330^{o}C. Samples grown with the lower or higher Sb/In flux ratio than 5.6 exhibit the significantly lower mobilities. As discussed in chapter 3, section 3.1 that the Sb flux has to be larger than the In flux in order to ensure that all In atoms are used to form the InSb compound. An insufficient Sb flux leads to a decrease of the electron mobility and a formation of In metal droplets which degrades the sample surface. However, it is shown that an excess Sb flux also decreases the electron mobility as well as deteriorates the epilayer surface, and even causes elemental Sb droplets ~ μm range in size on the surface and in the film [136]. Thus, my results show the optimum value of the V/III ratio of 5.6, which gives the best mobility at growth temperature of 310^{o}C.

4.1.5 Effects of doping and BL on the structural and electrical properties

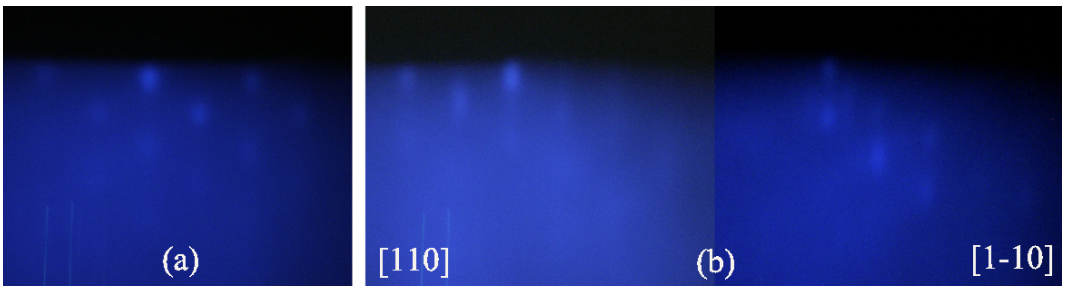

Figure 4.14: RHEED patterns recorded after: (a) opening the Al cell and (b) 0.1 μm InAlSb deposited

As discussed in section 4.1.3, at lower temperature electron concentration and mobility of the InSb epilayers correspond to degenerate, and the large lattice mismatch between the film and substrate results dislocations in the film. Thus, I investigated the Si-

doped InSb films with a doping level of 2e16 cm^{-3}, which should enable minimize the degradation of the electron concentration and mobility, and the interposed InAlSb buffer layers with a thickness of about 0.2 μm, which could reduce the mismatch and have shown promise for increasing the electron mobility of the InSb films [144; 145; 146].

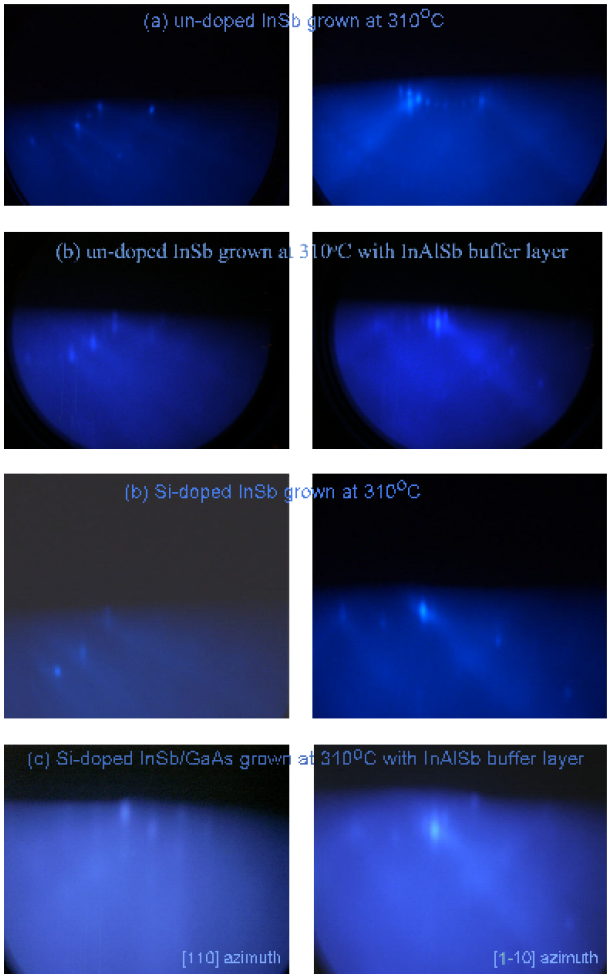

Figure 4.15: RHEED patterns of InSb surfaces grown on GaAs at 310^{o}C: (a) un-doped InSb, (b) un-doped InSb with InAlSb buffer layer, (c) Si-doped InSb, and (d) Si-doped InSb with InAlSb buffer layer

Figure 4.14 shows the RHEED patterns during the deposition of InAlSb buffer layer. As beginning of the Al cell opened, the RHEED pattern appears spotty (Fig 4.14(a)). By increasing the thickness of the deposited InAlSb layer, there is a clear trend from spotty to streaky (1×3) RHEED patterns (Fig 4.14(b)). The RHEED patterns of all four InSb films - grown at 310^{o}C; un-and doped Si, without-and with the InAlSb buffer layer - show (2×4) reconstructions as seen in Fig. 4.15. The sharp streaky RHEED pattern of the un-doped sample (Fig. 4.15(a) and (b))suggests a superior crystal quality

Table 4.1: X-ray and electrical data of different InSb films.

Sample	FWHM (arcsec)	μ_{300K} (cm^2/Vs)	n_{300K} (cm^{-3})	μ_{77K} (cm^2/Vs)	n_{77K} (cm^{-3})
Un-doped	380	41100	2.9e16	33400	1.6e16
Un-doped with BL	600	12400	2.0e17	11800	1.4e17
Si-doped	460	9100	1.7e18	9400	2.7e18
Si-doped with BL	880	4900	2.6e18	5300	2.6e18

of the epilayers. In the Si-doped sample, the obtained RHEED pattern is cloudy (Fig. 4.15((c)) and even more cloudy in the Si-doped sample with InAlSb buffer layer (Fig. 4.15(d)), indicating an inferior crystal quality.

The θ-2θ x-ray rocking curves of above samples are recorded and plotted in Fig. 4.16. In both un-doped and Si-doped samples, only the peaks due to GaAs substrate and InSb epilayer are clearly visible (Fig. 4.16(a) and (c). In the Si-doped sample grown with buffer layer, beside the peaks of GaAs and InSb, the right shoulder of the InSb peak is due to InAlSb buffer layer (Fig. 4.16(b) and (d)). The FWHM of InSb layers are about 380 arcsec, 600 arcsec, 460 arcsec and 880 arcsec for un-doped layer, un-doped layer grown with the buffer layer, Si-doped layer, and Si-doped layer grown with the buffer layer, respectively. Note that the InSb peak in Fig. 4.16(d) is wider than that in the other samples, suggesting a less consistent layer than the others.

Table 4.1 shows the variation of the InSb/GaAs material properties deduced from x-ray and Hall measurements. The un-doped layer exhibits the narrowest x-ray FWHM of 380 arcsec, with the highest 300 K mobility of 41100 (cm^2/Vs). As the temperature decreases, the mobility as well as the electron concentration correspond to degenerate. The reduction of electron mobility is about 29.6%. In the Si-doped samples, on the other hand, the mobility and the electron concentration increase slightly as decreasing temperature. However, it is evident that the electron mobilities of these samples are significantly lower than those of the un-doped film. The sample with $In_{0.95}Al_{0.05}Sb$ buffer layer shows even much lower electron mobility. This result is in contrast to previous work which describes InSb epilayers with InAlSb buffer layer. It was thought that the highly dislocated interface (due to the lattice mismatch) between epilayer and substrate would dominate the physical properties of the layer. To reduce the effects of this region, therefore, the method of growing various buffer layers is used. In our case, the quality of the InSb epilayers grown following this method did not exceed the expected results. To fully understand the system, I need to grow new structures with different doping level and different growth conditions of the InAlSb buffer layer. However, we have suspected that the quality of the InSb epilayers is improved rapidly with increasing layer thickness, regardless the presence of dislocations in the interface region. These dislocations then decrease in density with increasing distance from the substrate. Therefore, optimization the growth parameters is the primary concern for obtaining high quality of the epilayers (in agreement with Michel *et al* [147]).

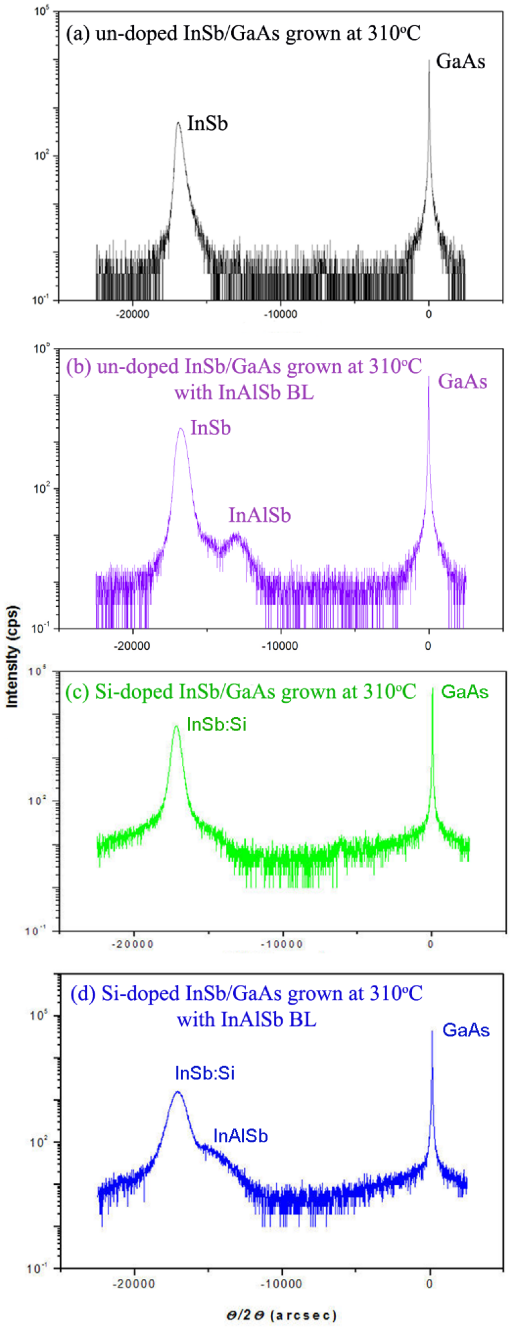

Figure 4.16: θ-2θ x-ray scans of InSb/GaAs films grown at 310^{o}C: (a) un-doped InSb, (b) un-doped InSb with InAlSb buffer layer, (c) Si-doped InSb, and (d) Si-doped InSb with InAlSb buffer layer

4.1.6 Infrared transmission

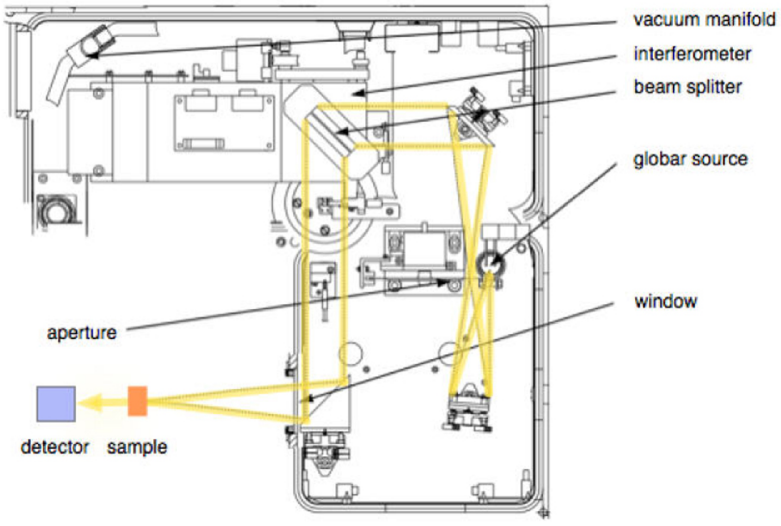

Figure 4.17: Schematic illustration of the Bruker IFS 66v spectrometer. The yellow line indicates the beam path.

In transmission spectroscopy, transmitted spectrum is created by illuminating a sample with light at a certain wavelength. The background is eliminated from the spectrum. Thus, it results in the fraction of light transmitted at each wavelength. In order to measure the spectrum, the most straightforward way is to pass the light through a monochromator. This monochromator allows only the light at a certain wavelength to pass through. The intensity of this single-wavelength light is then measured, directly indicating how much light is emitted at that wavelength. By changing the monochromator's wavelength setting, the entire spectrum can be measured. In this work, Fourier transform spectroscopy was employed to perform transmission measurements. Rather than allowing only one wavelength at a time to go through to the detector, this method lets through a beam containing many different wavelengths of light at the same time. Thus, the total beam intensity can be measured. Afterwards, the beam is modified to contain a different combination of wavelengths, giving a new data point. This process is repeated many times with different initial wavelength settings, modulated by a interferometer. All this data is collected and the transformation of the interferogram into spectrum is then carried out mathematically by a computer. Infrared transmission refers to energy in the region of the spectrum at wavelengths longer than those of visible light, but shorter than those of radio waves. Since InSb has a narrow band gap E_G, the spectrum is in the infrared region.

Setups

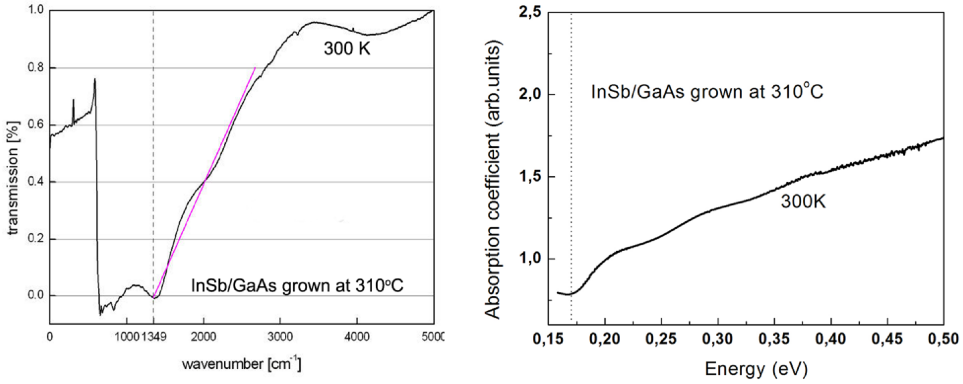

Figure 4.18: **left:** Infrared transmission spectra at 300 K of InSb/GaAs sample grown at 310^{o}C and **right:** An absorption vs energy plot

A Bruker IFS 66v spectrometer as illustrated in Fig. 4.17 was used to carry out the measurements. The spectrometer has a resolution of 0.1 cm^{-1} and a very wide spectral domain, between 25000 - 10 cm^{-1}, allowing measurements in both transmission, reflection and emission modes from the near to far infrared. The wavelength range covered extends from 1 μm to 40 μm [148]. The spectrometer comprises of globar and mercury vapor lamp as light sources, an interferometer chamber consisting of KBr beam splitter and the movable mirrors for continuous adjustments of the interferometer distance, followed by a sample chamber and two detectors. The detectors, a MCT-D316 and a KBr/DLaTGS D301, are connected to a computer. Thus, signal averaging, signal enhancement, base line correction and other spectral manipulations are possible with multitasking OPUS software. Spectra are then plotted on a HP plotter and data can be printed or saved on a 3.5" floppy. The measurements were performed at 300 K in vacuum.

Results

The infrared transmission spectra of the sample grown at 310^{o}C is shown in Fig. 4.18 (left). The cleaved samples have the same size of 2×5 mm. The spectra are analyzed according to [149], yielding a band gap of 1350 cm^{-1} for the sample, corresponding to 0.17 eV. This result fits well with the band gap of bulk InSb at 300 K. The absorption vs energy plots for these samples is shown in Fig. 4.18 (right). The onset of absorption coincides very well to the relation $\alpha \sim (E - h\nu)^{1/2}$, indicating a direct energy gap.

4.1.7 Noise

Theory

In both analog and digital electronics, the word noise means an unwanted perturbation to a wanted signal. Transport of electrons inside an electrical conductor will exhibit noise.

This occurs as some electrons will have a random motion, causing fluctuating voltage and currents. There are some subtypes of electronic noise such as thermal noise, flicker noise, generation-recombination noise (shot noise, burst noise, avalanche noise). Noise can be produced by several different factors. For instance, thermal noise (sometimes thermal, Johnson or Nyquist noise) is generated by the random thermal motion of charge carriers (usually electrons), inside an electrical conductor. It is unavoidable because it happens regardless of any applied voltage. Flicker noise (also known as pink noise *1/f*) is a signal or process with a frequency spectrum that falls off steadily into the higher frequencies. It occurs in almost all electronic devices at low frequencies, and results from a variety of effects, though always related to a direct current. However, it is not always possible to identify the respective effect of every subtype of noise. For example, there exists substantial suspicion that causes for flicker and generation-recombination noise overlap. A direct proof however is complicated. The noise level determines the signal to noise ratio of an electronic device. Thus, it can be determined how small the device can be or how low the smallest possible operating voltage is. Theoretically, the noise spectra S_V are composed of thermal noise $S_{V,th}$, flicker noise $S_{V,fl}$, and generation-recombination noise $S_{V,gr}$ according to

$$\begin{aligned} S_V &= S_{V,th} + S_{V,fl} + S_{V,gr} \\ &= \frac{A}{f} + \sum_i B_i \frac{1}{1 + (2\pi f \tau_i)^2} + 4\, k_B\, T\, R \end{aligned} \tag{4.18}$$

where A is the amplitude of the flicker noise, f is the frequency, B is the amplitude of the g-r noise, τ is the time constant for the g-r processes, k_B is the Boltzmann constant, T is the temperature, and R is the resistance. For transistors and sensors, both good transport and reduction of noise level are desired. Since the low noise spectrum is dominated by flicker noise in semiconducting materials, the Hooge constant α_H [150] is an important parameter. It relates to the quality of the sample and defines the level of the low frequency noise. One can propose the Hooge constant α_H from [151]

$$S_{V,fl} = \frac{A}{f} = \alpha_H \frac{V^2}{N f} \tag{4.19}$$

where V is squared bias voltage, N is the number of charge carriers. The Hooge constant α_H depends on the scattering mechanisms that determine the mobility [152; 153; 154; 155]. For InSb epilayers, the Hooge factors are found in the range of 10^{-2} - 10^{-3} [156; 157].

Setups

For this study, Dobbert *at al.* [33] performed the flicker noise measurements on my samples in a Greek cross geometry as shown in Fig. 4.19. The Greek cross structure has a length of 55 μm and a width of 17 μm. It was fabricated using standard optical photolithography and wet chemical etching. Ohmic contacts were made by alloying evaporated Au/Ge/Ni metal films. A SR560 differential low-noise preamplifier and a

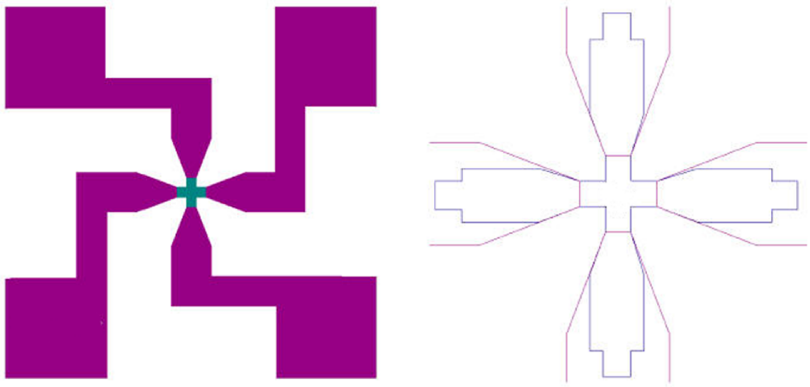

Figure 4.19: A Greek cross structure with base length of 55 μm and width of 17 μm. **left:** entire structure, **right:** detail of active structure.

Table 4.2: The mobilities μ and Hooge constants α_H for different InSb based samples at 300 K and 80 K [33].

Sample	μ_{300K} (cm^2/Vs)	α_{H300K} $(\times 10^{-5})$	μ_{80K} (cm^2/Vs)	α_{H80K} $(\times 10^{-5})$
grown at 310^{o}C	41100	4.4-29	33400	1.7-4.3
grown at 320^{o}C	30300	6.4-49	22300	3.9-99
Single crystal pure InSb	77000	20 - 800	67000	3.0

SR785 noise spectrum analyzer were used to measure the transverse noise between the Hall terminals. The frequency range for the measurements was from 3 Hz to 10 kHz. The samples were biased using constant currents of 10 - 900 μA, corresponding to voltages across the length of the sample from 10 to 4 V at 82 K and 3 to 30 mV at 300 K. The temperature range was from 300 K down to 82 K by using a nitrogen refrigerator.

Results

Two samples grown at 310^{o}C and 320^{o}C were examined for noise properties. The measured temperature range was from 300 to 82 K. From the measured noise spectra and the fitting in which all components have to be taken according to Eq. 4.18, one can extract the Hooge constant α_H for the samples. The Hooge constants α_H as well as the mobilities at 300 and 80 K are collected in Tab. 4.2.

At 300 K, the constant α_H are 4.4 - 29e-5 and 6.4 - 49e-5 for the sample grown at 310^{o}C and 320^{o}C, respectively. The lower Hooge constant corresponding to the higher electron mobility of the sample grown at 310^{o}C suggests the apparent improvement of the crystal quality. At 80 K, the constant α_H of both samples decrease, corresponding to the decreasing mobilities. It seems that there is a relationship between the Hooge parameter α_H and the electron mobility μ. In other studies [158; 153; 159], it is asserted that the Hooge parameter is mostly determined by fluctuations in carrier numbers. In

our case, however, the cleaved sample size is very small. A confirmation is, therefore, not clear.

We also investigate the generation-recombination noise for these samples. The temperature-dependence of the generation-recombination noise measured from 80 K to 300 K is indicative of trap states. Two deep traps 220 meV and 390 meV below the conduction band were detected . It appears that the origin of the traps in the different samples are of the same nature [34].

Figure 4.20: Schematic depiction of the structure InSb/Si.

4.2 InSb/Si system

The examined InSb/Si samples were grown under the growth conditions as presented in chapter 3, section 3.5. In addition, a schematic depiction of the structure is shown in Fig. 4.20.

4.2.1 Optimization of initial buffer layer

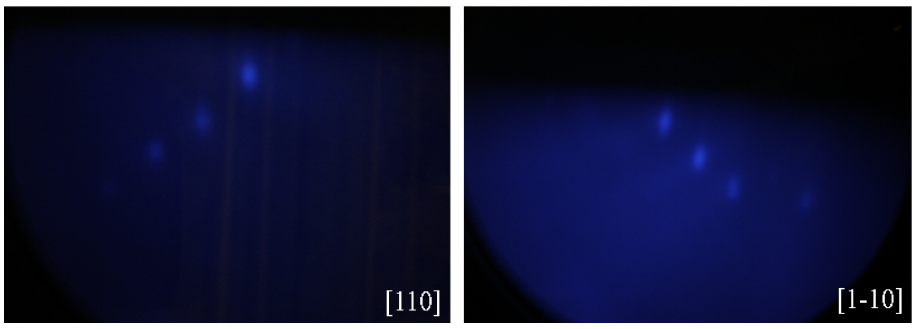

Figure 4.21: [110] and [1-10] RHEED patterns of InSb growth with GaAs buffer layer on Si (001) offcut by 4^o toward (110) at 380°C.

In the case of InSb/Si, it is much more difficult to get good crystal quality of InSb film due to about 19% lattice mismatch between eplilayer and substrate. This large lattice mismatch makes three dimensional polycrystalline growth begin at early stage of initial monolayers. It was found that using tilted substrates [3] or insertion of various buffer layers [4; 5; 6] may improve the crystal quality. In my work, I used p-type Si substrates with 4° off-cut towards (110) and resistivity of about 50-80 Ωcm. To improve the crystal quality, one of the applied techniques was two-step temperature growth: first growing of an InSb layer at 310°C and then increasing the substrate temperature and growth the second layer at this temperature. Since no success to grow InSb directly on Si substrate are obtained, the insertion of initial buffer layers between substrate and active InSb layer such as GaAs, AlSb, and GaSb/AlSb superlattice is necessary. This technique can help to suppress the formation of defects due to the lattice mismatch. As discussed about InSb/GaAs structure with good crystal quality and high mobility, therefore, I started to use GaAs as a buffer layer before deposited InSb layer. I grew InSb samples with 1000 Å-thick GaAs buffer layer at various temperatures from 280°C to 410°C on Si (001) offcut by 4^o toward (110). The growth rate of GaAs was about 0.73 $Å/s$. The temperatures for the growth of InSb layer varied from 310°C to 400°C. Figure 4.21 shows the [110] and [1-10] RHEED patterns of the InSb layer grown at 380°C. The RHEED intensity was not strong and the cloudy images indicate the inferior quality of the film. In addition, Hall measurements showed that the InSb film has very low electron mobility of 6000 cm^2/Vs at 300 K. For other samples, the mobility is even lower.

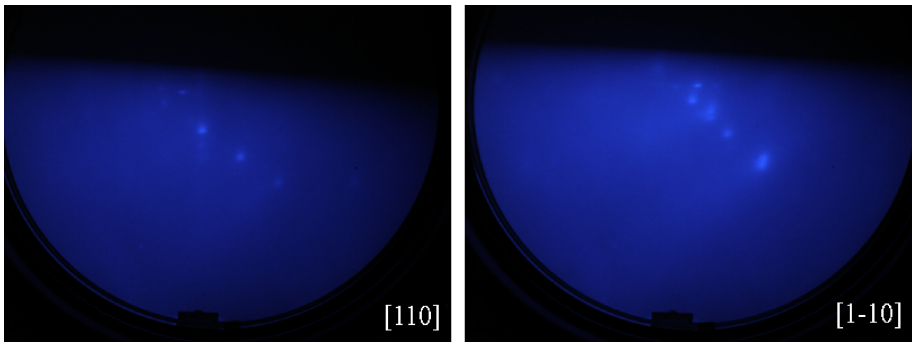

Figure 4.22: [110] and [1-10] RHEED patterns of the initial AlSb layer at 340°C on Si (001) offcut by 4^o toward (110) at 380°C.

Another possible buffer for interposition between InSb and Si is AlSb. Since AlSb has the lattice constant of 6.1355 Å, it can help to reduce the large lattice mismatch of about 19.3% between Si and InSb in two steps to about 5.6% [6]. I also used AlSb buffer layer for the growth of InSb/Si. The 1400 Å-thick buffer layer was grown at temperature range from 310°C to 410°C with the growth rate of about 2.3 Å/s. The observed RHEED patterns of the initial AlSb layer at 340°C is shown in Fig. 4.22. The InSb layer was then deposited on AlSb at the temperature range from 310°C to 400°C. However, the highest obtained mobility at 300 K is only about 8000 cm^2/Vs for the sample grown at 380°C with AlSb at 340°C.

Subsequently, GaSb/AlSb superlattice buffer layer was employed. After the cleaning process of the substrate, the substrate temperature was cooled down to the InSb growth temperature. A 30 period strained layer consisting of 0.06 μm GaSb/AlSb superlattice was then incorporated. 2 μm-thick InSb layer was deposited with an Sb/In flux ratio of about 5.6 and a growth rate of 2 Å/s. A growth temperature range between 280 and 400°C was investigated. I obtained better InSb films with GaSb/AlSb superlattice buffer layer compared to using GaAs and AlSb buffer layer. The results will be discussed in detail in next sections.

4.2.2 Structural properties

The RHEED patterns

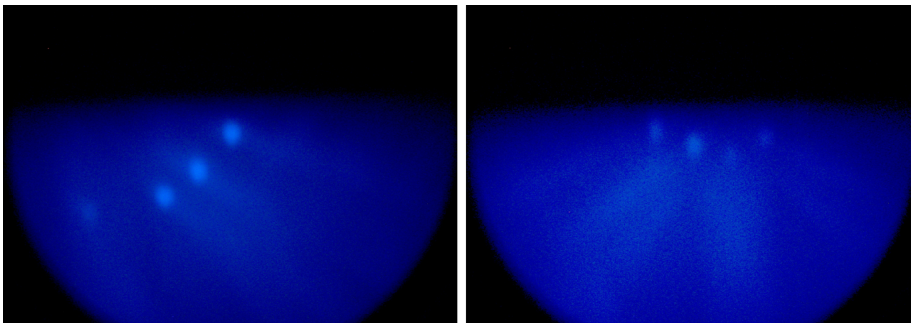

Figure 4.23: (1×1) RHEED patterns of the sample grown on Si substrate at 340°C.

The RHEED was employed during the growth of 2 μm-thick InSb layer with GaSb/AlSb superlattice buffer layer. The RHEED signals disappeared for the growth temperature lower than 340°C, probably due to the bad crystal quality. Figure. 4.23 shows the (1×1) RHEED reconstruction of the InSb film grown at 340°C. RHEED patterns obtained on samples grown over this temperature also showed similar behavior and thus are not presented here. While the streaky RHEED pattern refers to a flat surface, the spotty RHEED pattern corresponds to a rough surface or a surface with three dimensional islands. The RHEED pattern of this sample is spotty, indicating a rough surface. Furthermore, the cloudy appearance in the RHEED pattern reflects the presence of dislocations, which appear regardless of the inserted GaSb/AlSb buffer layer. In comparison with the RHEED pattern of the InSb/GaAs sample grown at 310°C, it is not cloudy, indicating a far superior level of InSb crystal quality.

The AFM topographs

The AFM scans of the sample grown at 340°C are shown in Fig. 4.24. Figure 4.24(a) in 50×50 μm scale indicates a rough surface morphology of the InSb epilayer, in agreement with RHEED results. The mean roughness of the film is about 300 nm. The surface consists of the crowded large grains in the range of μm as seen in Fig. 4.24(b).

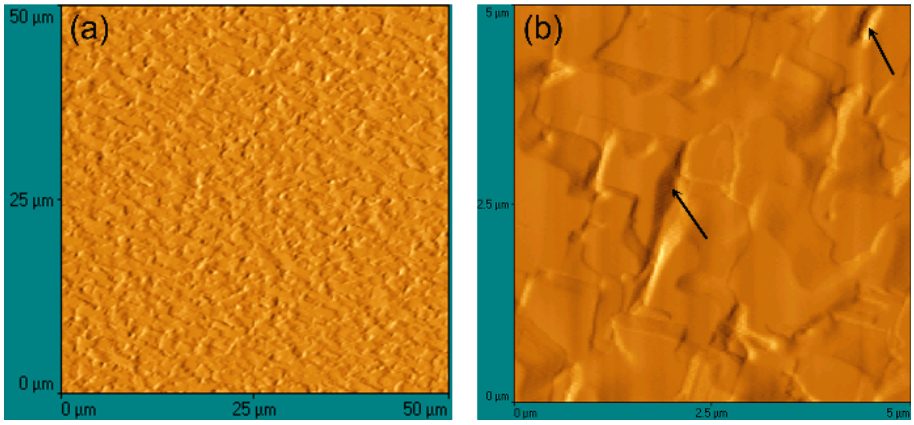

Figure 4.24: AFM scans of the sample grown at 340°C: (a) 50×50 μm scale, (b) closer scan in the 5×5 μm scale.

Additionally, the surface has some cracks, which are arrowed in the picture. The reason for these cracks may be due to the difference of thermal expansion coefficient between InSb and Si. Mori *et al.* [160] reported that the InSb films started to aggregate at the temperature over 300°C on Si. Note that with our MBE system, no success to grow InSb/Si at lower temperature than 340°C is obtained. This result suggests that the growth temperature of 340°C is low enough for the successful growth of InSb/Si and can not be the reason to cause the cracks on the surface.

From transmission electron microscopy: TEM images

The JEOL JEM-3010 transmission electron microscopy (TEM) which uses a LaB6 electron source (300 kV) to image a sample with resolutions down to 0.17 nm was used. The surface, interface structure and morphology of as-grown nanostructured materials can be determined quantitatively. Cross-sectional TEM examination for the sample grown at 340°C in the near-interface region is shown in Fig. 4.25. Figure 4.25(a) and (b) reveal the nature of the defects to be mainly microtwins and stacking faults along the (111) planes, labeled with blue arrows. A high density of threading dislocations is also observed, arrowed in purple. These twins and dislocations are most concentrated close to the interface and can also be observed several hundred nanometers away from the interface layer. However, in agreement with the RHEED results, the structure quality of the InSb films improves with increasing distance from the substrate. Above several hundred nanometers, mainly microtwins, stacking faults, and dislocations decrease in density as the layer thickness increases. The high-resolution TEM of the InSb/Si interface are shown in Fig. 4.25(c) and (d). One can see an array of edge misfit dislocations, which are arrowed in green. In addition, the roughening interface is assumed due to inter-diffusion and reaction between dislocations [135].

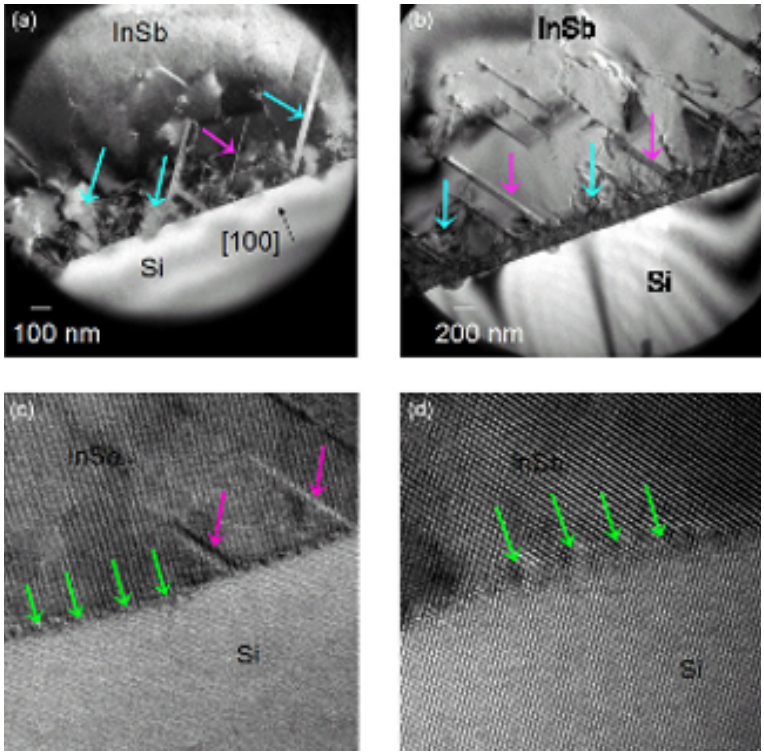

Figure 4.25: Cross-sectional TEM images for InSb layer grown on Si at 340°C: (a) and (b) bright-field images, (c) and (d) high-resolution micrographs of the InSb/Si interface layer.

4.2.3 Crystal diffraction

Figure 4.26 shows the (004) double-crystal X-ray (DCXR) patterns of two samples grown at 340°C and 380°C with GaSb/AlSb superlattice. Both the InSb and the GaAs peaks are clearly defined. The right shoulder of the InSb peak is due to the strain between the layers. The InSb peaks related with (004) plane appeared with high intensity. For the sample grown at 380°C, the FWHM is found about 951 arcsecs, which is the narrowest bandwidth among the InSb/Si samples grown at different conditions. The lattice constant of the InSb film determined from the XRD peak is 0.648 nm. This value matches closely the lattice constant of the InSb bulk. According to the data obtained from the atomic-force microscopy the root-mean-squared roughness (RMS) for areas around 2×2 μm^2 is lower than 16 nm. Our results show that good quality InSb epilayers can be grown on Si substrates using the GaSb/AlSb superlattice layer.

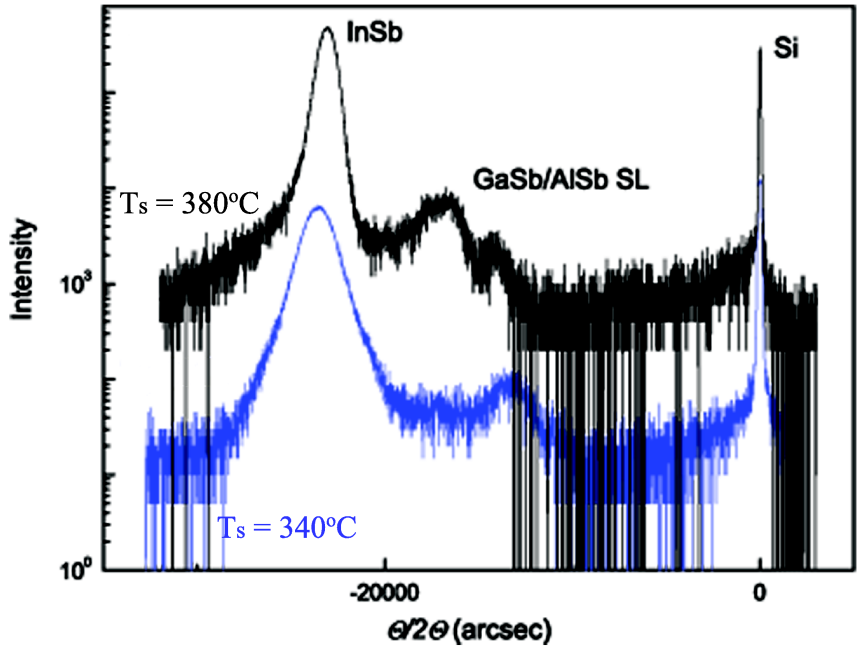

Figure 4.26: Double-crystal X-ray rocking curves for InSb/Si films grown at 340°C, 380°C.

4.2.4 Electronic properties

Figure 4.27 shows the Hall mobility as a function of temperature for the samples grown at 360°C, 370°C, 380°C, and 390°C. The temperature dependencies of the electron mobility in all samples are almost identical. The highest 300 K mobility was found to be 26500 cm^2/Vs for the sample grown at 380°C, corresponding to n=2.5e16 cm^{-3}, which is similar to the best samples on GaAs. By comparing Fig. 4.12 and 4.27, it is evident that that InSb/Si exhibits much lower 300 K mobilities and faster degradations at low temperatures than those in the InSb/GaAs samples. The electron mobility decreased with temperature in both cases. Similar to the GaAs-based samples, the electron mobility in the Si-based samples is limited by deformation potential scattering μ_d and is inversely proportional to the edge dislocation density D. However, in InSb/Si case, more dislocations can be generated in the grown InSb layer than those in the InSb/GaAs case. Therefore, the degradation of electron mobility observed at low temperature is higher.

4.2.5 Infrared transmission

For this study, Ernst *et al.* [148] measured the transmission spectra on my samples. Figure 4.28 shows the infrared transmission spectra for the samples grown on Si at

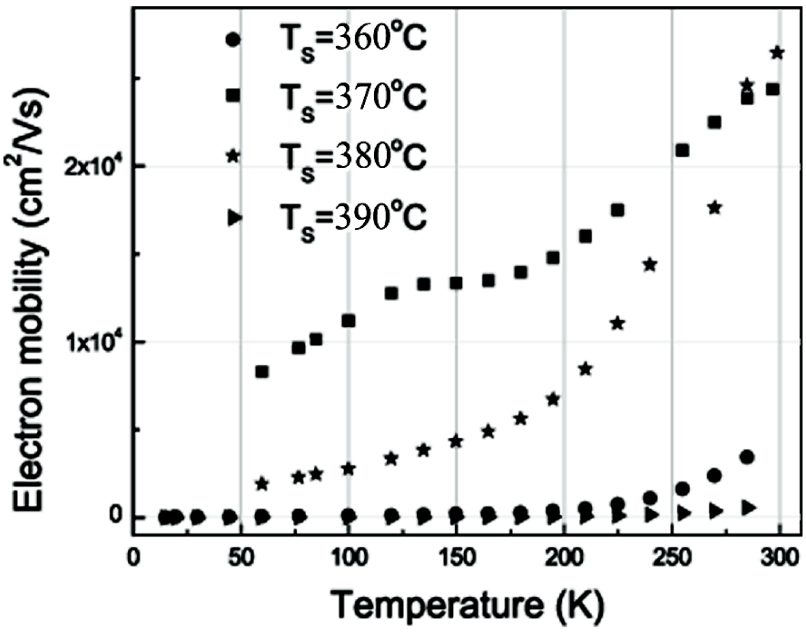

Figure 4.27: The temperature dependence of the electron mobilities for InSb/Si films.

340°C and 380°C. The method according to [149] is used for the analysis. Conversely to the GaAs-based samples, the obtained spectra are not as expected. It is, somehow, diffused. The part of the spectrum at higher wavenumbers may be attributed to artefacts in the detector, while the behavior at smaller wavenumbers is ambiguous: the absorption occurs even for very small energies, 620 cm^{-1} and 573 cm^{-1}, corresponding to 0.077 eV and 0.071 eV, respectively.

4.2.6 Noise

To further investigation of dislocation in the samples, noise spectroscopy was carried out on my samples by Dobbert. The samples grown at 340°C and 380°C were examined. At 300 K both samples exhibit similar flicker noise ($\propto$1/f) features and the Hooge factor α_H is about 5e-5 at 300 K. At 80 K α_H is 3e-4. Compared to those of the samples grown on GaAs as shown in Tab. 4.1, it can be seen that the sample grown on Si exhibits the lowest Hooge factor of examined samples at 300 K. The high level of the noise at 80 K must be attributed to the low electron concentration since the Hooge factors are rather small compared to the 300 K ones. Furthermore, compared to other epitaxially-grown InSb films [156; 157] the Hooge factors in this study are 10 to 100 times lower. At 300 K, the Hooge parameters correspond to the bulklike channels. At 80 K, on the other hand, the Hooge parameters of the GaAs-based samples correspond to degenerate, possibly two

dimensional channels; for the Si-based sample, to the interface channel. More results about noise properties of these samples can be obtained in our published papers [32; 33].

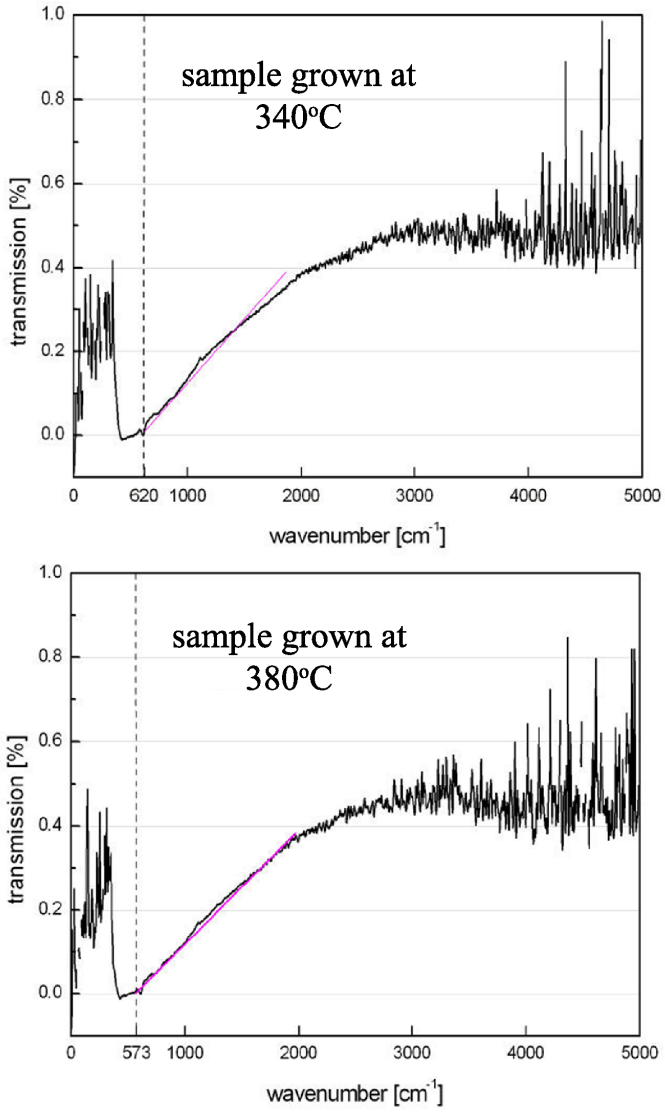

Figure 4.28: FT IR transmission spectra for samples grown at 340°C (top) and 380°C (bottom) [148].

4.3 Summary

To conclude, I have described the growth of high-quality InSb films on (001) GaAs as well as (001) Si substrates using MBE. My results indicate a significant correlation between the crystal quality of InSb films and the growth condition such as substrate temperature, growth rate, Sb/In flux ratio, and the substrate tilting. The optimal parameters include the substrate temperature of 310^{o}C, the growth rate of 2 Å/s, and the Sb/In flux ratio of 5.6 for growing directly on GaAs (001) substrate. The optimal conditions for the growth on Si substrate involve the same growth rate and Sb/In flux ratio but the substrate temperature was 380^{o}C and the substrate tilting of 4^o (001) offcut toward (110) were used. The buffer layer of 0.06 μm GaSb/AlSb superlattice is also required. The highest 300 K electron mobility was 41100 cm^2/Vs for a 2μm-thick InSb film grown directly on GaAs at a substrate temperature of 310^{o}C. However, the electron mobility degradation and the carrier freeze-out at low temperatures were also observed. To reduce these factor, the samples grown on GaAs were doped by Si with the doping level of 2e16 cm^{-3}. The high mobilities measured at low temperatures suggest the ability for the electronic device applications. Deep level noise spectra indicate the existence of the deep levels in both GaAs and Si-based samples. The samples grown on Si exhibits the lowest Hooge factor at 300 K compared to the samples grown on GaAs.

5 (In,Mn)Sb/GaAs system: characterization and properties

In the previous chapter, properties of the non-magnetic InSb have been discussed. In order to observe magnetic cooperative phenomena in the diluted magnetic semiconductor system, I introduced a sizable amount of Mn element to the host material InSb using the epitaxial method. Hence, this chapter is dedicated to properties of (In,Mn)Sb/GaAs system. The methods used for characterization are also described in detail.

5.1 Growth of (In,Mn)Sb on GaAs (001) substrate

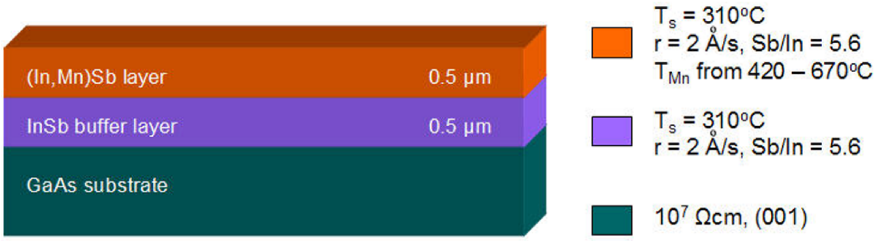

Figure 5.1: Schematic depiction of the structure (In,Mn)Sb/GaAs with detailed growth conditions.

I grew $In_{1-x}Mn_xSb$ films on semi-insulating epi-ready GaAs (001) under the growth conditions as presented in chapter 3, section 3.5. In addition, a schematic depiction of the structure is shown in Fig. 5.1. Samples were used in my study with the various Mn concentrations corresponding to the different temperatures of the Mn effusion cell from 420^{o}C to 670^{o}C. The Mn concentrations were estimated from the Mn/In flux ratio, and confirmed by using a dynamical simulation of rocking curve analysis to be smaller than 1%. A well-defined (2×4) reconstruction of RHEED pattern was observed during the growth of the InSb film and also the (In,Mn)Sb film as shown in Fig. 5.2. All samples have mirror-like surfaces.

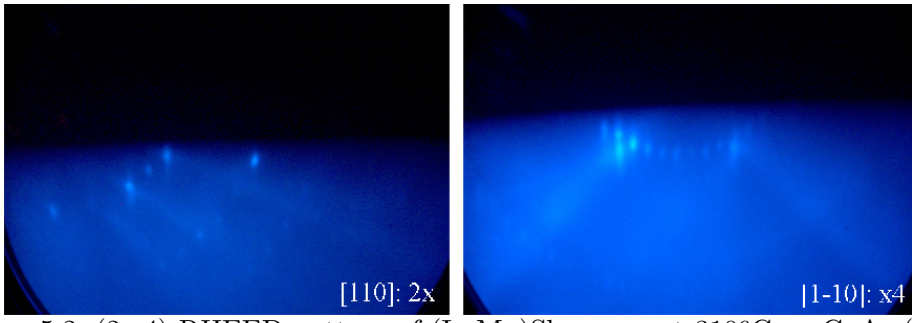

Figure 5.2: (2×4) RHEED pattern of (In,Mn)Sb grown at 310^{o}C on GaAs (001).

5.2 Mn concentration and lattice parameter

Determination of the Mn concentration

Mn composition can be measured using several methods such as reflection high energy electron diffraction (RHEED) [161], x-ray diffraction (XRD) [162; 59], channeling particle induced X-ray emission (c-PIXE), channeling Rutherford backscattering (c-RBS) [99], in-situ ion gauge [163; 162], electron probe microanalysis (EPMA) [164; 165; 162] and secondary ion mass spectrometry (SIMS) [166; 162]. In my work, I estimated firstly the Mn concentrations from the Mn/In flux ratio. The In and Mn flux are adjusted using the *in situ* beam monitoring ion gauge to have an approximately equal intensity, take into account the different gauge sensitivity for these two elements. The nominal compositions x are about 0.7%, 0.4%, and 0.2% for the samples grown with Mn effusion cell temperatures of 670^oC, 600^oC, and 560^oC, respectively. After the growth, the samples were under x-ray measurements. By using the high resolution double crystal x-ray diffraction (XRD), the rocking curves for both symmetric (004) and asymmetric (115) reflections were obtained. In order to estimate the average Mn content in the samples, the experimental rocking curves were then compared to simulated rocking curves obtained from a dynamical simulation of rocking curve analysis (RADs) [133]. RADs is a program that uses the fundamental x-ray scattering equations of dynamical diffraction to analyze rocking curves. Therefore, by matching simulation to experiment, it is possible to obtain information such as the composition, number, thickness and strain of layers in a structure. For the simulation, first is making a model consisting of GaAs substrate, InSb buffer layer and $In_{1-x}Mn_xSb$ layer. It is then necessary to set up parameters such as the instrument parameters (wavelength, polarization of the x-ray beam; material, orientation, tilt, reflection, number of reflections of the beam conditioner), the experimental parameters (reflection geometry, scan range), and the sample parameters (thickness units, strain type, curvature). The final step is click the simulate tool. Once simulation is complete, RADs plots out a simulated rocking curve on screen. The $In_{1-x}Mn_xSb$ samples grown with Mn effusion cell temperatures between 560^oC and 670^oC were examined and the respectively deduced Mn compositions are smaller than 1%. The results agree with the *in situ* beam ion gauge data.

Lattice parameter

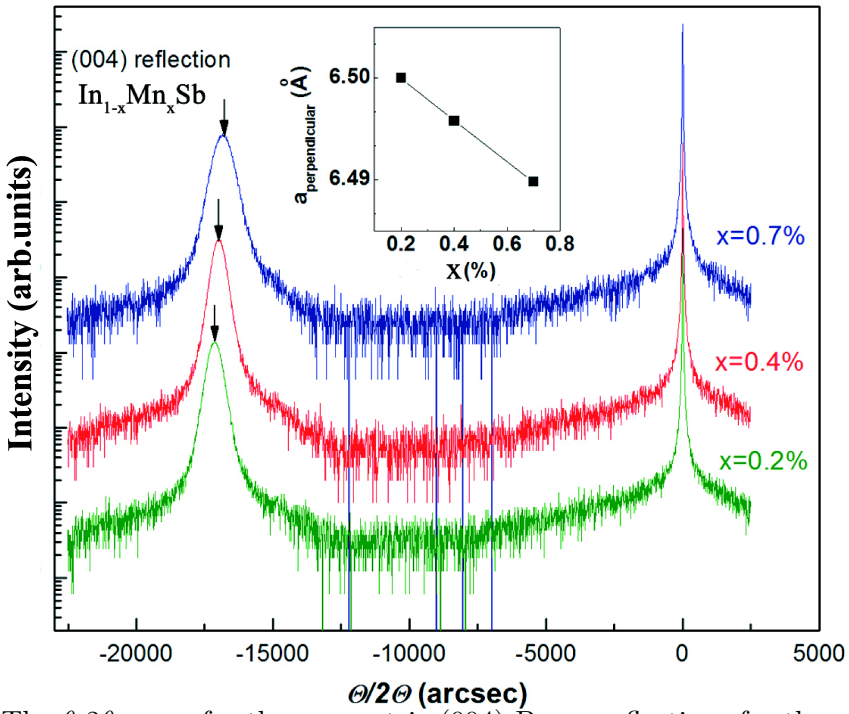

Figure 5.3: The θ-2θ scans for the symmetric (004) Bragg reflections for three samples. Inset shows the perpendicular lattice constants of the epilayers as a function of the Mn contents.

Figure 5.3 shows the θ-2θ scans for the symmetric (004) Bragg reflections of three specimens with the Mn concentration of 0.7%, 0.4%, and 0.2%. It is general believed that in perfectly crystalized samples the presence of MnSb is reduced to zero at the Mn content range ($< 1\%$) and Mn simply substitutes for In site. Moreover, the atomic radius of Mn atoms (r_{Mn}=1.29 Å) is smaller than that of In atoms (r_{In}=1.63 Å) and the recent theoritical lattice constant of zincblende MnSb (a_{MnSb}=6.166 Å) [167] is also smaller than that of InSb (a_{InSb}=6.479 Å). Therefore, the lattice constant of the magnetic layer $In_{1-x}Mn_xSb$ should be smaller than that of InSb layer grown at the same conditions. However, I saw no difference in angular position of diffraction peaks between $In_{1-x}Mn_xSb$ layer and InSb buffer layer in each sample. It reflects that the perpendicular lattice constant $a_\perp$ of $In_{1-x}Mn_xSb$ layer and InSb buffer layer are at the equal level. There is a possibulity that Mn atoms enter not only to the In sites but also to the interstitial sites and another possibility that can be occurred is the presence of Sb at In sites. These defects, the interstitial Mn (Mn_I) and Sb antisites (Sb_{In}), can influence the lattice constant of InMnSb layer and make it expansible to that of InSb buffer layer. The behavior of these compensating defects is confirmed by many studies of GaMnAs [168; 169]. If it is also true for InMnSb, it is very interesting to make further explorations in order to know their concentrations, their behaviors and how they affect the crystal structures of this material. To date, no experimental data and theoretical

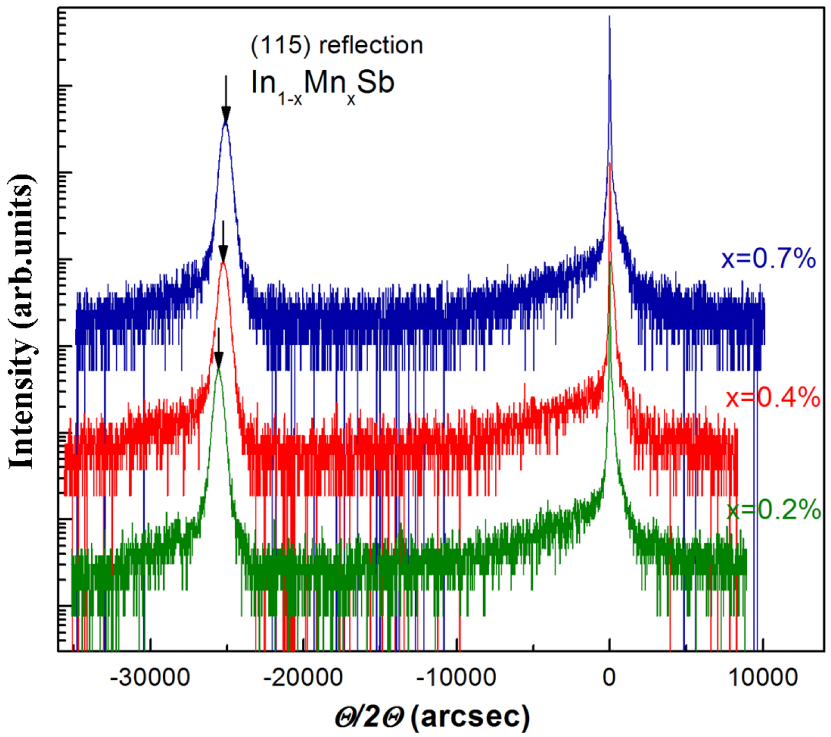

Figure 5.4: The θ-2θ scans for the asymmetric (115) Bragg reflections for three samples.

studies revealing their concentrations and their effects are available yet. Figure 5.3 also shows another feature concerning the InMnSb lattice parameter. The significant changes in angular positions of InMnSb (004) diffraction peaks of the three samples can be observed, suggesting the differences between the lattice constants of these samples. Note that they contain the Mn concentration limit $x \leq 1\%$. At this low Mn content range, the lattice constant of InMnSb decreases with increase Mn concentration. The inset in the figure 5.3 illustrates the perpendicular lattice constants of the epilayers as a function of the Mn contents. The InMnSb lattice constant decreases with the increasing Mn composition at the low Mn concentration range. As assumed of the interstitial Mn and Sb antisites, and expected that their densities are constant at the low Mn concentration limit range, Mn_{In} increases, therefore, with increasing x at $0.2\% \leq x \leq 0.7\%$. It results the decrease of perpendicular lattice constant of the InMnSb layer from 6.50000 Å to 6.48980 Å corresponding to the increase of x from 0.2% to 0.7%. However, the observation of the decreasing lattice constant of the InMnSb layer with the increasing Mn content also opens a question that why the lattice constant of the non-magnetic InSb buffer layer also decreases with the increasing Mn concentration. The (004) Bragg reflections are measured of the lattice parameters perpendicular to the epilayer plane $a_\perp$ for all samples. The combination of these and the asymmetric (115) Bragg diffractions are then used to calculate the in-plane lattice constants $a_\parallel$. These asymmetric (115) $\theta - 2\theta$ scans are shown in Fig. 5.4. The values of $a_\parallel$ are obtained to be 6.46780 Å, 6.46830 Å and 6.47050 Å for the Mn content of 0.7%, 0.4% and 0.2%, respectively. It can be seen that $a_s < a_\parallel < a_\perp$, where a_s=5.65325 Å is the cubic lattice constant of

Table 5.1: The results for the perpendicular lattice constant $a_\perp$, the in-plane lattice constant $a_\parallel$, the relaxed lattice constant a_{relax} and the degree of strain m of samples with different Mn content.

Sample ($\%Mn$)	$a_\perp$ (Å)	$a_\parallel$ (Å)	a_{relax} (Å)	m
0.7	6.48980	6.46780	6.47350	0.14510
0.4	6.49580	6.46830	6.47550	0.14540
0.2	6.50000	6.47050	6.47820	0.14590
0.0	6.50160	6.47260	6.48010	0.14630

the GaAs substrate. The data indicates the epilayers to be strain-relaxed on the GaAs substrate. They are biaxially compressed with the transverse strain component $\varepsilon_\parallel$ and the perpendicular strain component $\varepsilon_\perp$. Assuming that the InSb elastic constants are approximate those of $In_{1-x}Mn_xSb$, therefore, the following identities are exposed:

$$\varepsilon_\parallel = \frac{a_\parallel - a_{relax}}{a_{relax}}\,, \tag{5.1}$$

$$\varepsilon_\perp = \frac{a_\perp - a_{relax}}{a_{relax}}\,, \tag{5.2}$$

$$m = \frac{a_{relax} - a_s}{a_s}\,, \tag{5.3}$$

$$\nu = -\frac{\varepsilon_\parallel}{\varepsilon_\perp}\,, \tag{5.4}$$

where a_{relax} is the relaxed layer lattice parameter, m is the relaxed mismatch, ν is the Poisson's ratio and has a value of 0.35 for the epilayers [12]. Following these equations, the values of a_{relax} and m are determined.

The measured values of $a_\perp$, $a_\parallel$ and the deduced values of a_{relax} and m for all three samples and for an undoping InSb sample are then collected in Tab. 5.1. In the sample with 0.7% Mn, the ralaxed lattice constant of the epilayer is the lowest, whereas the lattice constant of the epilayer in the sample without Mn is the highest. It can be seen that the epilayers are less relaxed if the Mn density is bigger. As concerns Mn_I and Sb_{In} defects in the sample, the increasing density is accompanied the significant influences on the lattice parameters of the material. The (In,Mn)Sb alloy, the presence of MnSb clusters as well as Mn_I and Sb_{In} defects can contribute to the reduced average lattice constant. The Mn also apparently reduces the relaxation of the InSb grown on GaAs. For pure InSb, the 2-μm film is essentially 100% relaxed and its lattice constants, both parallel and perpendicular to the growth plane, are that of bulk InSb (see chapter 4). The Mn both decreases the average lattice constant and the relaxation, resulting in a somewhat larger lattice constant perpendicular to the growth plane [91].

5.3 Negative magnetoresistance and anomalous Hall effect

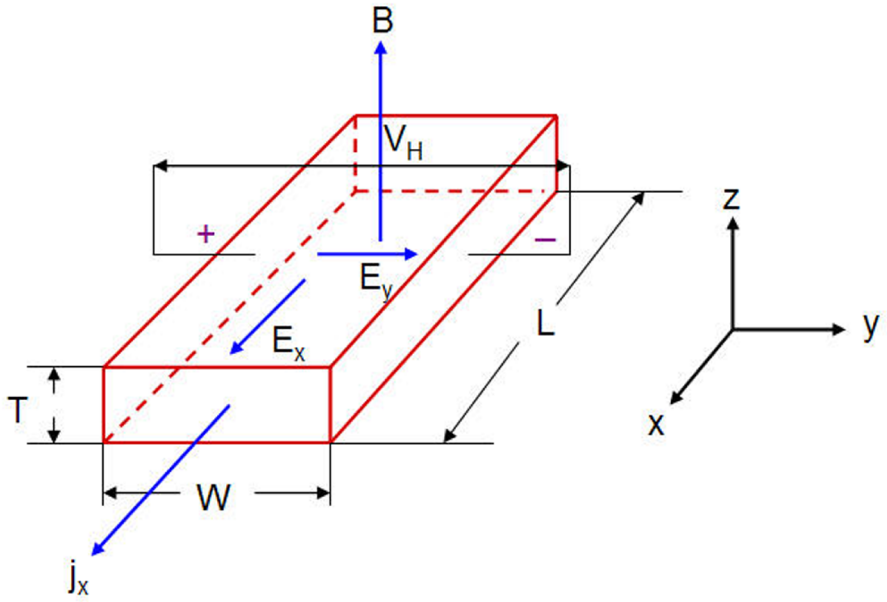

Figure 5.5: A Hall bar measurement. Current j flows in the x direction. The applied magnetic field B is in the z direction. For a p-type sample an internal electric field E applies in the y direction.

5.3.1 Hall-bar measurements

Definitions

As discussed in chapter 4, section 4.1.3, in order to assess the transport properties, it is necessary to determine the resistivity ρ and carrier density n. The combination of ρ and n allows to determine the drift mobility μ. One way to combine both these measurements is to mount sample as Hall bar (Fig. 5.5) aligned to the direction in which transport properties can be determined. In anisotropic transport the drift mobility μ is replaced by the drift mobilities along the two principal transport directions x and y, μ_x and μ_y. Magnetoresistance measurements, such as Hall-bar measurements, measure the components of the resistivity tensor of the material.

$$\widehat{\rho} = \begin{bmatrix} \rho_{xx} & \rho_{xy} \\ \rho_{yy} & \rho_{yx} \end{bmatrix} \tag{5.5}$$

where resistivities ρ_{xx}, ρ_{xy}, ρ_{yy}, and ρ_{yx} are given by

$$\rho_{xx} = \frac{E_x}{j_x}, \rho_{xy} = \frac{E_y}{j_x}, \rho_{yy} = \frac{E_y}{j_y}, \rho_{yx} = \frac{E_x}{j_y} \tag{5.6}$$

The current density j_x and j_y along the respective directions x and y one gets

$$j_x = \sigma_{xx}E_x + \sigma_{xy}E_y, j_y = \sigma_{yx}E_x + \sigma_{yy}E_y \tag{5.7}$$

where σ is conductivity. In the Hall-bar measurement, longitudinal voltage and Hall-voltage are measured without drawing a current. Measuring the Hall-voltage results no current flow ($j_y = 0$). Therefore,

$$\rho_{xx} = \frac{\sigma_{yy}}{\sigma_{xx}\sigma_{yy} - \sigma_{xy}\sigma_{yx}} \tag{5.8}$$

$$\rho_{xy} = \frac{-\sigma_{yx}}{\sigma_{xx}\sigma_{yy} - \sigma_{xy}\sigma_{yx}} \tag{5.9}$$

$$\rho_{yy} = \frac{\sigma_{xx}}{\sigma_{yy}\sigma_{xx} - \sigma_{yx}\sigma_{xy}} \tag{5.10}$$

$$\rho_{yx} = \frac{-\sigma_{xy}}{\sigma_{yy}\sigma_{xx} - \sigma_{yx}\sigma_{xy}} \tag{5.11}$$

The Hall coefficient R_H and the carrier density n_H are determined

$$R_H = \frac{\rho_{xy}}{B} \tag{5.12}$$

$$n_H = \frac{-1}{eR_H} = \frac{-B}{e\rho_{xy}} \tag{5.13}$$

Setups

I used a photolithographically patterned Hall bar with a width of 2 mm and a length of 8 mm, as shown in Fig. 5.6 (right). Eight indium contacts with small dimensions in comparison with the length of sample were made on the edges of the sample by annealing at 200^{o}C for 2 minutes. The contact resistances are negligible. For each measurement, two samples were mounted on a chip holder, wired, and affixed to the sample holder (Fig. 5.6 (left)), which was in turn inserted in a Oxford helium cryostat. The measurements were carried out using a 7 T superconducting magnet with a variable temperature insert over the temperature range 1.5 K - 300 K. The magnetic field was applied perpendicular to the layer plane. The temperature-dependent resistance was measured for a current I of 10^{-4} A, at magnetic field of 0.5 T, while the dependence of the resistance on magnetic field was measured for the same current, at temperature of 300 K, 4.2 K and 1.5 K.

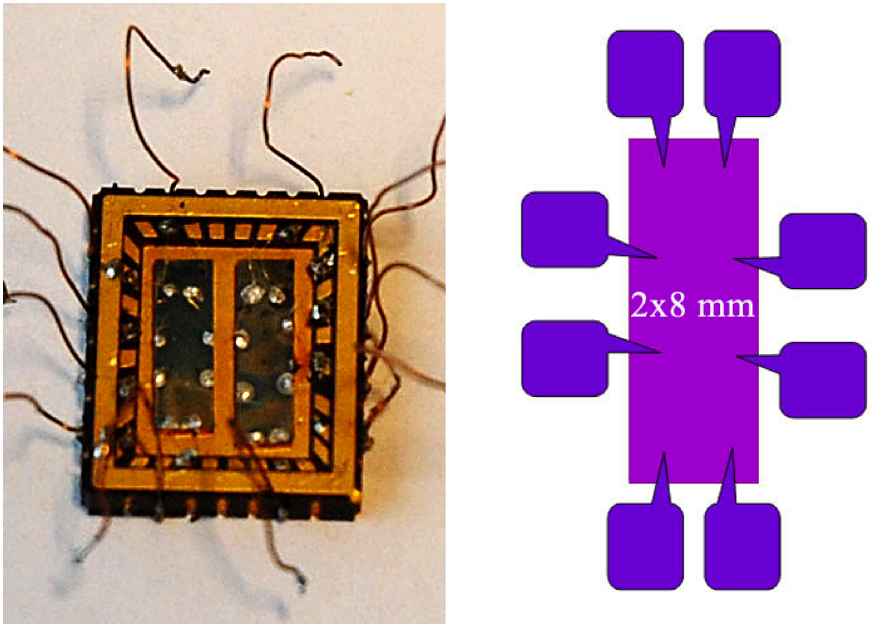

Figure 5.6: Hall-bar structure. **left:** Two samples were mounted on a chip holder and wired. **right:** an entire structure.

5.3.2 Negative magnetoresistance

The magneto-transport properties have been studied using Hall-effect measurements in the temperature range of 1.5 to 300 K. The magnetoresistance (MR) is calculated using the conventional expression

$$\Delta\rho/\rho_0 = (\rho_H - \rho_0)/\rho_0 \tag{5.14}$$

where ρ_0 is the resistivity at zero field. Figure 5.7 (a) shows magnetic-field-dependent magnetoresistance measured at 1.5 K for the (In,Mn)Sb films with different Mn concentration. The magnetoresistance is found to be sensitive to the Mn concentration. Samples with Mn content x of 0.7% and 0.4% show a small positive magnetoresistance at low field followed by large negative magnetoresistence at higher field. This behavior was also seen in the (Ga,Mn)As/GaAs and (Ga,Mn)Sb/GaSb system [170] and the authors attributed this effect to the contribution from the parallel conductance via the underlying GaAs substrate in the (Ga,Mn)As/GaAs samples and GaSb substrate in the (Ga,Mn)Sb/GaSb samples. But it also has been seen in my (In,Mn)Sb/GaAs samples (the host material of the epi-layer is not the same as the substrate) and is sensitive to the Mn concentration. I suppose, that such a parallel conducting channel, if it exists, plays only a minor role. In the sample with the lowest Mn concentration of 0.2%, the low-field positive magnetoresistance disappears, leaving negative magnetoresistance at all field. The low-field positive magnetoresistance can thus not be explained by contribution from

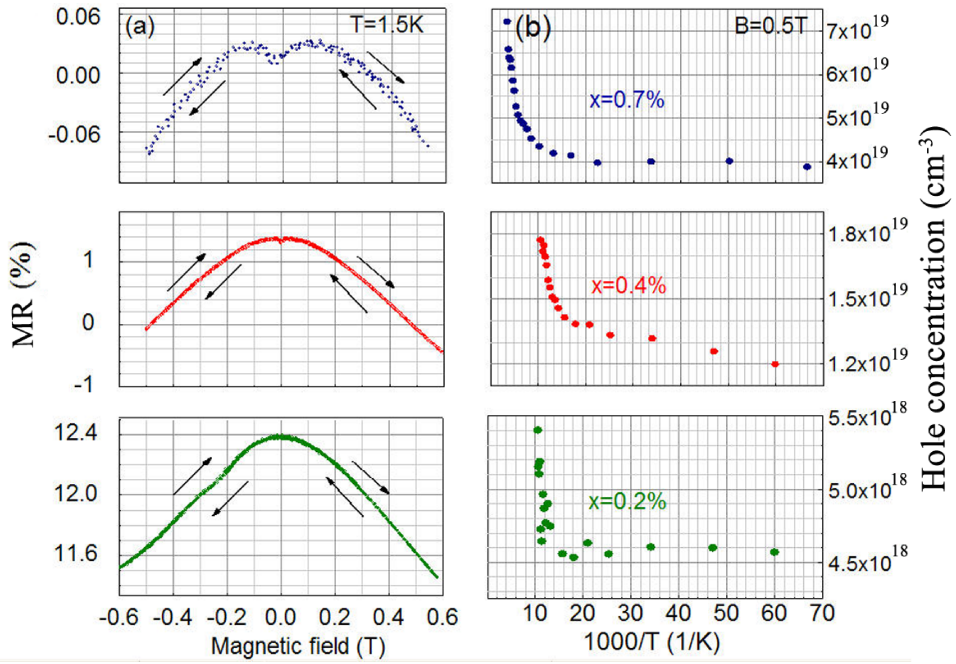

Figure 5.7: (a) Magnetic-field-dependent magnetoresistance measured at 1.5 K and (b) Carrier concentration as function of temperature measured at 0.5 T for (In,Mn)Sb films with different Mn concentration when the field applied perpendicular to the layer plane.

the parallel conductance only - there has to be clearly to Mn presence. The change in negative magnetoresistance, however, is slight. The interactions between the localized magnetic moments of the substitutional Mn acceptors and the holes in an impurity may result the negative magnetoresistance. Oiwa *et al.* [171] and Iye *et al.* [172] observed the large negative magnetoresistance in the $Ga_{1-x}Mn_xAs$/GaAs ($0.015 < x < 0.071$) samples and proposed the Anderson localization [173; 174] for the explanation of the negative magnetoresistance in these samples. This scenario may be also applied to the present case of $In_{1-x}Mn_xSb$/GaAs samples.

If a semiconductor is doped with impurities, then states closed to the band edges may be induced, and electrons may be thermally excited in to or out of these impurity states. When a semiconductor becomes ferromagnetic, spin splitting of the conduction as well as the valence bands are expected to occur due to s-d and p-d exchange interactions. Figure 5.8 shows the band energy in the Anderson localized regime. The Fermi energy E_f lies on the localized side of this edge energy E_m (it is also named as "mobility edge" - the critical point at which a transition from localized to extended character of the eigenfunctions occurs in the random lattice problem). The conductivity at low temperature is exponentially dependent on the localization length [172]

$$\xi \sim |E_m - E_f|^{-\nu} \tag{5.15}$$

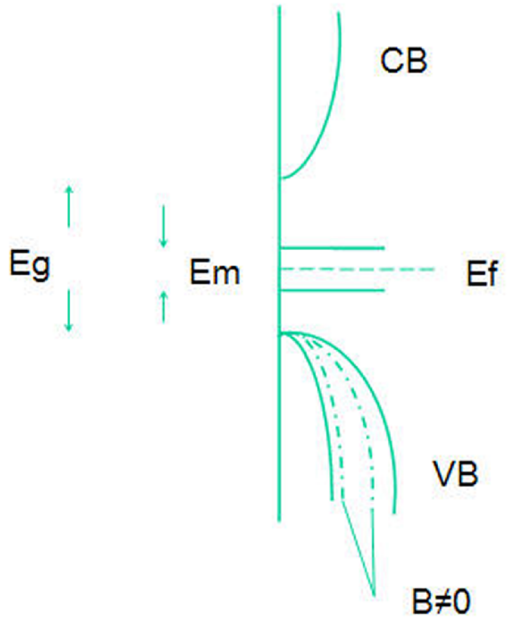

Figure 5.8: Band energy of (In,Mn)Sb in the Anderson localized regime.

where the value of exponent ν is close to unity. The effect of a magnetic field is to cause a Zeeman shift of the Fermi energy by $\pm g\mu B$ (g: factor enhancement, $\mu = e\hbar/2m_e$: Bohr magneton). This gives rise to a decrease in $E_m - E_f$ for one of the two spin subbands, and causes negative magnetoresistance. In the case of diluted magnetic semiconductors, the Zeeman shift of the Fermi energy $\pm g\mu B$ can be much larger, and the mobility edge may also be shifted as the magnetic field quenches disorder by aligning the Mn moments. The sample with 0.2% Mn may contain more diluted magnetic contributions than two others. The AFM and TEM measurements, which will be presented in section 5.4, also show that this sample has less MnSb clusters than two others.

The temperature- dependent carrier concentration measured at 0.5 T of these three (In,Mn)Sb samples is shown in Fig. 5.7 (b). The hole concentration p of the (In,Mn)Sb films at 300 K is measured to be 7.4e19 cm^{-3}, 1.8e19 cm^{-3}, and 5.4e18 cm^{-3} for sample with the Mn content of 0.7%, 0.4%, and 0.2%, respectively. The sample without Mn grown at the same conditions has n-type conductivity and electron concentration of 2.2e16 cm^{-3} at 300 K. All the samples have a similar behavior at high temperature range ($>$ 100 K) - decreasing carrier concentration as decreased temperature. The carrier concentration at low temperatures (e.g. below 50 K) in each sample is stable, indicating the carriers due to the impurities (scatterers). A different number of ionized impurities depends on the Mn content. The hole concentration increases with increasing Mn concentration owing to the increased acceptor concentration. Electrical parameters of these four films are given in Table 5.2.

Figure 5.9 shows a plot of resistivity as a function of temperature (B=0) of above

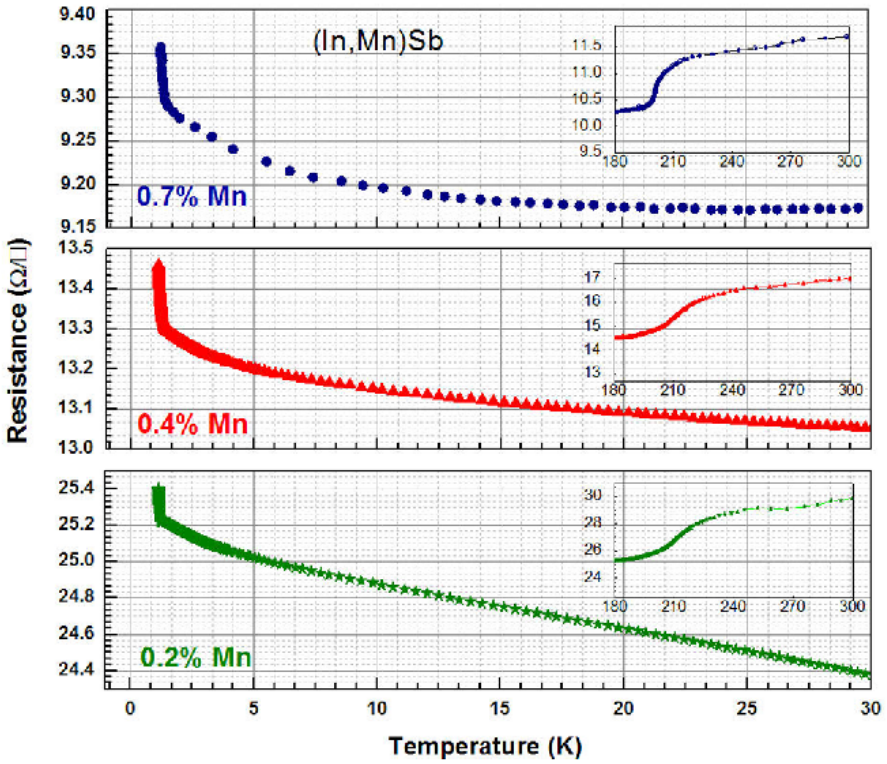

Figure 5.9: Temperature-dependent resistivity of (In,Mn)Sb films with different Mn concentration x.

(In,Mn)Sb films. The resistivity decreases with increasing Mn concentration due to the increased carrier concentration. It is also seen that the resistivity decreases with temperature on cooling from 300 K to around 30 K. An anomalous behavior from 250 K to 200 K may be resulted by effect of the substrate conductance [175]. The resistivity data at temperature lower than 30 K show an increased resistivity with decreasing temperature. The higher resistance at low temperature are expected due to compensation of Mn acceptors through point defects such as Mn interstitial sites. This rise of resistance suggests ionized impurity and spin disorder scattering. The ferromagnetic interaction in the present set of these alloys is mediated by localized holes, rather than metallic holes [91]. The similar behavior was also observed on (In,Mn)Sb films studied by Ganesan *et al.* [10]. It has been seen that conductivity of this material is dominated by Mott's variable range-hopping mechanism

$$\rho(T) \sim \exp(\frac{T}{T_o})^{1/4} \tag{5.16}$$

Table 5.2: Electrical parameters of (In,Mn)Sb films with different Mn content at 15 K and 300 K.

Sample (%Mn)	Resistivity (Ωcm)		Carrier conc. (cm^{-3})		Mobility (cm^2/Vs)	
	15 K	300 K	15 K	300 K	15 K	300 K
0.7	0.2	0.3	4.1e19	7.4e19 (p-type)	250	190
0.4	0.3	0.4	1.2e19	1.8e19 (p-type)	410	250
0.2	0.6	0.7	4.6e18	5.4e18 (p-type)	480	340
0.0	35	9.2	5.1e15	2.2e16 (n-type)	24000	41100

where ρ is resistivity. Theory predicts [176]

$$T_o = \frac{14}{g(E_F)a_B^{*2}} \tag{5.17}$$

where $g(E_F)$ is the density of states at the Fermi level and a_B^* is the Bohr radius of the donors.

The Mn interstitial sites are well known to compensate carriers. The carrier concentration of the films at 300 K is deduced to be 7.4e19 cm^{-3}, 1.8e19 cm^{-3}, and 5.4e18 cm^{-3} for sample with the Mn content of 0.7%, 0.4%, and 0.2%, respectively. At 15 K, the corresponding carrier concentration decreases to be 4e19 cm^{-3}, 1.2e19 cm^{-3}, and 4.6e18 cm^{-3}. In the metallic (Ga,Mn)As, (Ga,Mn)Sb alloys [177; 178; 179], and other studied (In,Mn)Sb system [7; 94], the temperature dependent of resistivity at zero field presents a maximum. This peak signals the presence of the critical scattering associated with the transition between the ferromagnetic and paramagnetic phases and provides convenient estimates of the Curie temperature. The behavior of these series (In,Mn)Sb is somehow similar to nonmetallic (Ga,Mn)As samples with high ferromagnetic transition temperature, which could not be determined from transport measurements [180; 171]. The magnetization measurements provide the hysteresis loops above 200 K for all three samples, which are discussed in section 5.4.

5.3.3 Anomalous Hall effect

It is well-known that the Hall resistance in a ferromagnetic material contains an ordinary contribution, which proportional to the external magnetic field, and an anomalous contribution, which often assumed to be proportional to the sample magnetization [181]. It can be expressed by the following equation

$$R_{Hall} = (R_O/d)B + (R_A/d)M \tag{5.18}$$

where R_O and R_A are ordinary and anomalous Hall coefficients, respectively, B is the applied magnetic field, M is the magnetization and d is the sample thickness. The second

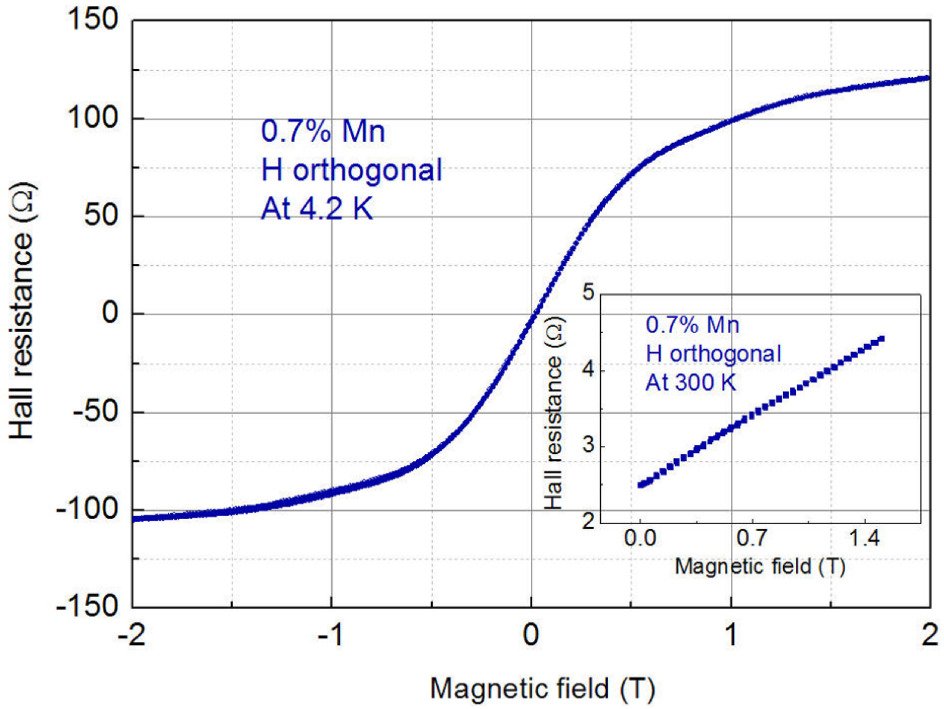

Figure 5.10: Field dependence of the Hall resistance measured at 4.2 K in the (In,Mn)Sb sample with 0.7% Mn. Magnetic field applied perpendicular to the layer plane. Inset shows the $R_{Hall}(H)$ curve at 300 K.

term presents the anomalous Hall effect (AHE), which is properly caused by anisotropic scattering between the carriers and local magnetic moments of Mn atoms. However, the mechanism of the AHE has long been controverted whether it is intrinsic or extrinsic and how to involve with the carriers and local magnetic moments scattering. Karplus *et al.* [182] attributed firstly the AHE to the intrinsic mechanism, in which the matrix elements of the current operators are required. Recently, the theoretical studies of the AHE relate the intrinsic-origin AHE to Berry phase effects[1], in which the transverse conductivity σ_{xy} is relative to the Berry phase curvature [181; 183; 184; 185]. Therefore, the study of σ_{xy} is necessary for ferromagnets. Other reports [186; 187] proposed to the extrinsic mechanism, in which the impurity scattering modified by the spin-orbit interaction plays an important role. It has been shown that the extrinsic mechanism is complicated and depends strongly on the impurities and the band structure of the materials. Nevertheless, the conventional expression (Eq. 5.17) is derived in all these

[1] Waves are characterized by amplitude and phase. The Berry phase occurs when both parameters are changed simultaneously but very slowly (adiabatically), and eventually brought back to the initial configuration. In quantum mechanics, this could e.g. involve rotations but also translations of particles. It is possible that the initial and final states differ in their phases. This phase difference is the Berry phase, and its occurrence typically indicates that the system's parameter dependence is singular (undefined) for some combination of parameters (from www.wikipedia.org).

theories for the AHE. In my study, I show the experimental results, in which the AHE was observed. As seen in the Fig. 5.10, the $R_{Hall}(H)$ curve of the sample with 0.7% Mn measured at 4.2 K shows an unusual behavior of Hall resistance in the low field region, when I sweep the field from negative to positive value. This observation establishes the ferromagnetism of the material. However, the width of the hysteresis is narrow and could not be determined. It was possible to measure the $R_{Hall}(K)$ at 4.2 K and at 300 K. The Hall resistance at 300 K is found to be linear in the used field region (Inset Fig. 5.10). Oiwa *et al.* [188] has investigated the anomalous Hall effect in the (In,Mn)As samples grown on (Ga,Al)Sb substrate. In this system, it has been shown that the shape of the hysteresis loop depends on the magnetic anisotropy. (The origin of magnetic anisotropy in ferromagnetic zinc-blende DMS is discussed in references [189; 190]). For example, if the hysteresis loop is square in shape, the sample has a strong perpendicular magnetic anisotropy. The magnetization vector is always fixed normal to the layer plane, and only the perpendicular component of the applied magnetic field is effective. By contrast, the relatively weak magnetic anisotropy results the magnetization in the direction of the applied magnetic field. Oiwa also attributed the phenomenon of the difference in magnetic anisotropy to the lattice-mismatch-induced strain in the magnetic layer. If the thickness of the magnetic layer exceeds the critical value, the strain energy builds up to a point where it becomes energetically favorable to form misfit dislocations. At this point, the lattice-mismatch-induced strain is mostly relaxed and results weak magnetic anisotropy. It is believed that the lattice-mismatch-induced strain is the principal factor of the magnetic anisotropy, although other sources such as dislocation density and carrier density have to be considered for quantitative account of this phenomenon. Whether this explanation can be also applied to the present case of my $In_{1-x}Mn_xSb$/GaAs samples or not, it is still unclear. However, I can imagine that only some of the total Mn spins appear to contribute the hysteresis loop at the low field. Some part of the others may be buried in the depletion layer region, where the hole concentration can be lower than the critical value for the present of carrier-induced ferromagnetism. These non-ferromagnetic Mn spins need much higher field to align. The rest of the non-ferromagnetic Mn spins may coexist with the ferromagnetic clusters in the interior of the (In,Mn)Sb layer.

5.4 Magnetization measurements

For the magnetic characterization, I used a superconducting quantum interference device (SQUID) to carry out the measurements on (In,Mn)Sb samples. The SQUID is capable of resolving changes in external magnetic field as large as 7 T. The magnetic field can be applied parallel or perpendicular to the sample layer plane. A measurement is performed by moving a sample through a system of superconducting detection coils which are connected to superconducting quantum interference device with superconducting wires. The temperature is in the range of 2 K to 400 K. For ferromagnetism, there are principal magnetic measurements: *M(H)* - magnetization as a function of applied magnetic field

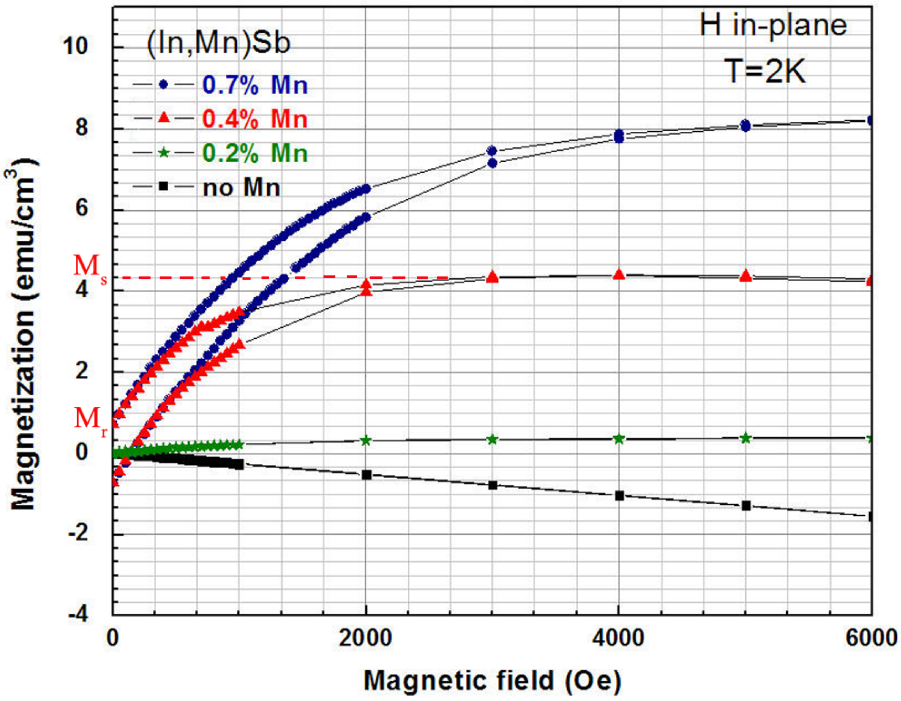

Figure 5.11: Hysteresis loops of (In,Mn)Sb films with different Mn contents measured at 2 K when the field applied parallel to layer plane.

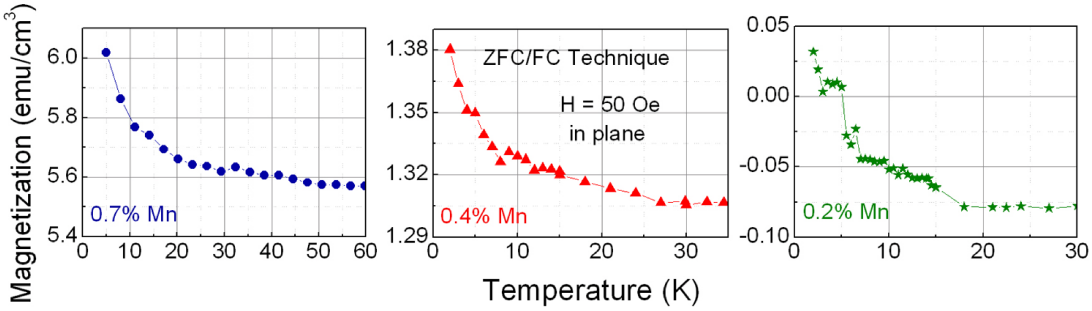

Figure 5.12: Temperature-dependent magnetization measured in a parallel field of 50 Oe, for the three $In_{1-x}Mn_xSb$ samples with $x = 0.7\%$, 0.4% and 0.2%. ZFC/FC means zero-field-cooled/field cooled. This is done by cooling the sample to the lowest measured temperature at $H = 0$. The ZFC part is measured as a function of temperature up to the highest desired temperature after a magnetic field is applied. By cooling the sample in this same field to the lowest temperature and measuring again as a function of temperature, the FC part can be done.

and *M(T)* - magnetization as a function of temperature. Figure 5.11 shows the field dependence of magnetization for four samples with different Mn content measured at 2 K,

when the magnetic field was applied parallel to the plane. For all (In,Mn)Sb samples, the *M(H)* is not linear and the behavior is not reversible. The lack of reversibility is named magnetic hysteresis loop. In these samples, the hysteresis loops in the low field range $H < 5000$ Oe are clearly seen, reflecting the ferromagnetic properties at low temperature of the diluted ferromagnetic materials. In comparison, magnetization measurements carried out on the sample without Mn have not shown any ferromagnetic characterizations. In the (In,Mn)Sb samples, as H increases the magnetization gradually reaches a maximum value as known as the saturation magnetization (which is denoted M_s in Fig. 5.11). The saturation magnetization of the films is also found to be dependent on Mn composition. The samples with the Mn content lower than 0.7% have the ferromagnetic contributions, which saturate in the low field region, while the ferromagnetic contribution of the sample with 0.7% reveals a slowly increasing component in the higher field region. As H is reduced back to zero from saturation, the magnetization goes to the value of remanent magnetization (as indicated M_r in Fig. 5.11). The measured values for remanent, and saturation magnetization of the films are found to be dependent on Mn composition. The remanence M_r of the sample with 0.7% Mn is approximately 17% of the saturation magnetization M_s, whereas samples with 0.4% and 0.2% Mn have M_r/M_s ratio of about 47% and 77%, respectively. While the saturation magnetization is an intrinsic property of the material, the remanent magnetization depends on the fabrication of the samples [191]. If the amplitude of the hysteresis loop is smaller than the saturation magnetization, one can conclude that not all the Mn moments participate in the hysteresis loop; there is a significant part of the Mn moments which requires higher field to align [172]. However, in my (In,Mn)Sb samples, the amplitude of the hysteresis loops are equal to the saturation magnetization, indicating that at very low temperature all the Mn moments participate in the low field hysteresis loop. In the sample with the highest Mn content of 0.7%, the magnetization saturates at $5000 \sim 6000$ Oe. This observation is then compared with the other in Fig. 5.10. In the range of $H < \sim 6000$ Oe, the *M(H)* curve corresponds to the magnetoresistance curve well. At higher field 6000 Oe $< H <$ 2 T, the anomalous Hall effect in the $R_{Hall}(H)$ is still observed, while the magnetization is saturated. This observation could result in some new effects due to electron scattering. However, the physics behind the process is needed to analyse. Figure 5.12 shows the temperature-dependent magnetization measured in a parallel field of 50 Oe, for the three $In_{1-x}Mn_xSb$ samples with $x = 0.7\%$, 0.4% and 0.2%. At low temperature, the magnetization decreases as decreasing temperature as well as the Mn content. It can be also seen that there is a magnetic phase change below 50 K, 30 K and 20 K for the sample with the Mn content of 0.7%, 0.4% and 0.2%, respectively. As discussed in section 5.4, these magnetic phase changes may originate from the ferromagnetic matrix. From these curves, Curie temperature T_c of the samples can be estimated [192; 193; 97; 96]. T_c is measured to be 50 ± 1 K, 27 ± 1 K, and 18 ± 1 K corresponding to Mn content of 0.7%, 0.4%, and 0.2%, respectively (discussed in section 5.5). The temperature-dependent magnetization of the $In_{1-x}Mn_xSb$ sample with $x = 0.7\%$ measured over the full temperature range at 500 Oe and 100 Oe is shown in Fig 5.13. The *M(T)* curves are evidently spaced, reflecting the higher applied field the higher magnetization. Moreover, both curves also reveal two distinct phases; one below about 50 K and the other above 50 K. As discussed

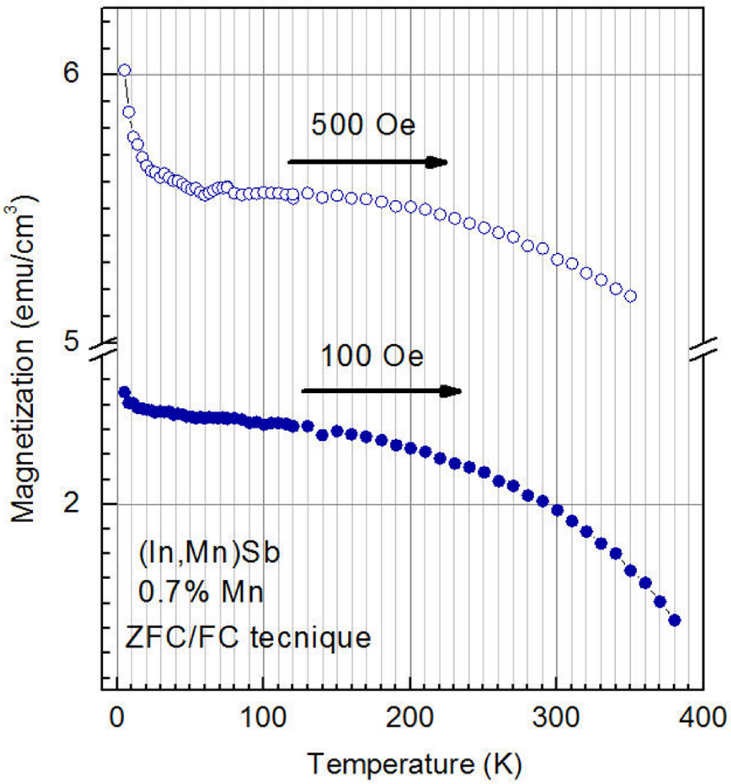

Figure 5.13: Temperature-dependent magnetization of the $In_{1-x}Mn_xSb$ sample with x = 0.7% measured at applied magnetic field of 500 Oe and 100 Oe.

above, the temperature of 50 K is expected to be the T_c of DMS (In,Mn)Sb alloy in this sample.

Magnetization versus magnetic field curves for the sample with x = 0.7% measured at 300 K, 77 K, and 2 K with the magnetic field H parallel to the sample plane are shown in Fig. 5.14. Magnetization measurements carried out on samples with other Mn compositions also exhibited similar behavior and hence are not shown here. Saturation in magnetization was found even at 300 K, which is a consequence of the ferromagnetic clusters being present in the film (see section 5.4 for details). The difference in the value of saturation magnetization between 2, 77, and 300 K suggests that the Mn contribution in magnetic phase InMnSb and much lower T_c [194].

5.5 Mn distribution

The AFM topographs of the four films, which are 5 μm × 5 μm scans, are shown in Fig. 5.15. The samples have well-interconnected surface features with average height of 30 nm; these features are basically independent of the Mn content. In addition, the AFM

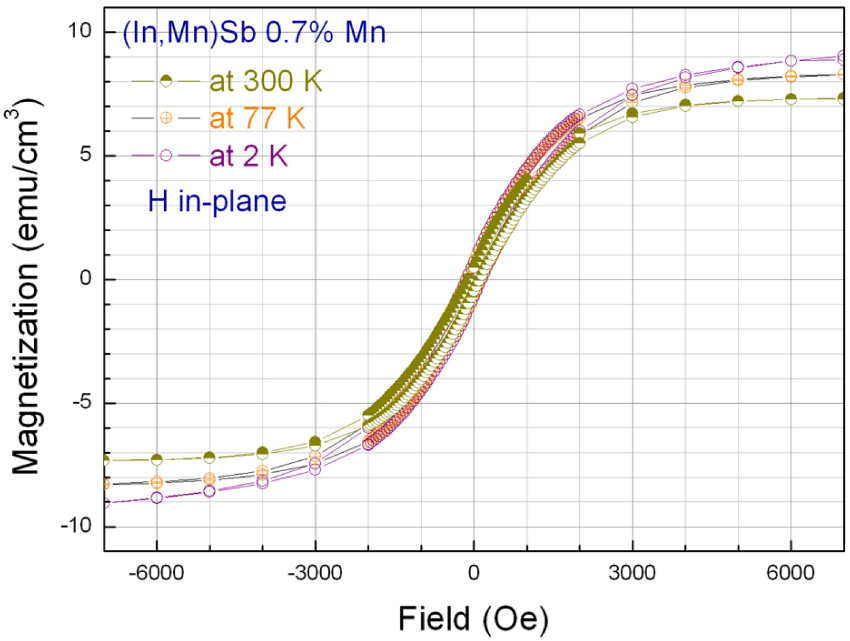

Figure 5.14: Magnetization curves of the $In_{1-x}Mn_xSb$ sample with $x = 0.7\%$ at three different temperatures. Magnetic field was applied parallel to the sample plane.

images reveal small triangular hillocks (as indicated with arrows) with base dimensions in the range of about 200 nm and average height of 120 nm. As the Mn content decreases, the density and size of these triangular hillocks decrease. In the sample with Mn content of 0.7%, the areal density of the triangular hillocks is found to be $4/\mu m^2$, decreasing to $1/\mu m^2$ in the sample with 0.2% Mn. One can note that the triangular hillocks are only observed in the samples with Mn; in the bulk InSb sample, no triangular hillocks are found. The presence of Mn in InSb can result in MnSb clusters [10; 101; 8] and I believe that the triangular hillocks are, in fact, such clusters, representing a second magnetic phase in the samples.

The JEOL JEM-3010 transmission electron microscopy (TEM) with high spatial resolution down to the atomic scale can quantitatively determine not only the surface, interface structure and morphology of as-grown nanostructured materials but also the local chemical composition by electron energy-loss spectroscopy (EELS) with nanometer probe size at the same position. Figure 5.15 shows cross-sectional TEM images of a sample with 0.4% Mn. Three layers with abrupt interfaces can be identified (Fig. 5.16(a)). The first layer from the bottom is the GaAs substrate. The second layer consists of (In,Mn)Sb alloy with a small density of defects, and the last layer is island-shape top layer due to the MnSb clusters. Fig. 5.16(b) depicts the diffraction pattern of the sample and is used to deduce the lattice parameters of the compounds. The bright spots represent the different compounds as marked in the figure. The existence of MnSb clus-

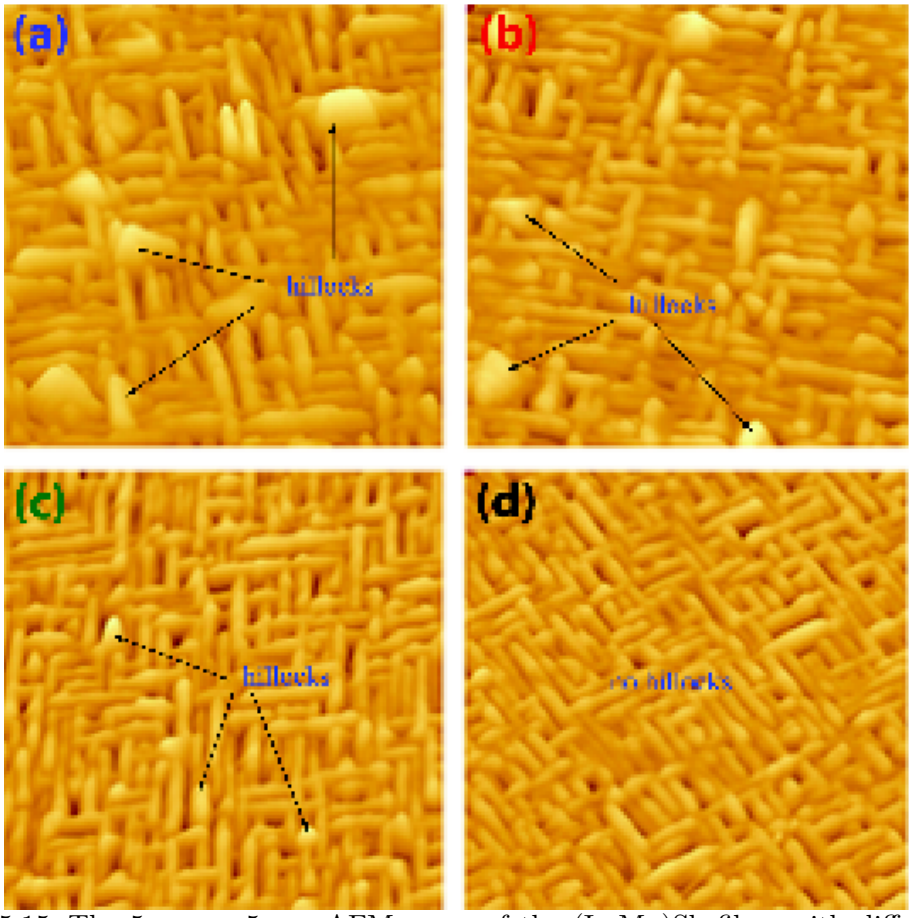

Figure 5.15: The 5 μm $\times$ 5 μm AFM scans of the (In,Mn)Sb films with different Mn content (a) 0.7%, (b) 0.4%, (c) 0.2%, and (d) 0.0%.

ters, which have a lattice constant between (In,Mn)Sb and GaAs, can be clearly seen. The cross-sectional TEM of the island clusters is shown in Fig. 5.16(c) and (d). The TEM results show that the MnSb clusters are not buried in the matrix, but located on the top layer. The height of the islands is about 20$\pm$2 nm. In order to explain the existence of MnSb nanoclusters on the top layer, at least two explanations have been proposed: First, MnSb has significant higher surface energies than that of (In,Mn)Sb [195]. Second, during the decreasing temperature under antimony flux after growth, it may happen that some residual Mn atoms in the growth chamber combined with Sb and formed MnSb islands on the surface.

The SEM micrographs of the film with 0.7% Mn as seen in Fig. 5.17 reveal the presence of a second phase (as indicated with arrows in black) on the surface. Compared with the AFM and TEM results, these features are assumed to be MnSb clusters. The clusters are of about 20-30 nm in dimension and distribute rather nonuniformly only on the surface. In addition, the image (Fig. 5.17 bottom) also shows other surface features (as indicated with arrows in yellow), of several μm in length, which do not appear in AFM or TEM

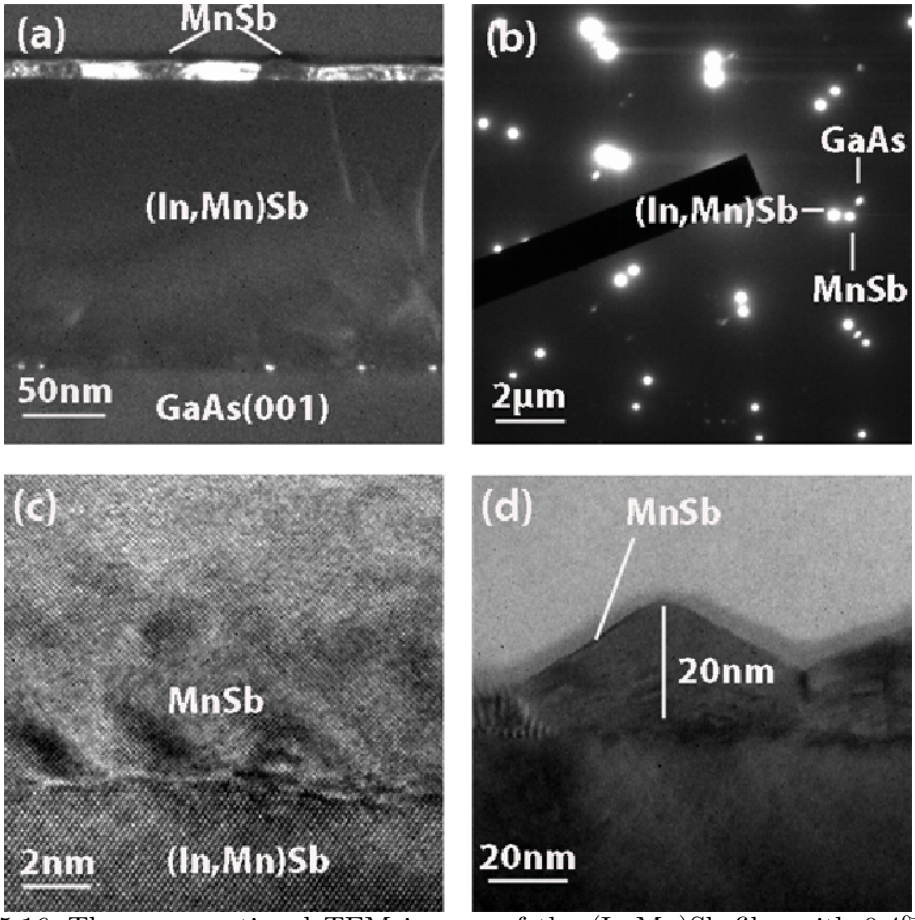

Figure 5.16: The cross-sectional TEM images of the (In,Mn)Sb film with 0.4%Mn (a) Overview of 50 nm sample, (b) Large area of 2 μm with shadow, (c) High-resolution image of top layer, and (d) MnSb with hight of 20 nm on the top.

images. These features are due to the cleaving.

Figure 5.18 shows the field dependence of magnetization for three samples at 2 K. Three distinguished hysteresis loops are observed in the magnetization measurement, suggesting the ferromagnetic properties at low temperature of the diluted ferromagnetic matrixes. The magnetization curves also show little difference between in-plane and out-of-plane field orientation. The diluted ferromagnetic matrix also results in an enhanced magnetoresistance response at low field and anomalous Hall effect at low temperature [9; 101]. The results show that the saturation magnetization of the films depends on Mn concentration. The magnetization saturates at higher field and has higher value for higher Mn content.

The magnetization versus external magnetic field was also carried out for the (In,Mn)-Sb samples at 300 K as shown in Fig. 5.19. All samples with Mn exhibit a ferromagnetic ordering at 300 K, displaying distinguished hysteresis loops. This observation indicates

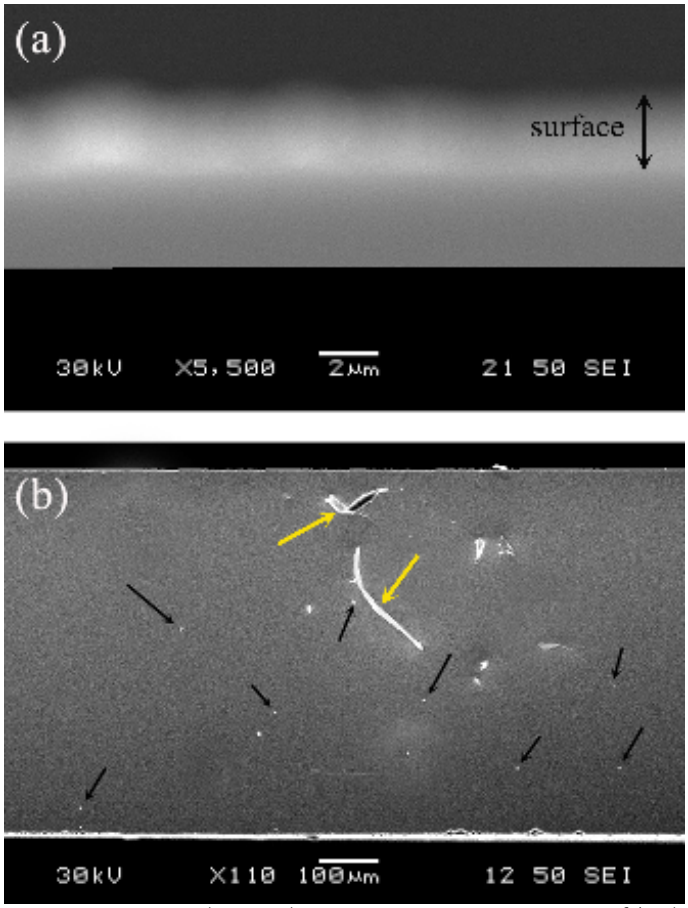

Figure 5.17: SEM images of the (In,Mn)Sb film Mn content of 0.7%. (a): cross-sectional view and (b): plan view.

that, in addition to the DMS (In,Mn)Sb due to substitutional Mn, a fraction of Mn also goes to MnSb clusters and contributes to the ferromagnetism (MnSb $T_C \sim 580$ K, the magnetic moment per Mn $\sim 3.5\mu_B$; μ_B: Bohr magneton [196]). The magnetization curves also showed little difference between in-plane and out-of-plane field orientation. However, the measured values for coercivity, remanent, and saturation magnetization of the films are found to be dependent on Mn composition. From the value of saturation magnetization, Matsukura *et al.* [194] reported that about 60% of the nominal Mn contributed to the formation of MnSb clusters in the (Ga,Mn)Sb sample with 8.6% Mn. The remaining 35% of Mn is in another phase. In our samples, the quantities of the Mn contribution are not clear. However, I found that as Mn density in the crystal increases, more MnSb clusters are formed. In comparison, magnetization measurements carried out on sample without Mn have not shown any ferromagnetic characterizations [197].

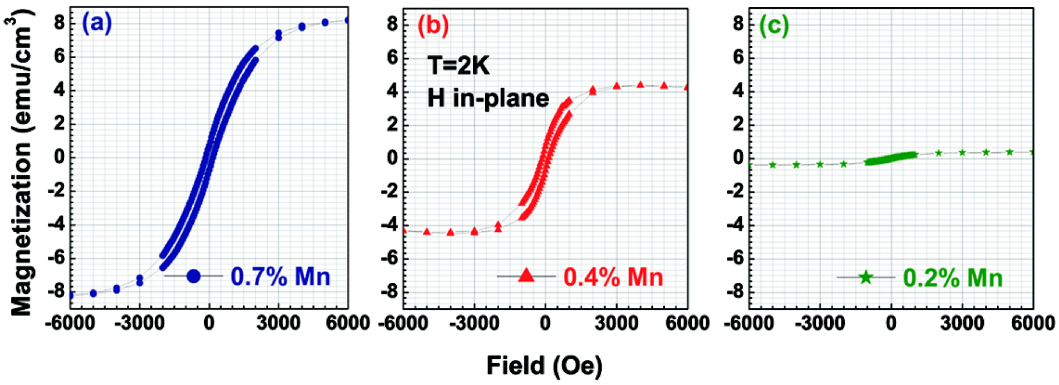

Figure 5.18: The experimental magnetic field dependence of magnetization with in-plane field at 2 K for three (In,Mn)Sb films with different Mn content of (a) 0.7%, (b) 0.4%, and (c) 0.2%.

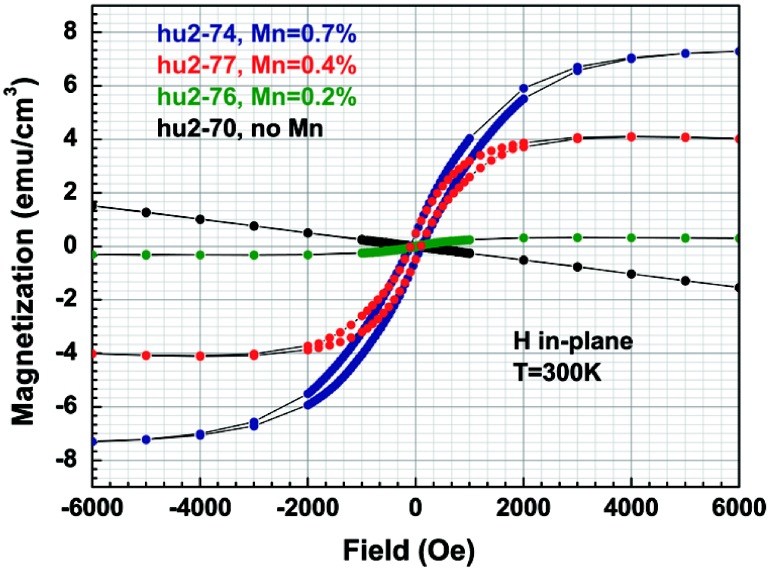

Figure 5.19: The M vs H plots at 300 K for four (In,Mn)Sb films with different Mn concentration when magnetic field applied parallel to the layer.

5.6 Curie temperature

Curie temperature T_c of a ferromagnetic material is the temperature above which the material loses its ferromagnetic characteristics. At temperature $T < T_C$, the magnetic

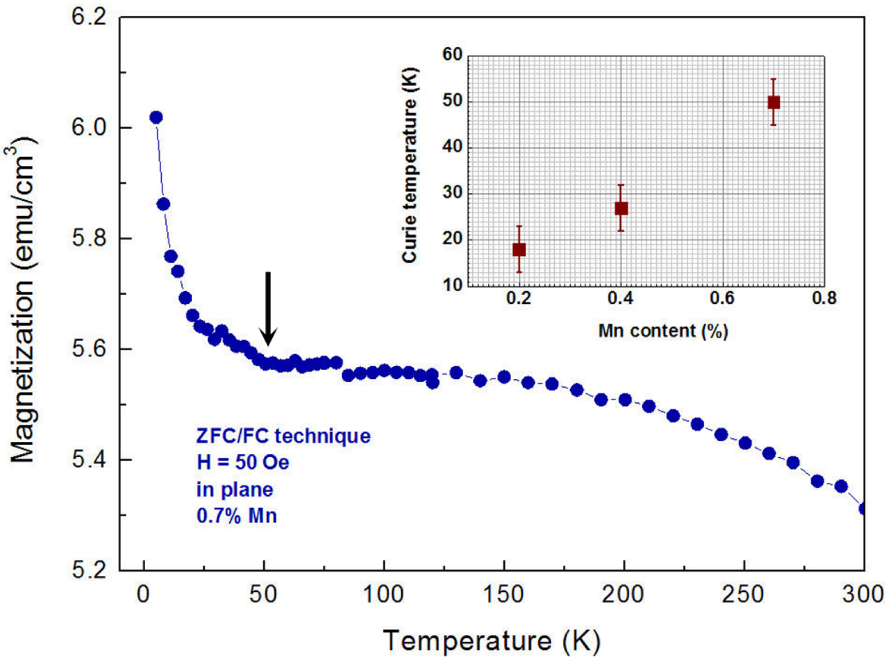

Figure 5.20: Temperature dependence of magnetization measured with in-plane field of 50 Oe for (In,Mn)Sb film with 0.7% Mn. Inset shows T_c as a function of Mn content.

moments are aligned within magnetic domains. As the temperature is increased towards T_c, the alignment (magnetization) within each domain decreases. Above T_c, the material is purely paramagnetic.

In the III-V ferromagnetic semiconductors, (Ga,Mn)As and (Ga,Mn)N are expected to possess the highest Curie temperature. For (In,Mn)Sb, Ganesan *at al.* [10] has recently reported the studies on bulk Mn-doped InSb materials grown by the horizontal Bridgman technique. It has been found that a ferromagnetic state below 10 K is the consequence of (In,Mn)Sb alloy and other ferromagnetic phase is contributed by MnSb clusters, that may provide $T_C \sim 580$ K [196]. The presence of such ferromagnetic clusters in these hybrid systems may be important for semiconductor-based spinphotonic applications and devices with a higher Curie temperature.

In our case, magnetization measurements also indicate that both the (In,Mn)Sb alloy as well as the MnSb inclusions are ferromagnetic and two distinct Curie temperatures are measured. Figure 5.20 shows the temperature dependence of magnetization of the sample with 0.7% Mn. It has been seen that two magnetic phases contribute to two separately parts of *M(T)* curve. One magnetic ordering below 50 K could arise from magnetic nature of the (In,Mn)Sb alloy, and other above 50 K should be from MnSb clusters. The temperature-dependent magnetization curves of samples with other Mn concentrations also exhibited similar behavior and hence are not shown here. Due to a limited temperature range by using SQUID to do magnetization measurements, the *M*

vs T plots should not be performed above 400 K. However, from other study, magnetic phase in MnSb clusters may have T_c above 500 K [10]. The junctional temperature (as indicated with arrow) between two magnetic phases have been widely used to estimate the T_c of DMS contribution [192; 193; 97; 96]. The inset shows the T_c versus Mn concentration for three DMS (In,Mn)Sb orderings. T_c is estimated to be 50 K, 27 K, and 18 K corresponding to Mn content of 0.7%, 0.4%, and 0.2%, respectively. Wojtowicz *et al.* [94] and Jungwirth *et al.* [181] reported a model to calculate T_c using a mean-field-theoretical (MFT) approach based on the 8-band effective band-orbital method (EBOM). This model estimates that T_c should increase roughly linearly with ferromagnetic Mn moment density. The theoretical calculations have been then compared with experimental values and an agreement between experiment and theory has been seen. In my (In,Mn)Sb samples, the T_c of DMS contribution also increases with increasing Mn content in the range studied here, as expected. It is known from studies of III-Mn-V [192; 46; 96] that a larger amount of magnetic impurity reduces T_c. In order to elucidate the mechanism responsible for the decrease of T_c when Mn content increases, at least two predictions have been proposed: the loss of substitution Mn to form MnSb clusters or to interstitial (double donor) sites and the formation of native defects such as Sb_{In} and In_{Sb} antisites. The result is a reduction in the density of active Mn spins, which in turn produces the drop of T_c. Note that my (In,Mn)Sb samples may have MnSb clusters or interstitial sites as well as native defects such as Sb_{In} and In_{Sb} antisites, which would be known to compensate carriers. The carrier concentration of the films at 300 K is obtained to be 7.4e19 cm^{-3}, 1.8e19 cm^{-3}, and 5.4e18 cm^{-3} for sample with the Mn content of 0.7%, 0.4%, and 0.2%, respectively. At 15 K, the corresponding carrier concentration decreases to be 4e19 cm^{-3}, 1.2e19 cm^{-3}, and 4.6e18 cm^{-3}. However, in our (In,Mn)Sb samples, the T_c of DMS contribution also increases with increasing Mn content in the range studied here. It seems that the Mn moment compensation does not play an important role in the hole-mediated ferromagnetism in the given range of Mn composition [100]. But the origins behind the process remain unclear.

5.7 Improvement for achieving higher Curie temperature

As discussed above, investigates samples show two ferromagnetic components: one from the DMS (In,Mn)Sb alloy and the other from the ferromagnetic MnSb clusters. The former reveals the Curie temperature T_c below 50 K. For the materials to be useful in device applications, at least two things are required: the higher T_c and the defect reduction. In order to obtain a higher T_c, it is crucial to increase the hole concentration by adding a large amount of Mn into the III-V host material. Because when Mn atom occupies substitutional group-III position, it acts as an acceptor. Hence, it supplies a local moment as well as a free hole for conduction. Ferromagnetic ordering in these structures is widely accepted to be due to the coupling between Mn local moments mediated by holes in the valence band. My investigation indicates that the T_c is proportional to the

magnetic moment, that depends upon the density of substitutional Mn ions; as the density of substitutional Mn ions increases the T_c increases. This trend has been confirmed experimentally in other previous works [7; 101; 8], even though the Mn contents in these samples (2 - 10%) are higher than those in my samples, but the T_c is lower. There are two ways to achieve higher T_c:

- Using higher Mn concentration.

- Since my results indicate that the more Mn was added, the more MnSb clusters were formed. However, these clusters dominate only on the surface. Hence, the second possibility is to etch the films down to several ten nanometers from the surface, where the cluster are located. Wojtowicz *et al.* [96] reported that Mn ions occupying interstitial sites (M_I) as double donors compensate the substitutional Mn (M_s) acceptors, therefore reducing the hole concentration and lowering the T_c of the $III_{1-x}Mn_xV$ alloys. According to this study, the M_I can be evidently removed via low-temperature annealing, while annealing at higher temperature is found to move a large fraction of Mn from substitutional positions to random clusters, hence decreasing both the number of active spins and the number of holes, and thus lowering T_c. For other III-V DMS, (Ga,Mn)As, Wang *et al.* [193] also reported that the T_c depends sensitively on the post growth annealing procedures. Taking all these concerns together, it is interesting to carry out further researches to obtain the higher Curie temperature.

5.8 Summary

To conclude, I have investigated the growth, structural, magnetotransport, and magnetic properties of the ferromagnetic $In_{1-x}Mn_xSb$ crystals grown on GaAs (001) using MBE. The Mn content is determined to be smaller than 1%.

The lattice studies show no variance of lattice constants between the magnetic layers $In_{1-x}Mn_xSb$ and the InSb buffer layers in each sample. The perpendicular lattice constant $a_\perp$ of the epilayers decreases with increase Mn content. The reason may be the interstitial Mn Mn_I and Sb antisites Sb_{In} defects. The in-plane lattice constant $a_\parallel$ is smaller than the lattice parameter perpendicular to the layer plane $a_\perp$ for each sample. It is seen that the epilayers remain strain-relaxed to the GaAs substrate. The values of relaxed layer lattice parameter a_{relax} and the degree of strain m are also calculated from the measured values of $a_\perp$ and $a_\parallel$. Mn decreases the lattice constant as well as the degree of relaxation of (In,Mn)Sb films. In all samples, the XRD measurements showed high crystalline perfection of the $In_{1-x}Mn_xSb$ layers.

The electrical measurements reveal a negative magnetoresistance and anomalous Hall effect below 5 K. The occurrence of the negative magnetoresistance has been analyzed using the Anderson localization. The increasing Mn concentration increases the carrier concentration but decreases resistivity. The carrier concentration at low temperatures (below 50 K) indicates the impurities (scatterers). The AHE was observed at 4.2 K in the low field region, establishing the ferromagnetism of the material. One can suppose

that only some of the total Mn spins appear to contribute the hysteresis loop at the low field. Some part of the others may be buried in the depletion layer region, which require much higher field to align and may coexist with the ferromagnetic clusters in the interior of the (In,Mn)Sb layer. The shape of the hysteresis loop is also suggested to depend on the magnetic anisotropy.

The distribution of Mn in the (In,Mn)Sb films has been discussed. TEM, AFM, SEM, x-ray and magnetization studies show two magnetic states in the (In,Mn)Sb films with different Mn content, corresponding to diluted magnetic semiconductor (In,Mn)Sb and clusters MnSb. A fraction of Mn atoms also goes to interstitial sites and to be electrically compensated, as revealed by Hall measurements. The measured values of T_c are found to be highly dependent on Mn concentration. In general, the Curie temperature in the diluted magnetic phase (In,Mn)Sb and in other magnetic phase of clusters has been found to be below 50 K and above 300 K, respectively. The observations of two magnetic states in the crystals and high T_c of MnSb clusters could be important for realizing ferromagnetic semiconductor based devices.

6 Conclusion and outlook

Taking the advantage of the high electron mobility as a key parameter for device applications such as infrared detectors, and Hall devices, InSb generates much interest. On the progress, the diluted magnetic semiconductor based InSb is also providing an exciting field of research, in particular with respect to how to achieve high Curie temperature. My dissertation, therefore, focuses on the growth and characterization of two main systems: InSb semiconductor and (In,Mn)Sb diluted magnetic semiconductor. All investigated heterostructures were grown using MBE Riber Compact 21T. For characterization, reflection high energy electron diffraction, x-ray diffraction, atomic force microscopy, scanning electron microscopy, transmission electron microscopy, superconducting quantum interference device as well as optical and transport techniques were applied.

Due to the large lattice mismatch between the epi-layer and substrate, the successful growth of InSb on GaAs (14.6% lattice mismatch) and on Si (19.3% lattice mismatch) is a challenge. For the hybrid semiconductor device applications, thin epitaxial layers of high-mobility InSb are required. Even though some related papers have reported the electron mobility at 300 K of the 2μm-thick InSb epilayer as high as 43000 cm^2/Vs (grown with buffer layer) [143] or 55000 cm^2/Vs (grown with a imperial recipe) [198], my study comprises a novel finding that high-quality InSb films can be grown directly without any special technique on (001) GaAs substrate with the electron mobility as high as 41100 cm^2/Vs at 300 K, corresponding to the carrier concentration of about 2.9e16 cm^{-3}. However, the electron mobility degradation and the carrier freeze-out at low temperatures were observed. To reduce these factors, the sample was doped by Si with the doping level of 2e16 cm^{-3}. The high mobility measured at low temperatures strongly inspires to grow the thicker InSb layers for the fabrication of infrared detectors [199; 200]. (An example structure of a p-i-n photodetector is shown in Fig. 6.1) The optimal growth parameters include the substrate temperature of 310^{o}C, the Sb/In flux ratio of 5.6, and the growth rate of 2 Å/s for the InSb/GaAs growth.

The growth of InSb/Si is more challenging. The difficulties involved in growth of high quality InSb films on Si include not only the large lattice mismatch but also the different thermal expansion coefficients ($\alpha_{InSb} \approx 2\alpha_{Si}$ at 300 K) and antiphase domain formation due to the growth of anpolar semiconductor on a nonpolar semiconductor. Only few related studies have been published so far [1; 2; 3]. For the successful growth of InSb/Si, I had to use Si (001) offcut by 4^o toward (110) substrate and the insertion of buffer layers, which help to reduce the lattice mismatch as well as the formation of defects. The 300 K mobility of 24000 cm^2/Vs corresponding to a carrier concentration of 2.6e16

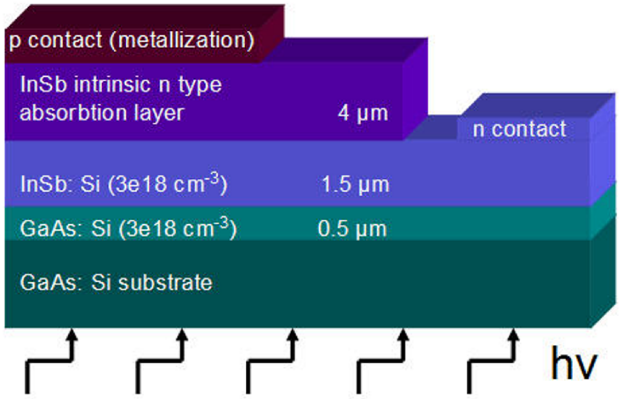

Figure 6.1: Schematic structure of a p-i-n photodetector.

cm^{-3} is found for the best 2μm-thick sample, which is grown at 340^oC with GaSb/AlSb superlattice buffer layer.

On (In,Mn)Sb material system, I have investigated the growth, structural, magnetotransport, and magnetic properties of ferromagnetic $In_{1-x}Mn_xSb$ ($x < 1\%$) crystals grown on GaAs (001). The samples reveal two magnetic phases, corresponding to the diluted magnetic semiconductor (In,Mn)Sb alloy and clusters MnSb. The distribution of the clusters is only on the sample surface. The measured values of the Curie temperature T_c are found to be highly dependent on Mn concentration. In our samples, the Curie temperature in the diluted magnetic phase (In,Mn)Sb alloy and in other magnetic phase of clusters has been found to be below 50 K and above 300 K, respectively. The high T_c obtained (∼50 K) with very low Mn doping range $< 1\%$ (compared with other previous researches [7; 101; 8]) provides a possibility to achieve higher T_c if I add a larger amount of Mn into the samples. The reason is that if more Mn atoms are added, more local moments are supplied. My experiments show a proportional correlation between the T_c and the magnetic moment. My results also show that the more Mn atoms were added, the more MnSb clusters were formed. However, these clusters dominate only on the sample surface. Hence, it is a new idea to etch the films down to several ten nanometers from the surface, where the clusters dominate. By this way, the MnSb clusters are then removed and the research can be carried out only on the DMS (In,Mn)Sb alloy. Other interesting work is low-temperature annealing to remove the Mn interstitial sites (M_I) which reduce the hole concentration hence, result lower T_c [96]. Altogether, I expect that it is possible to bring this material closer to the applications for realizing ferromagnetic semiconductor based devices.

Bibliography

[1] J. I. Chyi, D. Biswas, S. V. Iyer, N. S. Kumar, H. Morkoc, R. Bean, K. Zanio, H. Y. Lee, and H. Chen. Molecular beam epitaxial growth and characterization of InSb on Si. *Applied Physics Letters*, 54:1016, 1989.

[2] S. V. Ivanov, A. A. Boudza, R. N. Kutt, N. N. Ledentsov, B. Y. Meltser, S. S. Ruvimov, S. V. Shaposhnikov, and P. S. Kopev. Molecular beam epitaxial growth of InSb/GaAs (100) and InSb/Si (100) heteroepitaxial layers (thermodynamic analysis and characterization). *Journal of Crystal Growth*, 156(3):191–205, 1995.

[3] H. C. Lu, H. R. Fetterman, C. J. Chen, C. Hsu, and T. M. Chen. Growth and characterization of MBE-grown thin films of InSb on Si. *Solid-State Electronics*, 36(4):533–538, 1993.

[4] W. K. Liu, J. Winesett, W. Ma, X. Zhang, M. B. Santos, X. M. Fang, and P. J. McCann. Molecular beam epitaxy of InSb on Si substrates using fluoride buffer layers. *Journal of Applied Physics*, 81:1708, 1997.

[5] D. M. Li, M. Atoji, M. Yamazaki, T. Okamoto, T. Tambo, and C. Tatsuyama. The role of (4x3) surface reconstruction induced by in adsorption for the heteroepitaxial growth of InSb on Si (001)-2x1 surface. *Applied Surface Science*, 130:101–106, 1998.

[6] M. Mori, N. Akae, K. Uotani, N. Fujimoto, T. Tambo, and C. Tatsuyama. Heteroepitaxial growth of InSb films on a Si (001) substrate via AlSb buffer layer. *Applied Surface Science*, 216(1-4):569–574, 2003.

[7] T. Wojtowicz, G. Cywinski, W. L. Lim, X. Liu, M. Dobrowolska, J. K. Furdyna, W. Yu, K. M .and Walukiewicz, G. B. Kim, M. Cheon, et al. $In_{1-x}Mn_xSb$ - a narrow-gap ferromagnetic semiconductor. *Applied Physics Letters*, 82:4310, 2003.

[8] S. Yanagi, K. Kuga, T. Slupinski, and H. Munekata. Carrier-induced ferromagnetic order in the narrow gap III-V magnetic alloy semiconductor (In,Mn)Sb. *Physica E: Low-Dimensional Systems and Nanostructures*, 20(3-4):333–337, 2004.

[9] L. Tran, F. Hatami, W. T. Masselink, V. P. Kunets, and G. J. Salamo. Comparison of MBE growth of InSb on Si (001) and GaAs (001). *Journal of Electronic Materials*, 37(12):1799–1805, 2008.

[10] K. Ganesan and H. L. Bhat. Growth, magnetotransport, and magnetic properties of ferromagnetic (In,Mn)Sb crystals. *Journal of Applied Physics*, 103:043701, 2008.

[11] J. S. Blakemore. *Solid State Physics*. Cambridge University Press, 1985.

[12] M. Levinshtein, S. Rumyantsev, and M. Shur. *Handbook series on Semiconductor parameters*. World Scientific Publishing Company, 1996.

[13] O. Bierwagen. *Growth and anisotropic transport properties of self-assemble InAs nanostructures in InP*. PhD thesis, Humbold-Universitaet zu Berlin, 2008.

[14] I. Kimukin, N. Biyikli, T. Kartaloglu, O. Aytur, and E. Ozbay. High-speed InSb photodetectors on GaAs for mid-IR applications. *IEEE Journal of Selected Topics in Quantum Electronics*, 10(4):766–770, 2004.

[15] E. Michel and J. D. Kim. InSb infrared photodetectors on Si substrates grown by molecular beam epitaxy. *IEEE Photonics Technology Letters*, 8(5):673, 1996.

[16] G. Singh, E. Michel, C. Jelen, S. Slivken, J. Xu, P. Bove, I. Ferguson, and M. Razeghi. Molecular-beam epitaxial growth of high quality InSb for p-i-n photodetectors. *Journal of Vacuum Science & Technology B: Microelectronics and Nanometer Structures*, 13(2):782–785, 1995.

[17] K. Togawa, H. Sanbonsugi, A. Lapicki, M. Abe, H. Handa, and A. Sandhu. High-sensitivity InSb thin-film micro-Hall sensor arrays for simultaneous multiple detection of magnetic beads for biomedical applications. *IEEE Transactions on Magnetics*, 41(10):3661, 2005.

[18] A. Sandhu, H. Masuda, A. Oral, S. Bending, et al. Room temperature magnetic imaging of magnetic storage media and garnet epilayers in the presence of external magnetic fields using a sub-micron GaAs SHPM. *Journal of Crystal Growth*, 227: 899–905, 2001.

[19] G. Boero, M. Demierre, P. Besse, et al. Micro-Hall devices: performance, technologies and applications. *Sensors and Actuators A: Physical*, 106(1-3):314–320, 2003.

[20] Y. Sugiyama, Y. Takeuchi, and M. Tacanot. Highly-sensitive InGaAs-2DEG Hall device made of pseudomorphic $In_{0.52}Al_{0.48}As/In_{0.8}Ga_{0.2}As$ heterostructure. *Sensors and Actuators A: Physical*, 34(2):131–136, 1992.

[21] J. Dobbert, V. P. Kunets, T. A. Morgan, D. Guzun, Y. I. Mazur, W. T. Masselink, and G. J. Salamo. Strained quantum well InAs Micro-Hall sensors: Dependence of device performance on channel thickness. *IEEE Transactions on Electron Devices*, 55(2):695–700, 2008.

[22] A. J. Bosch, R. G. van Welzenis, and O. F. Z. Schannen. Molecular beam epitaxy of InSb (110). *Journal of applied physics*, 58(9):3434–3439, 1985.

[23] J. E. Oh, P. K. Bhattacharya, Y. C. Chen, and S. Tsukamoto. Molecular-beam epitaxial growth of high-quality InSb on InP and GaAs substrates. *Journal of Applied Physics*, 66(8):3618–3621, 1989.

[24] S. D. Parker, R. L. Williams, R. Droopad, R. A. Stradling, K. W. J. Barnham, S. N. Holmes, J. Laverty, C. C. Phillips, E. Skuras, R. Thomas, et al. Observation and control of the amphoteric behaviour of Si-doped InSb grown on GaAs by MBE. *Semiconductor Science and Technology*, 4:663, 1989.

[25] P. E. Thompson, J. L. Davis, J. Waterman, R. J. Wagner, D. Gammon, D. K. Gaskill, and R. Stahlbush. Use of atomic layer epitaxy buffer for the growth of lnSb dn GaAs by molecular beam epitaxy. *Journal of Applied Physics*, 69:10, 1991.

[26] P. Songpongs, T. G. Andersson, M. J. Ekenstedt, J. R. Soederstroem, and M. M. Cumming. Hall measurements on selectively doped InSb heterostructures grown by molecular beam epitaxy on GaAs (001). *Applied Physics Letters*, 65:1433, 1994.

[27] T. Sato, M. Akabori, and S. Yamada. High-quality highly mismatched InSb films grown on GaAs substrate via thick AlSb and $In_xAl_{1-x}Sb$ step-graded buffers. *Physica E: Low-dimensional Systems and Nanostructures*, 21:615–619, 2004.

[28] M. C. Debnath, T. Zhang, C. Roberts, L. F. Cohen, and R. A. Stradling. High-mobility InSb thin films on GaAs (001) substrate grown by the two-step growth process. *Journal of Crystal Growth*, 267(1-2):17–21, 2004.

[29] J. I. Chyi, S. Kalem, N. S. Kumar, C. W. Litton, and H. Morkoc. Growth of InSb and $InAs_{1-x}Sb_x$ on GaAs by molecular beam epitaxy. *Applied Physics Letters*, 53 (12):1092–1094, 2009.

[30] B. V. Rao, D. Gruznev, T. Tambo, and C. Tatsuyama. Growth of high-quality InSb films on Si (111) substrates without buffer layers. *Journal of Crystal Growth*, 224:316–322, 2001.

[31] M. Mori, M. Saito, K. Nagashima, K. Ueda, T. Yoshida, and K. Maezawa. High-temperature growth of heteroepitaxial InSb films on Si (111) substrate via the InSb bi-layer. *Journal of Crystal Growth*, 311(7):1692–1695, 2009.

[32] L. Tran, J. Dobbert, F. Hatami, and W. T. Masselink. Growth and characterization of InSb films on Si (001). *Materials Research Society*, Symp. Proc. 1068:C02–05, 2008.

[33] J. Dobbert, L. Tran, F. Hatami, WT Masselink, V.P. Kunets, and GJ Salamo. Low frequency noise in InSb/GaAs and InSb/Si channels. *Applied Physics Letters*, 97:102101, 2010.

[34] J. Dobbert, L. Tran, F. Hatami, WT Masselink, V.P. Kunets, and GJ Salamo. Deep level noise spectroscopy in InSb/GaAs and InSb/Si channels. submitted to Applied Physics Letters, 2010, 2010.

[35] J. Dobbert, L. Tran, F. Hatami, W. T. Masselink, V. P. Kunets, and G. J. Salamo. A comparison of the low frequency noise in InSb grown on GaAs and Si by MBE. *Journal of Crystal Growth*, doi:10.1016/j.jcrysgro.2010.12.039, 2010.

[36] F. Matsukura, H. Ohno, and T. Dietl. *Handbook of magnetic materials*. Elsevier, 2002.

[37] A. Haury, A. Wasiela, A. Arnoult, J. Cibert, S. Tatarenko, T. Dietl, and Y. Merle dAubigne. Observation of a ferromagnetic transition induced by two-dimensional hole gas in modulation-doped CdMnTe quantum wells. *Phys. Rev. Lett.*, 79(3):511–514, Jul 1997. doi: 10.1103/PhysRevLett.79.511.

[38] T. Jungwirth, J. Sinova, J. Masek, J. Kucera, and A. H. MacDonald. Theory of ferromagnetic (III,Mn)V semiconductors. *Reviews of Modern Physics*, 78(3): 809–864, 2006.

[39] N. W. Ashcroft and N. D. Mermin. *Solid State Physics*. Saunders College Publishing, Philadelphia, 1976.

[40] P. W. Anderson. Antiferromagnetism. theory of superexchange interaction. *Physical Review*, 79(2):350–356, 1950.

[41] C. Zener. Interaction between the d shells in the transition metals. *Phys. Rev.*, 81 (3):440–444, Feb 1951. doi: 10.1103/PhysRev.81.440.

[42] C. Zener. Interaction between the d-Shells in the transition metals. II. ferromagnetic compounds of manganese with Perovskite structure. *Phys. Rev.*, 82(3): 403–405, May 1951. doi: 10.1103/PhysRev.82.403.

[43] A. K. Bhattacharjee, G. Fishman, and B. Coqblin. Virtual bound state model for the exchange interaction in semimagnetic semiconductors such as $Cd_{1-x}Mn_xTe$. *Physica B+ C*, 117:449–451, 1983.

[44] T. Dietl. *Handbook of Semiconductors*. North Holland, Amsterdam, 1994.

[45] I. C. Gummich et al. Interaction between two magnetic impurities in a quantum well. *Solid state communications*, 76(6):831–833, 1990.

[46] F. Matsukura, H. Ohno, A. Shen, and Y. Sugawara. Transport properties and origin of ferromagnetism in (Ga,Mn)As. *Physical Review B*, 57(4):2037–2040, 1998.

[47] J. De Boeck, R. Oesterholt, A. Van Esch, H. Bender, C. Bruynseraede, C. Van Hoof, and G. Borghs. Nanometer-scale magnetic MnAs particles in GaAs grown by molecular beam epitaxy. *Applied Physics Letters*, 68:2744, 1996.

[48] H. Shimizu, T. Hayashi, T. Nishinaga, and M. Tanaka. Magnetic and transport properties of III-V based magnetic semiconductor (GaMn)As: Growth condition dependence. *Applied Physics Letters*, 74:398, 1999.

[49] G. M. Schott, W. Faschinger, and L. W. Molenkamp. Lattice constant variation and complex formation in zincblende gallium manganese arsenide. *Applied Physics Letters*, 79:1807, 2001.

[50] D. C. Look. On compensation and conductivity models for molecular-beam-epitaxial GaAs grown at low temperature. *Journal of Applied Physics*, 70:3148, 1991.

[51] M. Luysberg, H. Sohn, A. Prasad, P. Specht, Z. Liliental-Weber, E. R. Weber, J. Gebauer, and R. Krause-Rehberg. Effects of the growth temperature and As/Ga flux ratio on the incorporation of excess As into low temperature grown GaAs. *Journal of Applied Physics*, 83:561, 1998.

[52] K. Takamura, F. Matsukura, Y. Ohno, and H. Ohno. Growth and properties of (Ga,Mn)As films with high Mn concentration. *Journal of Applied Physics*, 89: 7024, 2001.

[53] A. Shen, H. Ohno, F. Matsukura, Y. Sugawara, N. Akiba, T. Kuroiwa, A. Oiwa, A. Endo, S. Katsumoto, and Y. Iye. Epitaxy of (Ga,Mn)As, a new diluted magnetic semiconductor based on GaAs. *Journal of Crystal Growth*, 175:1069–1074, 1997.

[54] A. Shen, Y. Horikoshi, H. Ohno, and S. P. Guo. Reflection high-energy electron diffraction oscillations during growth of GaAs at low temperatures under high As overpressure. *Applied Physics Letters*, 71:1540, 1997.

[55] S. P. Guo, A. Shen, H. Yasuda, Y. Ohno, F. Matsukura, and H. Ohno. Surfactant effect of Mn on the formation of self-organized InAs nanostructures. *Journal of Crystal Growth*, 208(1-4):799–803, 2000.

[56] M. Tazima, K. Yamamoto, D. Okazawa, A. Nagashima, and J. Yoshino. Effect of Mn on the low temperature growth of GaAs and GaMnAs. *Physica E: Low-dimensional Systems and Nanostructures*, 10(1-3):186–191, 2001.

[57] H. Ohno, N. Akiba, F. Matsukura, A. Shen, K. Ohtani, and Y. Ohno. Spontaneous splitting of ferromagnetic (Ga,Mn)As valence band observed by resonant tunneling spectroscopy. *Applied Physics Letters*, 73:363, 1998.

[58] A. Shen, F. Matsukura, S. P. Guo, Y. Sugawara, H. Ohno, M. Tani, H. Abe, and H. C. Liu. Low-temperature molecular beam epitaxial growth of GaAs and (Ga, Mn) As. *Journal of Crystal Growth*, 201:679–683, 1999.

[59] J. Sadowski, R. Mathieu, P. Svedlindh, J. Z. Domagala, J. Bak-Misiuk, K. Swiatek, M. Karlsteen, J. Kanski, L. Ilver, H. Asklund, et al. Structural and magnetic properties of GaMnAs layers with high Mn-content grown by migration-enhanced epitaxy on GaAs (100) substrates. *Applied Physics Letters*, 78:3271, 2001.

[60] J. Sadowski, R. Mathieu, P. Svedlindh, M. Karlsteen, J. Kanski, L. Ilver, H. Asklund, K. Swiatek, J. Z. Domagala, J. Bak-Misiuk, and D. Maude. Properties of GaMnAs layers grown by migration enhanced epitaxy at very low substrate temperatures. *Physica E*, 10:181–185, 2001.

[61] J. Yang, H. Yasuda, S. Wang, F. Matsukura, Y. Ohno, and H. Ohno. Surface morphologies of III-V based magnetic semiconductor (Ga,Mn)As grown by molecular beam epitaxy. *Applied Surface Science*, 166(1-4):242–246, 2000.

[62] T. Hayashi, Y. Hashimoto, S. Katsumoto, and Y. Iye. Effect of low-temperature annealing on transport and magnetism of diluted magnetic semiconductor (Ga,Mn)As. *Applied Physics Letters*, 78:1691, 2001.

[63] S. J. Potashnik, K. C. Ku, S. H. Chun, J. J. Berry, N. Samarth, and P. Schiffer. Effects of annealing time on defect-controlled ferromagnetism in $Ga_{1-x}Mn_xAs$. *Applied Physics Letters*, 79:1495, 2001.

[64] Y. Satoh, D. Okazawa, A. Nagashima, and J. Yoshino. Carrier concentration dependence of electronic and magnetic properties of Sn-doped GaMnAs. *Physica E: Low-dimensional Systems and Nanostructures*, 10(1-3):196–200, 2001.

[65] R. K. Kawakami, E. Johnston-Halperin, L. F. Chen, M. Hanson, N. Guebels, J. S. Speck, A. C. Gossard, and D. D. Awschalom. (Ga,Mn)As as a digital ferromagnetic heterostructure. *Applied Physics Letters*, 77:2379, 2000.

[66] T. Omiya, F. Matsukura, A. Shen, Y. Ohno, and H. Ohno. Magnetotransport properties of (Ga,Mn)As grown on GaAs (411) A substrates. *Physica E: Low-dimensional Systems and Nanostructures*, 10(1-3):206–209, 2001.

[67] Y. J. Zhao, W. T. Geng, K. T. Park, and A. J. Freeman. Electronic and magnetic properties of $Ga_{1-x}Mn_xAs$: Role of Mn defect bands. *Phys. Rev. B*, 64(3):035207, Jun 2001. doi: 10.1103/PhysRevB.64.035207.

[68] S. Ohya, H. Shimizu, Y. Higo, J. Sun, and M. Tanaka. Growth and properties of quaternary alloy magnetic semiconductor (InGaMn)As. *Japanese Journal of Applied Physics*, 41:L24, 2001.

[69] T. Slupinski, H. Munekata, and A. Oiwa. Ferromagnetic semiconductor (In,Ga,Mn)As with Curie temperature above 100 K. *Applied Physics Letters*, 80: 1592, 2002.

[70] H. Munekata, H. Ohno, S. Von Molnar, A. Harwit, A. Segmueller, and L. L. Chang. Epitaxy of III-V diluted magnetic semiconductor materials. *Journal of Vacuum Science and Technology B: Microelectronics and Nanometer Structures*, 8:176, 1990.

[71] H. Ohno, H. Munekata, T. Penney, S. von Molnár, and L. L. Chang. Magnetotransport properties of p-type (In,Mn)As diluted magnetic III-V semiconductors. *Phys. Rev. Lett.*, 68(17):2664–2667, Apr 1992. doi: 10.1103/PhysRevLett.68.2664.

[72] H. Munekata, H. Ohno, R. R. Ruf, R. J. Gambino, and L. L. Chang. P-type diluted magnetic III-V semiconductors. *Journal of Crystal Growth*, 111(1-4):1011–1015, 1991.

[73] H. Ohno, H. Munekata, S. Von Molnar, and L. L. Chang. New III-V diluted magnetic semiconductors. *Journal of Applied Physics*, 69:6103, 1991.

[74] S. Guha and H. Munekata. Microstructure and homogeneity in (In,Mn)As III-V-based diluted magnetic semiconductor epitaxial films. *Journal of Applied Physics*, 74:2974, 1993.

[75] S. P. Guo, H. Ohno, A. Shen, F. Matsukura, and Y. Ohno. Self-organized (In,Mn)As diluted magnetic semiconductor nanostructures on GaAs substrates. *Applied Surface Science*, 130:797–802, 1998.

[76] S. P. Guo, A. Shen, F. Matsukura, Y. Ohno, and H. Ohno. InAs and (In,Mn)As nanostructures grown on GaAs (100), (211) B, and (311) B substrates. *Journal of Crystal Growth*, 201:684–688, 1999.

[77] H. Munekata, T. Penney, and L. L. Chang. Diluted magnetic III-V semiconductor structures. *Surface Science*, 267(1-3):342–348, 1992.

[78] A. Shen, F. Matsukura, Y. Sugawara, T. Kuroiwa, H. Ohno, A. Oiwa, A. Endo, S. Katsumoto, and Y. Iye. Epitaxy and properties of InMnAs/AlGaSb diluted magnetic III-V semiconductor heterostructures. *Applied Surface Science*, 113:183–188, 1997.

[79] H. Munekata, A. Zaslavsky, P. Fumagalli, and R. J. Gambino. Preparation of (In,Mn)As/(Ga,Al)Sb magnetic semiconductor heterostructures and their ferromagnetic characteristics. *Applied Physics Letters*, 63:2929, 1993.

[80] W Gebicki, J Strzeszewski, G Kamler, T Szyszko, and S. Podsiado. Raman scattering study of $Ga_{1-x}Mn_xN$ crystals. *Applied Physics Letters*, 76:3870, 2000.

[81] M. Zajac, R. Doradzinski, J. Gosk, J. Szczytko, M. Lefeld-Sosnowska, M. Kaminska, A. Twardowski, M. Palczewska, E. Grzanka, and W. Gebicki. Magnetic and optical properties of GaMnN magnetic semiconductor. *Applied Physics Letters*, 78:1276, 2001.

[82] M. Zajkac, J. Gosk, M. Kaminska, A. Twardowski, T. Szyszko, and S. Podsiadlo. Paramagnetism and antiferromagnetic d-d coupling in GaMnN magnetic semiconductor. *Applied Physics Letters*, 79:2432, 2001.

[83] S. Kuwabara, K. Ishii, S. Haneda, T. Kondo, and H. Munekata. Preparation of wurtzite GaN-based magnetic alloy semiconductors by molecular beam epitaxy. *Physica E: Low-dimensional Systems and Nanostructures*, 10(1-3):233–236, 2001.

[84] Y. L. Soo, G. Kioseoglou, S. Kim, S. Huang, Y. H. Kao, S. Kuwabara, S. Owa, T. Kondo, and H. Munekata. Local structure and chemical valency of Mn impurities in wide-band-gap III-V magnetic alloy semiconductors GaMnN. *Applied Physics Letters*, 79:3926, 2001.

[85] M. E. Overberg, C. R. Abernathy, S. J. Pearton, N. A. Theodoropoulou, K. T. McCarthy, and A. F. Hebard. Indication of ferromagnetism in molecular-beam-epitaxy-derived n-type GaMnN. *Applied Physics Letters*, 79:1312, 2001.

[86] T. A. Bither and W. H. Cloud. Magnetic tetragonal Delta phase in the MnGa binary. *Journal of Applied Physics*, 36:1501, 1965.

[87] N. Theodoropoulou, A. F. Hebard, M. E. Overberg, C. R. Abernathy, S. J. Pearton, S. N. G. Chu, and R. G. Wilson. Magnetic and structural properties of Mn-implanted GaN. *Applied Physics Letters*, 78:3475, 2001.

[88] M. L. Reed, N. A. El-Masry, H. H. Stadelmaier, M. K. Ritums, M. J. Reed, C. A. Parker, J. C. Roberts, and S. M. Bedair. Room temperature ferromagnetic properties of (Ga,Mn)N. *Applied Physics Letters*, 79:3473, 2001.

[89] T. Adhikari and S. Basu. Electrical properties of gallium manganese antimonide: a new diluted magnetic semiconductor. *Japanese Journal of Applied Physics*, 33: 4581, 1994.

[90] E. Abe, F. Matsukura, H. Yasuda, Y. Ohno, and H. Ohno. Molecular beam epitaxy of III-V diluted magnetic semiconductor (Ga,Mn)Sb. *Physica E: Low-dimensional Systems and Nanostructures*, 7(3-4):981–985, 2000.

[91] L. Tran, J. Herfort, O. Bierwagen, F. Hatami, and W. T. Masselink. Narrow-gap ferromagnetic semiconductors (In,Mn)Sb on GaAs (001): growth and properties. *physica status solidi (c)*, 6(6):1492–1496, 2009.

[92] N. I. Obukhov et al. Effect of exchange interaction on metal-dielectric transition in p-InSb (Mn). *Solid State Communications*, 70(1):103–105, 1989.

[93] S. A. Obukhov. Phase transition in a system of magnetic impurities. *Solid State Communications*, 88(3):255–256, 1993.

[94] T. Wojtowicz, W. L. Lim, X. Liu, G. Cywiski, M. Kutrowski, L. V. Titova, K. Yee, M. Dobrowolska, J. K. Furdyna, K. M. Yu, et al. Growth and properties of ferromagnetic $In_{1-x}Mn_xSb$ alloys. *Physica E: Low-Dimensional Systems and Nanostructures*, 20(3-4):325–332, 2004.

[95] R. P. Panguluri, B. Nadgorny, T. Wojtowicz, W. L. Lim, X. Liu, and J. K. Furdyna. Measurement of spin polarization by Andreev reflection in ferromagnetic $In_{1-x}Mn_xSb$ epilayers. *Applied Physics Letters*, 84:4947, 2004.

[96] T. Wojtowicz, J. K. Furdyna, X. Liu, K. M. Yu, and W. Walukiewicz. Electronic effects determining the formation of ferromagnetic $III_{1-x}Mn_xV$ alloys during epitaxial growth. *Physica E: Low-dimensional Systems and Nanostructures*, 25(2-3): 171–180, 2004.

[97] M. Csontos, T. Wojtowicz, X. Liu, M. Dobrowolska, B. Janko, J. K. Furdyna, and G. Mihaly. Magnetic scattering of spin polarized carriers in (In,Mn)Sb dilute magnetic semiconductor. *Physical review letters*, 95(22):227203, 2005.

[98] T. Wojtowicz, W. L. Lim, X. Liu, Y. Sasaki, U. Bindley, M. Dobrowolska, J. K. Furdyna, K. M. Yu, and W. Walukiewicz. Correlation of Mn lattice location, free hole concentration, and Curie temperature in ferromagnetic GaMnAs. *Journal of Superconductivity*, 16(1):41–44, 2003.

[99] K. M. Yu, W. Walukiewicz, T. Wojtowicz, I. Kuryliszyn, X. Liu, Y. Sasaki, and J. K. Furdyna. Effect of the location of Mn sites in ferromagnetic $Ga_{1-x}Mn_xAs$ on its Curie temperature. *Phys. Rev. B*, 65(20):201303, Apr 2002. doi: 10.1103/PhysRevB.65.201303.

[100] J. Blinowski and P. Kacman. Spin interactions of interstitial Mn ions in ferromagnetic GaMnAs. *Physical Review B*, 67(12):121204, 2003.

[101] K. Ganesan, S. Mariyappan, and H. L. Bhat. Influence of magnetic clusters on electrical and magnetic properties of $In_{1-x}Mn_xSb/GaAs$ dilute magnetic semiconductor grown by liquid phase epitaxy. *Solid State Communications*, 143(4-5): 272–275, 2007.

[102] K Ganesan. *Growth, Structural And Physical Properties Of Certain Antimony Based III-V Diluted Magnetic Semiconductors.* PhD thesis, Indian Institute of Science, 2010.

[103] A. Van Esch, L. Van Bockstal, J. De Boeck, G. Verbanck, A. S. van Steenbergen, P. J. Wellmann, B. Grietens, R. Bogaerts, F. Herlach, and G. Borghs. Interplay between the magnetic and transport properties in the III-V diluted magnetic semiconductor $Ga_{1-x}Mn_xAs$. *Phys. Rev. B*, 56(20):13103–13112, Nov 1997. doi: 10.1103/PhysRevB.56.13103.

[104] H. Ohno. Making nonmagnetic semiconductors ferromagnetic. *Science*, 281(5379): 951, 1998.

[105] T. Dietl, A. Haury, and Y. Merle dAubigne. Free carrier-induced ferromagnetism in structures of diluted magnetic semiconductors. *Phys. Rev. B*, 55(6):R3347–R3350, Feb 1997. doi: 10.1103/PhysRevB.55.R3347.

[106] T. Jungwirth, K. Y. Wang, J. Masek, K. W. Edmonds, J. Koenig, J. Sinova, M. Polini, N. A. Goncharuk, A. H. MacDonald, M. Sawicki, A. W. Rushforth, R. P. Campion, L. X. Zhao, C. T. Foxon, and B. L. Gallagher. Prospects for high temperature ferromagnetism in (Ga,Mn)As semiconductors. *Phys. Rev. B*, 72(16): 165204, Oct 2005. doi: 10.1103/PhysRevB.72.165204.

[107] T. Jungwirth, J. Koenig, J. Sinova, J. Kucera, and A. H. MacDonald. Curie temperature trends in (III,Mn)V ferromagnetic semiconductors. *Physical Review B*, 66(1):12402, 2002.

[108] T. Dietl, H. Ohno, F. Matsukura, J. Cibert, and D. Ferrand. Zener model description of ferromagnetism in zinc-blende magnetic semiconductors. *Science*, 287 (5455):1019, 2000.

[109] M. Csontos, G. Mihaly, B. Janko, T. Wojtowicz, X. Liu, and J. K. Furdyna. Pressure-induced ferromagnetism in (In,Mn)Sb dilute magnetic semiconductor. *Nature materials*, 4(6):447–449, 2005.

[110] T. Sasaki, S. Sonoda, Y. Yamamoto, K. Suga, S. Shimizu, K. Kindo, and H. Hori. Magnetic and transport characteristics on high Curie temperature ferromagnet of Mn-doped GaN. *Journal of Applied Physics*, 91:7911, 2002.

[111] C. Liu, F. Yun, and H. Morkoc. Ferromagnetism of ZnO and GaN: A review. *Journal of Materials Science: Materials in Electronics*, 16(9):555–597, 2005.

[112] L. M. Sandratskii, P. Bruno, and J. Kudrnovsky. On-site Coulomb interaction and the magnetism of (GaMn)N and (GaMn)As. *Phys. Rev. B*, 69(19):195203, May 2004. doi: 10.1103/PhysRevB.69.195203.

[113] B. Sanyal, O. Bengone, and S. Mirbt. Electronic structure and magnetism of Mn-doped GaN. *Phys. Rev. B*, 68(20):205210, Nov 2003. doi: 10.1103/PhysRevB.68.205210.

[114] M. Wierzbowska, D. Sanchez-Portal, and S. Sanvito. Different origins of the ferromagnetic order in (Ga,Mn)As and (Ga,Mn)N. *Phys. Rev. B*, 70(23):235209, Dec 2004. doi: 10.1103/PhysRevB.70.235209.

[115] J. Kreissl, W. Ulrici, M. El-Metoui, A.-M. Vasson, A. Vasson, and A. Gavaix. Neutral manganese acceptor in GaP: An electron-paramagnetic-resonance study. *Phys. Rev. B*, 54(15):10508–10515, Oct 1996. doi: 10.1103/PhysRevB.54.10508.

[116] X. Luo and R. M. Martin. Jahn-Teller distortion and ferromagnetism in the dilute magnetic semiconductors GaAs:Mn and cubic GaN:Mn. *Phys. Rev. B*, 72(3): 035212, Jul 2005. doi: 10.1103/PhysRevB.72.035212.

[117] T. C. Schulthess, W. M. Temmerman, Z. Szotek, W. H. Butler, and G. M. Stocks. Electronic structure and exchange coupling of Mn impurities in III-V semiconductors. *Nature Materials*, 4(11):838–844, 2005.

[118] L. Bergqvist and P. H. Dederichs. Dilute magnetic semiconductors. *NIC Symposium 2008*, 39:153–160, 2008.

[119] K. Sato, P. H. Dederics, and H. Katayama-Yoshida. Curie temperatures of III-V diluted magnetic semiconductors calculated from first principles. *EPL (Europhysics Letters)*, 61:403–408, 2003.

[120] K. Sato, P. H. Dederichs, H. Katayama-Yoshida, and J. Kudrnovsky. Exchange interactions in diluted magnetic semiconductors. *Journal of Physics: Condensed Matter*, 16:S5491, 2004.

[121] J. Koenige, H. Lin, and A. H. MacDonald. Theory of diluted magnetic semiconductor ferromagnetism. *Phys. Rev. Lett.*, 84(24):5628–5631, Jun 2000. doi: 10.1103/PhysRevLett.84.5628.

[122] J. Schliemann, J. Koenig, H. H. Lin, and A. H. MacDonald. Limits on the Curie temperature of (III,Mn)V ferromagnetic semiconductors. *Applied Physics Letters*, 78:1550, 2001.

[123] J. Koenig, T. Jungwirth, and A. H. MacDonald. Theory of magnetic properties and spin-wave dispersion for ferromagnetic (Ga,Mn)As. *Phys. Rev. B*, 64(18): 184423, Oct 2001. doi: 10.1103/PhysRevB.64.184423.

[124] G. Bouzerar, T. Ziman, and J. Kudrnovsky. Calculating the Curie temperature reliably in diluted III-V ferromagnetic semiconductors. *EPL (Europhysics Letters)*, 69:812, 2005.

[125] Robin F. C. Farrow. *Molecular Beam Epitaxy Applications to Key Materials*. Noyes Publications, New Jersey, U.S.A, 1995.

[126] T. Van Buuren, M. K. Weilmeier, I. Athwal, K. M. Colbow, J. A. Mackenzie, T. Tiedje, P. C. Wong, and K. A. R. Mitchell. Oxide thickness effect and surface roughening in the desorption of the oxide from GaAs. *Applied Physics Letters*, 59 (4):464–466, 2009.

[127] M. R. Brozel and G. E. Stillman. *Properties of GaAs*. EMIS Datareview INSPEC, London, 1996.

[128] S. F. Fang, K. Adomi, S. Iyer, H. Morkoc, H. Zabel, C. Choi, and N. Otsuka. Gallium arsenide and other compound semiconductors on silicon. *Journal of Applied Physics*, 68:R31, 1990.

[129] A. Ermolieff, S. Marthon, X. Rochet, D. Rouchon, O. Renault, A. Michallet, and F. Tardif. Silicon wafer cleaning processes and ozone oxide growth as studied by angle-resolved x-ray photoelectron spectroscopy (ARXPS) and ellipsometry. *Surface and Interface Analysis*, 33(5):433–436, 2002.

[130] R. Fischer, H. Morkoc, D. A. Neumann, H. Zabel, C. Choi, N. Otsuka, M. Longerbone, and L. P. Erickson. Material properties of high-quality GaAs epitaxial layers grown on Si substrates. *Journal of Applied Physics*, 60:1640, 1986.

[131] R. Houdre and H. Morkoc. Properties of GaAs on Si grown by molecular beam epitaxy. *Critical Reviews in Solid State and Materials Sciences*, 16(2):91–114, 1990.

[132] G. Mussler. *Growth and Characterization of Ga(As,N) and (In,Ga)(As,N)*. PhD thesis, Humboldt-Universitat zu Berlin, 2007.

[133] Bede scientific instruments LTD. *Rocking curve analysis by dynamical simulation, user guide*. Bede scientific instruments LTD, 1998.

[134] J. L. Davis and P. E. Thompson. Molecular beam epitaxy growth of InSb films on GaAs. *Applied Physics Letters*, 54:2235–2237, 1989.

[135] T. W. Kim, H. C. Bae, and H. L. Park. Structural and optical properties of InSb epitaxial films grown on GaAs (100) substrates at low temperature. *Applied Physics Letters*, 74:380, 1999.

[136] M. A. McKee, B. S. Yoo, and R. A. Stall. Uniform growth of InSb on GaAs in a rotating disk reactor by LP-MOVPE. *Journal of Crystal Growth*, 124(1-4): 286–291, 1992.

[137] Bede scientific instruments LTD. *Bede scientific QC1a Diffractometer, user guide.* Bede scientific instruments LTD, 1997.

[138] L. T. van der Pauw. A method of measuring specific resistivity and Hall effect of discs of arbitrary shape. *Philips Res. Rep.*, 13:1–9, 1958.

[139] R. L. Petritz. Theory of an experiment for measuring the mobility and density of carriers in the space-charge region of a semiconductor surface. *Physical Review*, 110(6):1254–1262, 1958.

[140] R.A. Smith. *Semiconductor.* Cambridge University press, 1978.

[141] B. Poedoer. Electron mobility in plastically deformed germanium. *physica status solidi (b)*, 16(2):K167–K170, 1966.

[142] D. L. Dexter and F. Seitz. Effects of dislocations on mobilities in semiconductors. *Physical Review*, 86(6):964–965, 1952.

[143] X. Weng, N. G. Rudawski, P. T. Wang, R. S. Goldman, D. L. Partin, and J. Heremans. Effects of buffer layers on the structural and electronic properties of InSb films. *Journal of Applied Physics*, 97:043713, 2005.

[144] D. L. Partin, J. Heremans, and C. M. Thrush. Effect of an InAlSb buffer layer on InSb thin film mobility. *Journal of Vacuum Science and Technology B: Microelectronics and Nanometer Structures*, 17:1267, 1999.

[145] R. M. Biefeld and J. D. Phillips. Growth of InSb on GaAs using InAlSb buffer layers. *Journal of Crystal Growth*, 209(4):567–571, 2000.

[146] T. Sato, M. Akabori, and S. Yamada. High-quality highly mismatched InSb films grown on GaAs substrate via thick AlSb and InAlSb step-graded buffers. *Physica E: Low-dimensional Systems and Nanostructures*, 21(2-4):615–619, 2004.

[147] E. Michel, G. Singh, S. Slivken, C. Besikci, P. Bove, I. Ferguson, and M. Razeghi. Molecular beam epitaxial growth of high quality InSb. *Applied Physics Letters*, 65 (26):3338–3340, 2009.

[148] Friederike K. B. Ernst. Crystallographic and electronic properties of InSb grown on Si in comparison to InSb grown on GaAs. Master's thesis, Humboldt-Universitaet zu Berlin, 2010.

[149] F. Abelès. *Optical Properties of Solids*. North-Holland Publishing Company, Amsterdam, London, 1972.

[150] F. N. Hooge. 1/f noise is no surface effect. *Physics Letters A*, 29(3):139–140, 1969.

[151] F. N. Hooge. Discussion of recent experiments on 1/f noise. *Physica*, 60(1):130–144, 1972.

[152] X. Y. Chen and M. R. Leys. Study of 1/f noise in InP grown by CBE. *Solid-State Electronics*, 39(8):1149–1153, 1996.

[153] F. N. Hooge. 1/f noise sources. *Electron Devices, IEEE Transactions on*, 41(11): 1926–1935, 2002.

[154] L. Ren and F. N. Hooge. Temperature dependence of 1/f noise in epitaxial n-type GaAs. *Physica B: Condensed Matter*, 176(3):209–212, 1992.

[155] L. Ren and M. R. Leys. 1/f noise at room temperature in n-type GaAs grown by molecular beam epitaxy. *Physica B: Condensed Matter*, 172(3):319–323, 1991.

[156] O. A. Mironov, M. Myronov, S. Durov, V. T. Igumenov, V. M. Konstantinov, VV Paramonov, T. Zhang, and L. F. Cohen. The sub-micrometer thickness n-InSb/i-GaAs epilayers for magnetoresistor applications at room temperatures of operation. *Physica E: Low-dimensional Systems and Nanostructures*, 20(3-4):523–526, 2004.

[157] V. Kunets et al. Highly sensitive micro-Hall devices based on $Al_{0.12}In_{0.88}Sb$/InSb heterostructures. *Journal of Applied Physics*, 98(1):4506, 2005.

[158] Sh. Kogan. *Electronic noise and fluctuations in solids*. Cambridge University Press, 1996.

[159] N. V. Dyakonova and M. E. Levinshtein. Model of bulk 1/f noise in semiconductors. *Sov. Phys. Semicond*, 23:175, 1989.

[160] M. Mori, D. M. Li, M. Yamazaki, T. Tambo, H. Ueba, and C. Tatsuyama. Heteroepitaxial growth of InSb on Si (001) surface via Ge buffer layers. *Applied Surface Science*, 104-105:563–569, 1996.

[161] I. Kuryliszyn-Kudelska, J. Z. Domagala, T. Wojtowicz, X. Liu, E. Lusakowska, W. Dobrowolski, and J. K. Furdyna. Effect of Mn interstitials on the lattice parameter of GaMnAs. *Journal of Applied Physics*, 95(2):603–608, 2009.

[162] L. X. Zhao, R. P. Campion, P. F. Fewster, R. W. Martin, B. Y. Ber, A. P. Kovarsky, C. R. Staddon, K. Y. Wang, K. W. Edmonds, C. T. Foxon, et al. Determination of the Mn concentration in GaMnAs. *Semiconductor Science and Technology*, 20: 369, 2005.

[163] R. P. Campion, K. W. Edmonds, L. X. Zhao, K. Y. Wang, C. T. Foxon, B. L. Gallagher, and C. R. Staddon. High-quality GaMnAs films grown with arsenic dimers. *Journal of Crystal Growth*, 247(1-2):42–48, 2003.

[164] T. Hayashi, M. Tanaka, T. Nishinaga, H. Shimada, H. Tsuchiya, and Y. Otuka. (GaMn)As: GaAs-based III-V diluted magnetic semiconductors grown by molecular beam epitaxy. *Journal of Crystal Growth*, 175:1063–1068, 1997.

[165] H. Ohno, A. Shen, F. Matsukura, A. Oiwa, A. Endo, S. Katsumoto, and Y. Iye. (Ga,Mn)As: A new diluted magnetic semiconductor based on GaAs. *Applied Physics Letters*, 69:363, 1996.

[166] G. M. Schott, G. Schmidt, G. Karczewski, L. W. Molenkamp, R. Jakiela, and A. Barcz. Influence of growth conditions on the lattice constant and composition of (Ga,Mn)As. *Applied Physics Letters*, 82:4678, 2003.

[167] A. Continenza, S. Picozzi, W. T. Geng, and A. J. Freeman. Coordination and chemical effects on the structural, electronic, and magnetic properties in Mn pnictides. *Physical Review B*, 64(8):85204, 2001.

[168] J. Sadowski and J. Z. Domagala. Influence of defects on the lattice constant of GaMnAs. *Physical Review B*, 69(7):75206, 2004.

[169] L. X. Zhao, C. R. Staddon, K. Y. Wang, K. W. Edmonds, R. P. Campion, B. L. Gallagher, and C. T. Foxon. Intrinsic and extrinsic contributions to the lattice parameter of GaMnAs. *Applied Physics Letters*, 86:071902, 2005.

[170] H. Luo, B. D. McCombe, M. H. Na, K. Mooney, F. Lehmann, X. Chen, M. Cheon, S. M. Wang, Y. Sasaki, X. Liu, et al. Transport and magnetic properties of ferromagnetic GaAs/Mn digital alloys. *Physica E: Low-dimensional Systems and Nanostructures*, 12(1-4):366–369, 2002. ISSN 1386-9477.

[171] A. Oiwa, S. Katsumoto, A. Endo, M. Hirasawa, Y. Iye, H. Ohno, F. Matsukura, A. Shen, and Y. Sugawara. Giant negative magnetoresistance of (Ga, Mn) As/GaAs in the vicinity of a metal-insulator transition. *physica status solidi (b)*, 205(1):167–171, 1998. ISSN 1521-3951.

[172] Y. Iye, A. Oiwa, A. Endo, S. Katsumoto, F. Matsukura, A. Shen, H. Ohno, and H. Munekata. Metal-insulator transition and magnetotransport in III-V compound diluted magnetic semiconductors. *Materials Science and Engineering B*, 63 (1-2):88–95, 1999. ISSN 0921-5107 begin_of_the_skype_highlighting 0921-5107 end_of_the_skype_highlighting.

[173] D. J. Thouless. Anderson's theory of localized states. *Journal of Physics C: Solid State Physics*, 3:1559, 1970.

[174] P. W. Anderson. The size of localized states near the mobility edge. *Proc. Nat. Acade. Sci. USA*, 69:1097–1099, 1972.

[175] Y. D. Park, A. Wilson, A. T. Hanbicki, J. E. Mattson, T. Ambrose, G. Spanos, and B. T. Jonker. Magnetoresistance of Mn: Ge ferromagnetic nanoclusters in a diluted magnetic semiconductor matrix. *Applied Physics Letters*, 78:2739, 2001.

[176] M. E. Raikh, J. Czingon, Q. Ye, F. Koch, W. Schoepe, and K. Ploog. Mechanisms of magnetoresistance in variable-range-hopping transport for two-dimensional electron systems. *Phys. Rev. B*, 45(11):6015–6022, Mar 1992. doi: 10.1103/PhysRevB.45.6015.

[177] I.T. Yoon, T.W. Kang, K.H. Kim, and D.J. Kim. A Hall coefficient investigation of ferromagnetic $Ga_{1-x}Mn_xAs$ layers on (100) GaAs substrates. *Solid State Communications*, 130(9):627–630, 2004. ISSN 0038-1098.

[178] K. Y. Wang, K. W. Edmonds, L. X. Zhao, M. Sawicki, R. P. Campion, B. Gallagher, and C. T. Foxon. (Ga,Mn)As grown on (311) GaAs substrates: Modified Mn incorporation and magnetic anisotropies. *Physical Review B*, 72(11):115207, 2005. ISSN 1550-235X.

[179] W. L. Lim, T. Wojtowicz, X. Liu, M. Dobrowolska, and J. K. Furdyna. MBE growth and magnetotransport studies of ferromagnetic $Ga_{1-x}Mn_xSb$ semiconductor layers on hybrid ZnTe/GaAs substrates. *Physica E: Low-dimensional Systems and Nanostructures*, 20(3-4):346–349, 2004. ISSN 1386-9477.

[180] I. T. Yoon, T. W. Kang, K. H. Kim, and D. J. Kim. Magnetotransport properties of ferromagnetic GaMnAs layers on a (100) GaAs substrate. *Journal of Applied Physics*, 97:063902, 2005.

[181] T. Jungwirth, Q. Niu, and A. H. MacDonald. Anomalous Hall effect in ferromagnetic semiconductors. *Physical review letters*, 88(20):207208, 2002.

[182] R Karplus and J. M. Luttinger. Hall effect in ferromagnetics. *Phys. Rev.*, 95(5): 1154–1160, Sep 1954. doi: 10.1103/PhysRev.95.1154.

[183] M. Onoda and N. Nagaosa. Quantized anomalous Hall effect in two-dimensional ferromagnets: Quantum Hall effect in metals. *Phys. Rev. Lett.*, 90(20):206601, May 2003. doi: 10.1103/PhysRevLett.90.206601.

[184] J. Sinova, T. Jungwirth, J. Kučera, and A. H. MacDonald. Infrared magneto-optical properties of (III,Mn)V ferromagetic semiconductors. *Phys. Rev. B*, 67 (23):235203, Jun 2003. doi: 10.1103/PhysRevB.67.235203.

[185] Z. Fang, N. Nagaosa, K. S. Takahashi, A. Asamitsu, R. Mathieu, T. Ogasawara, H. Yamada, M. Kawasaki, Y. Tokura, and K. Terakura. The anomalous Hall effect and magnetic monopoles in momentum space. *Science*, 302(5642):92, 2003.

[186] J. M. Luttinger. Theory of the Hall effect in ferromagnetic substances. *Phys. Rev.*, 112(3):739–751, Nov 1958. doi: 10.1103/PhysRev.112.739.

[187] L. Berger. Side-jump mechanism for the Hall effect of ferromagnets. *Phys. Rev. B*, 2(11):4559–4566, Dec 1970. doi: 10.1103/PhysRevB.2.4559.

[188] A. Oiwa, A. Endo, S. Katsumoto, Y. Iye, H. Ohno, and H. Munekata. Magnetic and transport properties of the ferromagnetic semiconductor heterostructures (In,Mn)As/(Ga,Al)Sb. *Phys. Rev. B*, 59(8):5826–5831, Feb 1999. doi: 10.1103/PhysRevB.59.5826.

[189] M. Sawicki, F. Matsukura, A. Idziaszek, T. Dietl, G. M. Schott, C. Ruester, C. Gould, G. Karczewski, G. Schmidt, and L. W. Molenkamp. Temperature dependent magnetic anisotropy in (Ga,Mn)As layers. *Phys. Rev. B*, 70(24):245325, Dec 2004. doi: 10.1103/PhysRevB.70.245325.

[190] J. L. Tracy, G. Franzese, Ashlee Byrd, J. Garner, T. M. Pekarek, I. Miotkowski, and A. K. Ramdas. Anisotropic magnetization of the III-VI diluted magnetic semiconductor $In_{1-x}Mn_xSb$ in the mixed state. *Phys. Rev. B*, 72(16):165201, Oct 2005. doi: 10.1103/PhysRevB.72.165201.

[191] Mike McElfresh. *Fundamentals of magnetism and magnetic me*. Purdue University, 1994.

[192] K. Y. Wang, M. Sawicki, K. W. Edmonds, R. P. Campion, A. W. Rushforth, A. A. Freeman, C. T. Foxon, B. L. Gallagher, and T. Dietl. Control of coercivities in (Ga,Mn)As thin films by small concentrations of MnAs nanoclusters. *Applied Physics Letters*, 88:022510, 2006.

[193] M. Wang, R. P. Campion, A. W. Rushforth, K. W. Edmonds, C. T. Foxon, and B. L. Gallagher. Achieving high Curie temperature in (Ga,Mn)As. *Applied Physics Letters*, 93:132103, 2008.

[194] F. Matsukura, E. Abe, and H. Ohno. Magnetotransport properties of (Ga,Mn)Sb. *Journal of Applied Physics*, 87(9):6442–6444, 2009. ISSN 0021-8979.

[195] H. Zhang, S. S. Kushvaha, S. Chen, X. Gao, D. Qi, A. T. S. Wee, and X. S. Wang. Synthesis and magnetic properties of MnSb nanoparticles on Si-based substrates. *Applied Physics Letters*, 90:202503, 2007.

[196] G. Czack. *Manganese in Gmelin Handbook of Inorganic Chemistry*. Spinger Berlin, 1993.

[197] L. Tran, F. Hatami, J. Herfort, A. Trampert, and W. T. Masselink. Distribution of Mn in ferromagnetic (In,Mn)Sb films grown on (001) GaAs using MBE. *Journal of Crystal Growth*, doi:10.1016/j.jcrysgro.2010.10.127, 2010.

[198] T. Zhang, M. Debnath, S. K. Clowes, W. R. Branford, A. Bennett, C. Roberts, L. F. Cohen, and R. A. Stradling. InSb epilayers on GaAs (100) for spintronic and magneto-resistive sensor applications. *Physica E: Low-dimensional Systems and Nanostructures*, 20(3-4):216–219, 2004. ISSN 1386-9477.

[199] I. Kimukin, N. Biyikli, and E. Ozbay. InSb high-speed photodetectors grown on GaAs substrate. *Journal of Applied Physics*, 94:5414, 2003.

[200] A. Tevke, C. Besikci, C. Van Hoof, and G. Borghs. InSb infrared pin photodetectors grown on GaAs coated Si substrates by molecular beam epitaxy. *Solid-State Electronics*, 42(6):1039–1044, 1998. ISSN 0038-1101.

[201] H. Akinaga, J. De Boeck, G. Borghs, S. Miyanishi, A. Asamitsu, W. Van Roy, Y. Tomioka, and L. H. Kuo. Negative magnetoresistance in GaAs with magnetic MnAs nanoclusters. *Applied Physics Letters*, 72:3368, 1998.

[202] O. Bierwagen, R. Pomraenke, S. Eilers, and W. T. Masselink. Mobility and carrier density in materials with anisotropic conductivity revealed by Van der Pauw measurements. *Physical Review B*, 70(16):165307, 2004.

[203] T. Dietl. Ferromagnetic semiconductors. *Semiconductor Science and Technology*, 17:377–392, 2002.

[204] P. Dutta, P. Dimon, and P. M. Horn. Energy scales for noise processes in metals. *Phys. Rev. Lett.*, 43(9):646–649, Aug 1979. doi: 10.1103/PhysRevLett.43.646.

[205] K. W. Edmonds, K. Y. Wang, R. P. Campion, A. C. Neumann, C. T. Foxon, B. L. Gallagher, and P. C. Main. Hall effect and hole densities in $Ga_{1-x}Mn_xAs$. *Applied Physics Letters*, 81(16):3010, 2002.

[206] P. H. Handel. Fundamental quantum 1/f noise in semiconductor devices. *Electron Devices, IEEE Transactions on*, 41(11):2023–2033, 2002.

[207] T. Hartmann, M. Lampalzer, W. Stolz, K. Megges, J. Lorberth, P. J. Klar, and W. Heimbrodt. Optical characterisation of MOVPE-grown $Ga_{1-x}Mn_xAs$ semimagnetic semiconductor layers. *Thin Solid Films*, 364(1-2):209–212, 2000.

[208] W. Heimbrodt, T. Hartmann, P. J. Klar, M. Lampalzer, W. Stolz, K. Volz, A. Schaper, W. Treutmann, H. A. K. von Nidda, A. Loidl, et al. Monitoring the sign reversal of the valence band exchange integral in (Ga,Mn)As. *Physica E: Low-dimensional Systems and Nanostructures*, 10(1-3):175–180, 2001.

[209] H. Itoh, S. Narui, Z. Zhang, and T. Ichonokawa. Structure of double-atomic-height steps in si(001) vicinal surfaces observed by scanning tunneling microscopy. *Surface science letters*, 277:L70–L76, 2002.

[210] R. H. Kingston. *Semiconductor Surface Physics*. University of Pennsylvania Press, Philadelphia, 1957.

[211] G. S. Kousik, C. M. Van Vliet, G. Bosman, and P. H. Handel. Quantum 1/f noise associated with ionized impurity scattering and electron-phonon scattering in condensed matter. *Advances in Physics*, 34(6):663–702, 1985.

[212] J. I. Lee, J. Brini, A. Chovet, and C. A. Dimitriadis. Flicker noise by random walk of electrons at the interface in nonideal Schottky diodes. *Solid-State Electronics*, 43(12):2185–2189, 1999.

[213] M. E. Levinshtein. Nature of the volume 1/f noise in the main materials of semiconductor electronics: Si, GaAs, and SiC. *Physica Scripta*, 1997:79, 1997.

[214] S. J. May, A. J. Blattner, and B. W. Wessels. Negative magnetoresistance in (In,Mn)As semiconductors. *Phys. Rev. B*, 70(7):073303, Aug 2004. doi: 10.1103/PhysRevB.70.073303.

[215] D. K. Satapathy. *Molecular-beam epitaxy growth and structural characterization of semiconductor-ferromagnet heterostructures by grazing incidence x-ray diffraction*. PhD thesis, Humboldt-Universität zu Berlin, 2005.

[216] J. R. Soederstroem, M. M. Cumming, J. Yao, et al. Molecular beam epitaxy growth and characterization of InSb layers on GaAs substrates. *Semiconductor Science and Technology*, 7:337, 1992.

[217] H. Yasuda and H. Ohno. Monte Carlo simulation of reentrant reflection high-energy electron diffraction intensity oscillation observed during low-temperature GaAs growth. *Applied Physics Letters*, 74:3275–3277, 1999.

Acknowledgements

First of all, I thank the Ministry of Education and Training in Vietnam for the financial support during my PhD.

I would like to express my gratitude to Prof. Dr. W. Ted Masselink who accepted me to work in his group, stimulated and supported at all the stages in my investigation as well as gave me many opportunities to attend conferences. I am greatly indebted to him for his kindness, supervision and support the progress of my work. Prof. Dr. Masselink also commended me to Prof. Dr. Henning Riechert at the Paul-Drude Institut, who kindly allowed me to do some measurements there and to attend some conferences. I would like to express my respect for them, who are not only excellent in science but also have such a beautiful character.

In particular, I deeply thank Dr. Fariba Hatami who is not only my dear colleague but also like my sister. I would especially like to thank for her help, encouragement, and valuable advices in the work as well as in the life. I also thank her for proof-reading this thesis. I will never forget her kindly guidance to get the financial support for conferences and for the last six months of the PhD. I also never forget her stories about children such as "How a child learn to walk". Now I know for sure that if I fall down I will stand up, if I do something wrong, I can do it then better. Words are not enough to express my gratitude to her. Just say: I am so lucky to know her, to share the same office space with her. Thank you to be there for me, Fariba.

Many thanks to Dr. Oliver Bierwagen for his valuable introduction and supervision in MBE technique, x-ray and transport measurements, especially his practical assistance in Hall measurements.

Furthermore, I have to express my gratitude to my colleagues: Dr. Mykhaylo Semtsiv who has introduced me to the MBE and guided me the optical as well as x-ray measurements; Sebastian Dressler for his kindly help in organizational and insurance concerns as I was a newcomer; Julia Dobbert for her co-operation to publish our data; Martin Wienold for SEM; Karin Braune for AFM; Asli Ugur for guiding me the AFM software analysis; Nelli Anand for solving organizational and management problems.

I am particularly grateful to Dr. Achim Trampert and Dr. Jens Herfort at Paul-Drude Institute who helped me during the TEM and magnetization measurements. Many thanks for the fruitful scientific discussions and co-operation to publish papers.

Additionally, I thank Dr. Vasyl Kunets of University of Arkansas for magnetization measurements, and helpful discussions.

I also thank my parents and my sisters in Vietnam who often encourage me when I have difficulties. Many thanks to my husband Quang-Long for his love and support, and of course to my lovely kids Nhat-Minh and Angelina.

Last but not least the referees are deeply appreciated.

Selbständigkeitserklärung

Ich erkläre, dass ich die vorliegende Arbeit "*InSb Semiconductors and (In,Mn)Sb Diluted Magnetic Semiconductors: Growth and Properties*" selbständig und nur unter Verwendung der angegebenen Literatur und Hilfsmittel angefertigt habe.

Ich habe mich anderwärts nicht um einen Doktorgrad beworben und besitze einen entsprechenden Doktorgrad nicht.

Ich erkläre die Kenntnisnahme der dem Verfahren zugrunde liegenden Promotionsordnung der Mathematisch-Naturwissenschaftlichen Fakultät I der Humboldt-Universität zu Berlin.

Berlin, den 20.02.2011

Lien Tran